学位論文

Electronic Transport and Angle-resolved Photoemission Studies of Iron-based Superconductors

(電子輸送および角度分解光電子分光による鉄系超伝導体の研究)

平成２５年１２月博士（理学）申請

東京大学大学院理学系研究科

物理学専攻

劉　亮

Abstract

Almost all of the parent compounds of iron-based superconductors (FeSCs) harbor metallic antiferromagnetic (AFM) ground states. The AFM transition is either accompanied or preceded in temperature by a structural transition that breaks a fourfold rotational symmetry of the tetragonal high-temperature lattice. Due to the proximity of the AFM phase to the superconducting phase, many efforts have been done, especially in the most studied "122" family of compounds (for example $BaFe_2As_2$), to investigate its electronic nature with the broken fourfold rotational symmetry. However, several important controversies on the experimental results such as the origin of the remarkable resistivity anisotropy and the Fermi surfaces (FSs) in the AFM state still exist. In this thesis, we mainly focused on the effects of atom substitution in the metallic AFM state of the "122" iron pnictides and the "11" iron chalcogenides through transport and angle-resolved photoemission spectroscopy (ARPES) measurements.

In the "11" compounds, we first studied the effect of unavoidably preexisting excess Fe ions via transport measurements in the parent compound $Fe_{1+x}Te$. Our results showed the evolution of the temperature dependence of resistivity upon increasing excess Fe content, which corresponds to the change of the magneto-structural phase tuned by the excess Fe content. It was revealed that excess Fe ions exhibit strong scattering effects in both AFM and paramagnetic-tetragonal phases. The in-plane resistivity anisotropy was investigated in single crystals detwinned by applying uniaxial pressure. No anisotropy was observed well above T_s, while a clear anisotropy appeared when the temperature was decreased below T_s. Notably, ρ_a was higher than ρ_b, opposite to the anisotropy observed in the iron pnictides. It was found that the resistivity anisotropy was mostly determined by the anisotropy in the residual resistivity component. Further studies of Cu-substituted $Fe_{1+x}Te$ found that the magnitude of resistivity anisotropy increased with a larger amount of impurity (excess Fe and/or Cu) ions while the AFM order was correspondingly suppressed. This is suggestive of the generic applicability of the impurity-induced-anisotropy scenario for explaining the origin of resistivity anisotropy observed in the iron-based materials.

In the "122" system, it was surprisingly shown that Ru substitution for Fe atoms exhibited a much weaker effect on increasing residual resistivity in the AFM state, compared with electron doping via 3d transition-metal (e.g., Co) substitution. ARPES measurements on detwinned crystals of $Ba(Fe_{1-x}Ru_x)_2As_2$ (x = 0.04) were performed to reveal the intrinsic anisotropic electronic structures. Three types of FS pockets were

revealed: isotropic hole pockets located at the Brillouin zone center, Dirac-cone-like tiny electron pockets along the Z-X direction which originate from the band crossing at 20 meV below E_F, and another relatively larger electron pocket along the Z-Y direction, which arises from the band folding and consequent band reconstruction. The most anisotropic feature in the band dispersions was the d_{xz}-d_{yz} band splitting around the 2-Fe Brillouin-zone corner, similar to that reported for $Ba(Fe_{1-x}Co_x)_2As_2$, where the electron doping had a relatively large effect on the suppression of the electronic anisotropy compared to the structural modification induced by 4d Ru substitution. Moreover, our results presented a strong three dimensional character both in the hole pocket and in the energy scale related to the band splitting.

Besides, the existence of line nodes has been strongly suggested in the Ru-substituted $BaFe_2As_2$ like in the isovalent P-substituted $BaFe_2As_2$. Our ARPES studies of $Ba(Fe_{1-x}Ru_x)_2As_2$ (x = 0.35) found that the superconducting (SC) gaps both on the hole FSs and the electron FSs are isotropic in the k_x-k_y plane, suggesting the inexistence of "vertical" line nodes. It was also revealed that the SC gaps on the hole FSs showed a strong k_z dependence, namely, the gap minimum appears around the Z point, implying the possible existence of "horizontal" line nodes near Z. The resemblance in the SC-gap structure of P- and Ru-substituted 122 compounds suggests an important role of pnictogen height in tuning the SC-gap structures of iron-based superconductors.

Contents

Chapter 1

Introduction

1.1 Iron-based superconductors

The discovery of superconductivity at 26 K in F-doped LaFeAsO [1] has led to the world-wide effort to investigate the new family of superconductors, namely iron-based superconductors (FeSCs), over the past several years. Very soon after the discovery of the superconducting transition temperature (T_c) at 26 K, T_c was raised to ~ 55 K in $SmFeAs(O_{1-x}F_x)$ [2], the reported highest T_c in FeSCs so far. Nowadays, FeSCs are regarded as the second family of the high-T_c superconductor group in addition to the famous cuprate superconductors.

The electronic phase diagram usually gives the most basic but important physical aspects of superconductors. The phase diagram of the FeSCs (for details see §2.2) is strikingly similar to that of cuprates: the parent compounds exhibit antiferromagnetic (AFM) ordering; chemical substitutions suppress the AFM ordering and finally induce superconductivity. Although the mediator of paring in both systems remains unsolved, spin fluctuations have been intensively investigated [2], and are widely believed to play a crucial role in the superconductivity.

On the other hand, two major distinct features exist between the phase diagrams of the two systems.

1. The parent compound of the cuprate is an insulator with a charge-transfer gap. AFM states develop within the CuO_2 planes as a consequence of the strong on-site Coulomb repulsion between electrons in the same Cu $3d_{x^2-y^2}$ orbital [3]. As for FeSCs, the parent compound is metallic. Several bands dominantly derived from the Fe 3d orbitals cross E_F, resulting in a multiband system.
2. The electronic phases of cuprates tuned by various chemical substitutions can be unified to be dependent on the carrier concentration. Substitution for atoms in the basal copper-oxide layer is detrimental to superconductivity. In contrast, superconductivity in FeSCs can be induced by chemical substitution of wider variety, including direct substitution in the active iron-pnictogen layer. It turns out that the simple charge doping is not the sole factor in determining the phase diagrams of FeSCs.

1.2 Purpose of this study

Drawing on the experience of more than 20 years' studies of cuprates that the explanation of the phase diagram (e.g., the evolution of the electronic ground state from the insulating state in the parent compound to the superconducting (SC) state with carrier doping) is one of the most important steps to access the mechanism of high-T_c superconductivity in cuprate, the understanding of the metallic AFM ground state in the parent compounds of FeSCs and the appearance of the superconductivity with atom substitution would be pivotal to work out the mechanism of superconductivity in FeSCs. As a starting point, it calls for a high priority to clarify the nature of the metallic AFM state.

It has been revealed that the appearance of antiferromagnetism in FeSCs with decreasing temperature is either accompanied or preceded by a structural phase transition which breaks the fourfold rotational symmetry. Intensive studies of the AFM phase have been performed by transport measurements [4-9], optical measurements [10, 11], and angle-resolved photoemission spectroscopy (ARPES) [12, 13], and revealed the unique feature of the AFM ground state with unprecedented in-plane electronic anisotropy (for details see §2.6). Sizable resistivity anisotropy has been observed in the initial studies of the AFM ground state of "122" compounds, the origin of which has been discussed in terms of the anisotropy of reconstructed Fermi surfaces (FSs) [8, 14] or orbital ordering [15]. From recent studies of annealed Co-doped "122" compounds with significantly improved qualities, an impurity-induced-anisotropy scenario was proposed to explain the observed resistivity anisotropy [6, 10, 16]. Those studies provided evidence that a doped Co atom forms an impurity state, which anisotropically scatters carriers. The question naturally arises: *how does the anomalous anisotropic impurity state form in the AFM ground state?* To reach the answer to this basic question, it would be helpful to first clarify the following two issues:

1. *Can the impurity-induced-anisotropy scenario be verified in systems with different kinds of atom substitution? If it is true, what will the impurity state be like for the different kinds of impurity atoms?*

   In order to answer the questions, the isovalent Ru-substituted "122" compounds have be investigated through transport measurements, since Ru atoms would substitute Fe atoms like Co while Ru substitution introduces much weaker disorders than Co substitution. In addition, a comprehensive understanding of the electronic structure of the AFM state is highly needed. ARPES is a powerful method which allows direct access to band structures in condensed matter systems. We have performed an

ARPES study of the Ru-substituted “122” compounds to reveal its anisotropic electronic structure.

2. *Is the observed resistivity anisotropy in iron pnictides generic including iron chalcogenides?*
   The “11” iron chalcogenides, another family of FeSCs, have a distinct AFM ordering periodicity from the “122” compounds (for details see §2.4). In order to establish comparison between the “11” and “122” compounds, the in-plane resistivity anisotropy and the effect of transition-metal substitution for Fe and of isovalent substitution for Te have been investigated through transport measurements.

Besides, measurement of the superconducting (SC) order parameter is another route to deepen the understanding of superconductivity due to its close relationship with the nature of paring interaction. ARPES with high resolution in energy allows directly probing of SC gap structure in the momentum space. A variety of superconducting gap structures in FeSCs, such as nodeless $s_{\pm}$-wave, nodal *s*-wave, nodeless s_{++} and nodal *d*-wave have been discussed from the theoretical point of views [17]. In order to identify the SC gap structure of the isovalent Ru-substituted 122 compounds, we have performed an ARPES study of $Ba(Fe_{1-x}Ru_x)_2As_2$ (x = 0.35).

1.3 Organization of the thesis

The present thesis is organized as follows. In Chapter 2, we describe the background for the present study on the physical properties of iron-based superconductors, focusing on the “122” and “11” compounds. In Chapter 3, we firstly introduce the methods of the single crystal growth, the transport measurements, then the techniques and the experimental setup of photoemission spectroscopy. In Chapters 4 and 5, we characterize the grown single crystals and present the results of the in-plane resistivity measurements in the “11” iron chalcogenides. In Chapter 6, we present the study of $Ba(Fe_{1-x}Ru_x)_2As_2$ in the AFM ground state. The FSs and the electronic anisotropy are discussed compared with the previous studies. In Chapter 7, we study the superconducting gap structure of $Ba(Fe_{1-x}Ru_x)_2As_2$ (x = 0.35). Finally, the summary is given in Chapter 8.

Chapter 2

Background

2.1 Families and their crystal structures of iron-based superconductors

So far, six different structural classes of iron-based superconductors (FeSCs) have been found [18]. These structures are shown in Fig. 2.1, all sharing a common layered structure based on a planar layer of iron atoms joined by tetrahedrally coordinated pnictogen (As, P) or chalcogen (S, Se, Te) anions arranged in a stacked sequence [19]. It is now widely thought that it is this iron pnictogen/chalcogen (Pn/Ch) building blocks that play a crucial role in the high T_c superconductivity, similar in nature to the common copper-oxygen building block found in the high-T_c cuprate superconductors. Specifically, Pn/Ch-Fe-Pn/Ch bond angle in the tetrahedral building blocks are pointed out to be strongly correlated with the T_c and the Pn/Ch height is considered to affect the nature of superconducting gap symmetry [17].

One element dividing FeSCs into different families is the "blocking layer". In the case with the FeAs building blocks, "1111" family shows rare-earth and oxygen/fluorine (e.g., LaO [2]) separating FeAs blocks in the c axis while it is alkaline-earth (e.g., Ba [2]) in "122" family, alkali (e.g., Li [2]) in "111" family and later reported more complicated perovskite-type combinations in $Sr_4V_2O_6Fe_2As_2$ [17]. In the case with FeSe blocks, a simple α-PbO-type crystal structure with only the FeSe layers in "11" family supports superconductivity at 8 K [20]. The most recently discovered "122*" family has an ordered-defect alteration of the 122 structure, with alkali (e.g., Li) intercalated between the FeSe blocks as shown in Fig. 2.1(f) [21]. It is noted that all the six structures are tetragonal at room temperature, but four of the six have the same space group, P4/*nmm*, with the primitive tetragonal (pt) lattice while the 122 structure has I4/mmm with the body-centered tetragonal (bct) lattice. This difference would result in the different reciprocal lattices, pt for the four families and bct for the 122 structure. Hereafter we focus on the 122 and 11 compounds studied in this thesis.

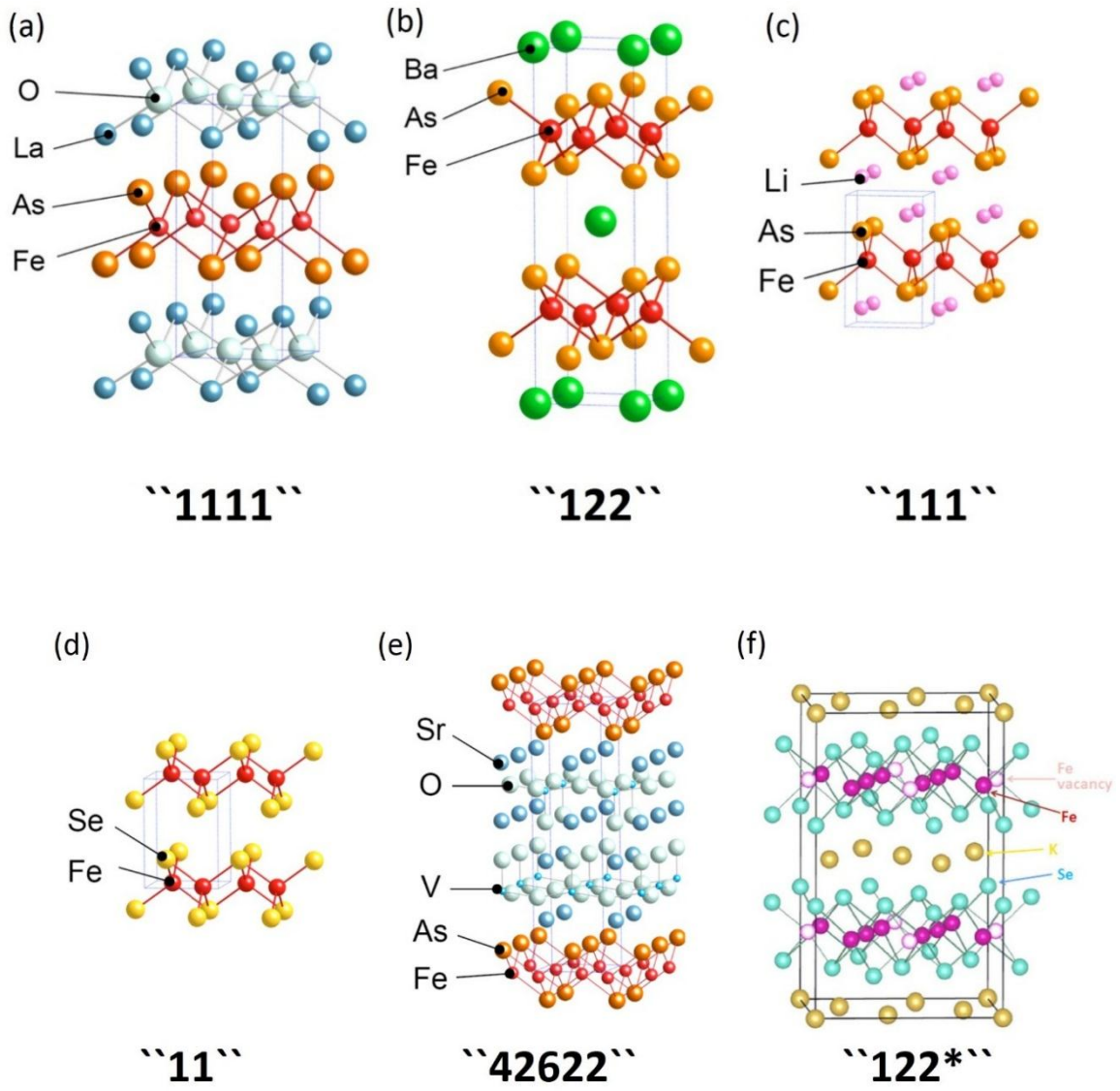

Figure 2.1 Crystal structures of the six typical classes of iron-based superconductors. (a) LaOFeAs ("1111" family); (b) $BaFe_2As_2$ ("122" family); (c) LiFeAs ("111" family); (d) FeSe ("11" family); (e) $Sr_4V_2O_6Fe_2As_2$. Reprinted from [19]. (f) $K_{0.8}Fe_{1.6}Se_2$ (called "122*"). Reprinted from [21].

2.2 Phase diagram

The typical parent compound of the 122 materials, $BaFe_2As_2$, shows a tetragonal-orthorhombic structural transition as well as a paramagnetic (PM)-antiferromagnetic (AFM) transition at the same temperature. Using either chemical doping/substitution or applied external pressure, non-superconducting AFM parent compound can be driven to a superconducting (SC) state. The phase diagrams of chemically doped Ba-122 materials are shown in Fig. 2.2, which is strikingly similar to those of several other classes of unconventional superconductors, including cuprates and heavy-fermion superconductors [2], all showing a SC dome proximity to a phase with magnetism. One can see that both hole doping on the Ba site [7] and transition-metal (TM = Co [22], Ni, Rh, Ru [23], Pd, Ir, Pt *et al*.) electron doping (Ru substitution is isovalent) on the Fe site [2], as well as isovalent P doping on the As site [24], succeeded in inducing SC, which is in strong contrast to that in high-T_c cuprate superconductors. The K hole-doped Ba122 is the first discovered superconductors in the 122 family, but shows the highest T_c in this system. One important feature in the AFM region of the phase diagram is that the structural transition temperature (T_s) and the magnetic transition temperature (T_N) remain the same upon doping in K-Ba122 although still under some debate, while other substitutions, substitution on Fe sites and P substitution on As sites, result in the separation of T_s and T_N, always with T_s preceding (here, Ru substitution is also under debate) [17].

One important question deserving to be answered is what controls the variety of phase diagrams. The answer is apparently distinct from cuprate, in which density of doped carriers is the common key parameter to control the phase diagram. In other words, what role does doping play in FeSCs? There are three effects, at least, of dopants that can be considered generally [25]: 1. Doping carriers; 2. Introducing disorders/impurities; 3. Applying chemical pressure. It is known that in the paramagnetic/tetragonal phase a major role of doping is changing the Fermi surface by supplying charge carriers or modifying the structural properties by exerting chemical pressure. In the antiferromagnetic/orthorhombic (AFO) phase, Ishida *et al*. carefully investigated the in-plane resistivity and demonstrated that the major effect of doping is to introduce disorders [7].

The phase diagram of 11 materials [20] is also shown in Fig. 2.2(e). The end material FeSe shows SC with T_c ~ 8 K and T_c rises up to ~14 K with 60% Te substitution for Se. On the other hand, both Co and Ni substitution on Fe sites suppress T_c. The region with 10%-40% Te substitution is marked in grey, where no single phase is stable. It is interesting to note the other end of the $FeTe_{1-x}Se_x$ diagram, FeTe, which exhibits an

accompanying tetragonal-monoclinic structural transition and PT-AFM magnetic transition at T_s ~ 70 K. From this side, upon Se substitution AFM ground state in FeTe is suppressed and finally SC is induced, much similar to the case of 122 systems shown above.

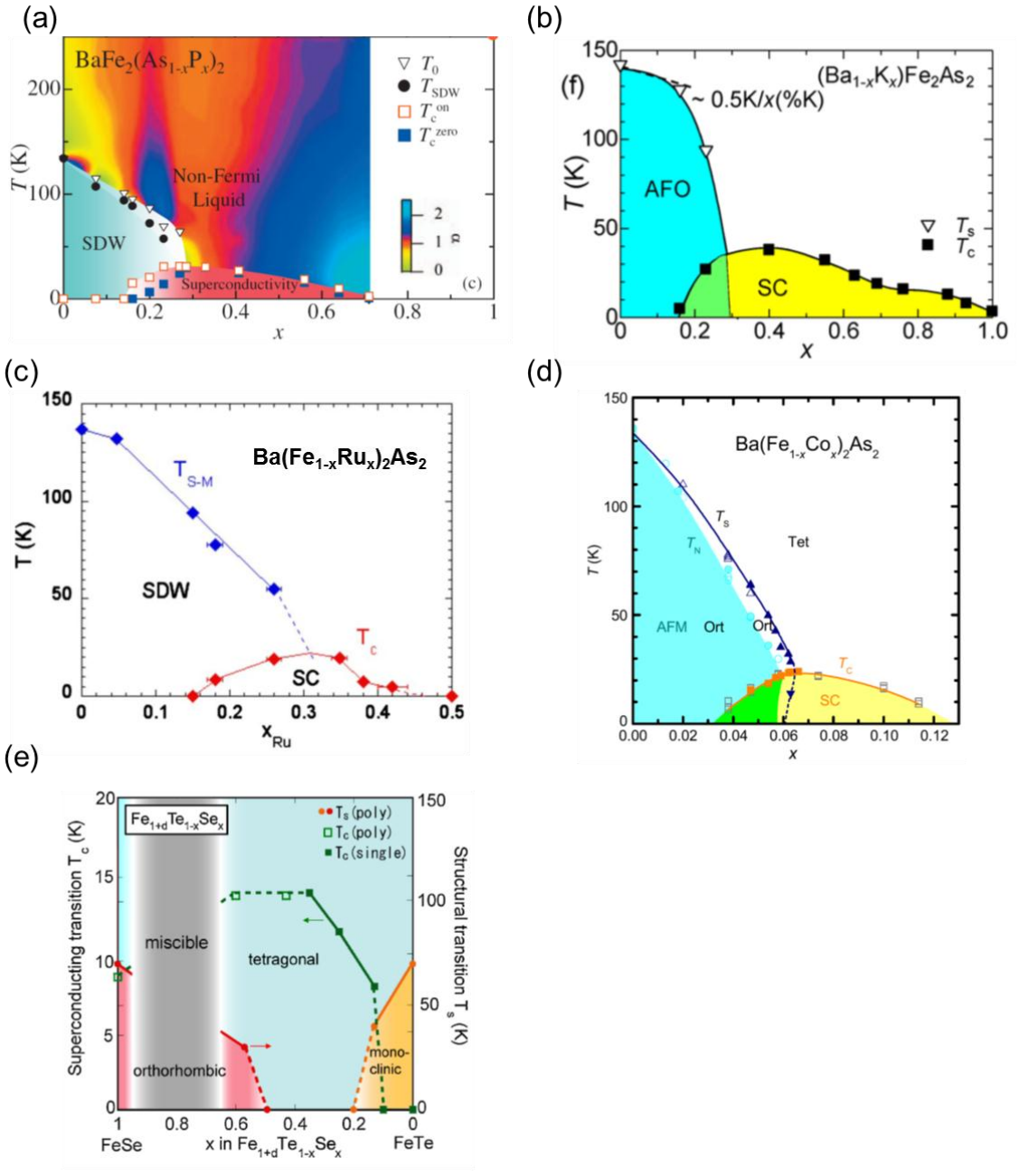

Figure 2.2 Phase diagrams. Ba-122 materials: (a) P substitution for As. Reprinted from [24]. (b) K substitution for Ba. Reprinted from [7]. (c) Ru substitution for Fe. Reprinted from [23]. (d) Co substitution for Fe. Reprinted from [22]. 11 materials: (e) Se substitution for Fe. Reprinted from [20].

2.3 Transport properties

Fig. 2.3(a-d) shows the temperature (T) dependence of the in-plane resistivity for P-[24], K-[26], Ru-[23], and Co-substituted [6] $BaFe_2As_2$ crystals, respectively. The T dependence of resistivity of $BaFe_2As_2$ shows a metallic behavior with the resistivity magnitude at room temperature being several hundred μΩ cm, indicating a bad metal character, distinct from that of parent cuprate clarified as a charge transfer insulator. A kink appeared in the T dependence around 142 K, corresponding to the occurred AFO transition, below which resistivity drops much steeper. It is argued that the sharp T dependence of the conductivity in the AFO phase results from the appearance of contribution from Dirac electrons observed by ARPES [27]. T_s is weakened and SC appears upon various substitutions, as shown in the previous phase diagram. Further investigations on annealed crystals show that the magnitude of the resistivity systematically decreases in the PT phase whereas increases in the AFO phase, indicating the different scattering mechanism in the two phases [7, 25].

Since FeSe single crystals are difficult to be synthesized (very recently, millimeter-size crystals were successfully grown [28]), the data on polycrystals are shown [20] in Fig. 2.3(e), where the metallic T dependence can be seen. In contrast, FeTe shows a semiconductor-like behavior at the high T region, a sudden drop at T_s and a metallic behavior below T_s. The weak semiconductor-like T dependence is usually believed to be related to the large amount of preexisting excess Fe atoms.

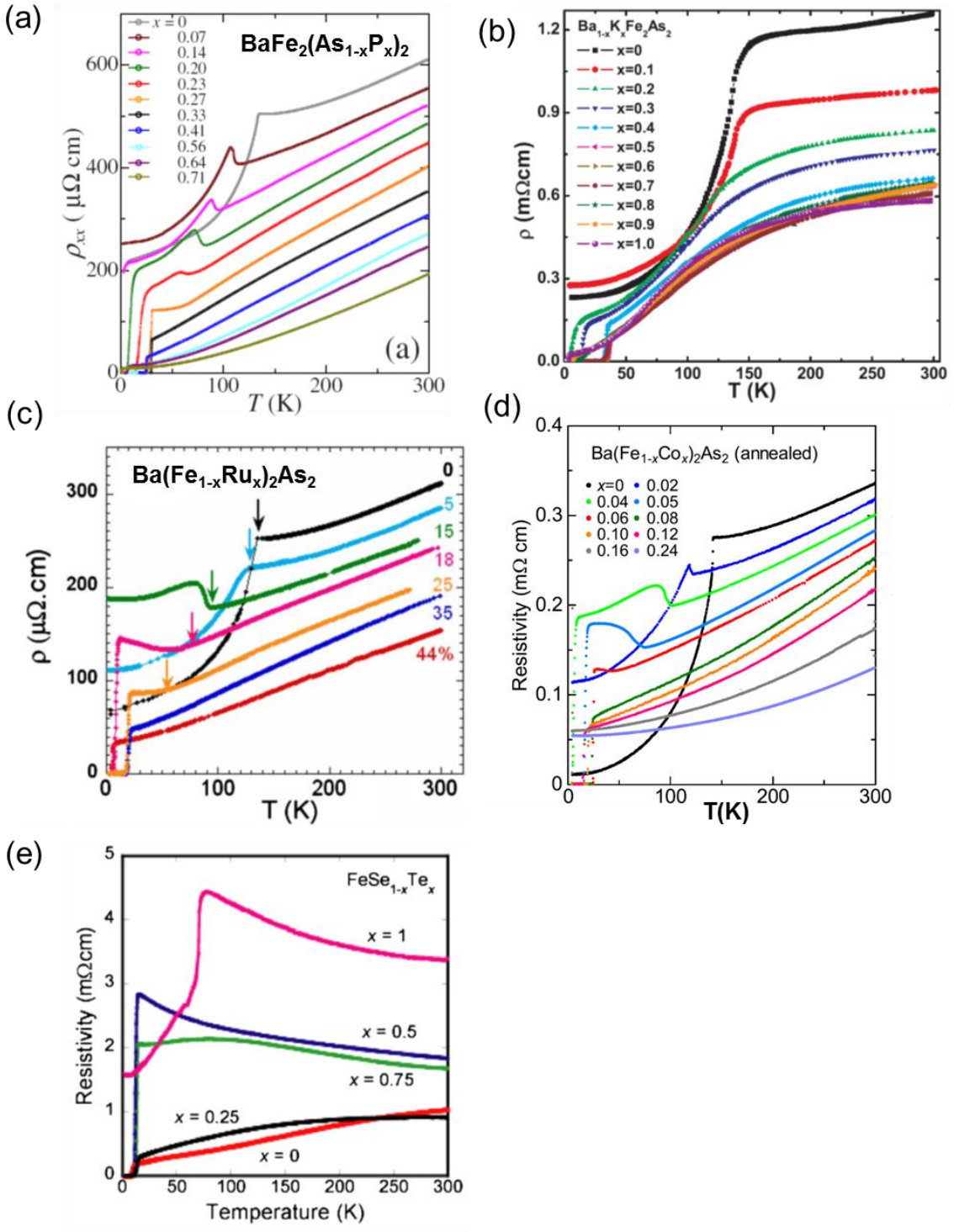

Figure 2.3 Temperature dependence of the resistivity. Ba-122 materials: (a) P substitution for As. Reprinted from [24]. (b) K substitution for Ba. Reprinted from [26]. (c) Ru substitution for Fe. Reprinted from [23]. (d) Co substitution for Fe. Reprinted from [6]. 11 materials: (e) Se substitution for Te. Reprinted from [20].

2.4 Magnetic order of 122 and 11 parent compounds

Both FeTe and Ba122 show an AFM ground phase, but neutron diffraction measurements clarify different spin structures in these two systems. In 122, it is a collinear structure characterized by a $(1/2, 1/2, 1)_T$ wavevector in the tetragonal notation, with moments oriented along the *a* axis, arranged antiferromagnetically along *a* and ferromagnetically along *b* [29]. Here the orthorhombic cell is defined as $c > a > b$, the definition of which we will also use for 11 materials throughout this thesis. The wavevector observed in FeTe is different from that in 122, with an in-plane wavevector of $(1/2, 0)_T$, that is, 45° different in direction and bicollinear in type[29], as shown in the Fig. 2.4. It is interesting to note that both calculations and ARPES measurements of the Fermi surfaces (FSs) of FeTe indicate a nesting nature similar to that of 122 materials [30]. Although it is argued that the AFM order is driven by the Fermi surface nesting in 122, this seems not to be the case in 11.

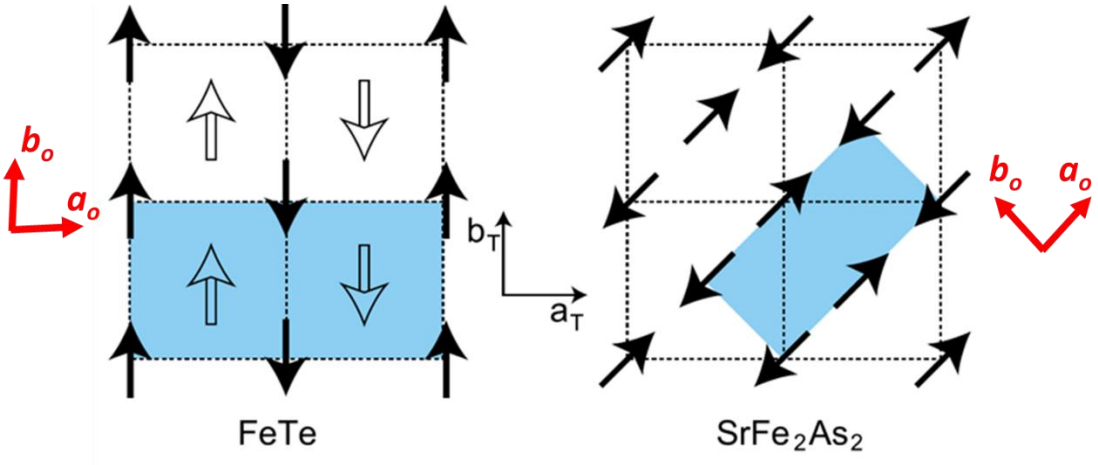

Figure 2.4 Schematic spin structures of FeTe and $SrFe_2As_2$. Reprinted from [29].

2.5 Electronic structure

The band theory shows that a metal's band structure can give a quantitative description of its electronic properties and the energy states proximity to the Fermi energy (E_F) participate in determining most of its properties. The band structures of FeSCs have been calculated using first principal DFT at the first stage. In general, the dominant contribution to the electronic density of states (DOS) at E_F derives from the Fe d-electron orbitals in the FePn/Ch layer. These form several bands that cross E_F, both electron- and hole-like, resulting in a multiband system dominated by Fe 3d character. As an example,

the calculated LDA band dispersion around E_F of $BaFe_2As_2$ is shown in Fig. 2.5 [31], indicating the FSs consisting of two hole pockets centered at the Brillouin zone (BZ) center and two electron pockets centered at BZ corner. These characters are qualitatively well consistent with that observed by ARPES and quantum oscillation measurements [32]. The predicted nesting character between hole FSs and electron FSs accounting for the driving force of the magnetic transition is also observed. One can also see that a hole FS around Z point in the calculation results is strongly warped, suggesting a three dimensional (3D) character. Recent APRES results on P-Ba122 showed a 3D shape of the outer hole pocket around Z point [33], which is consistent with the calculation prediction that the 3D character is sensitive to the pnictogen height.

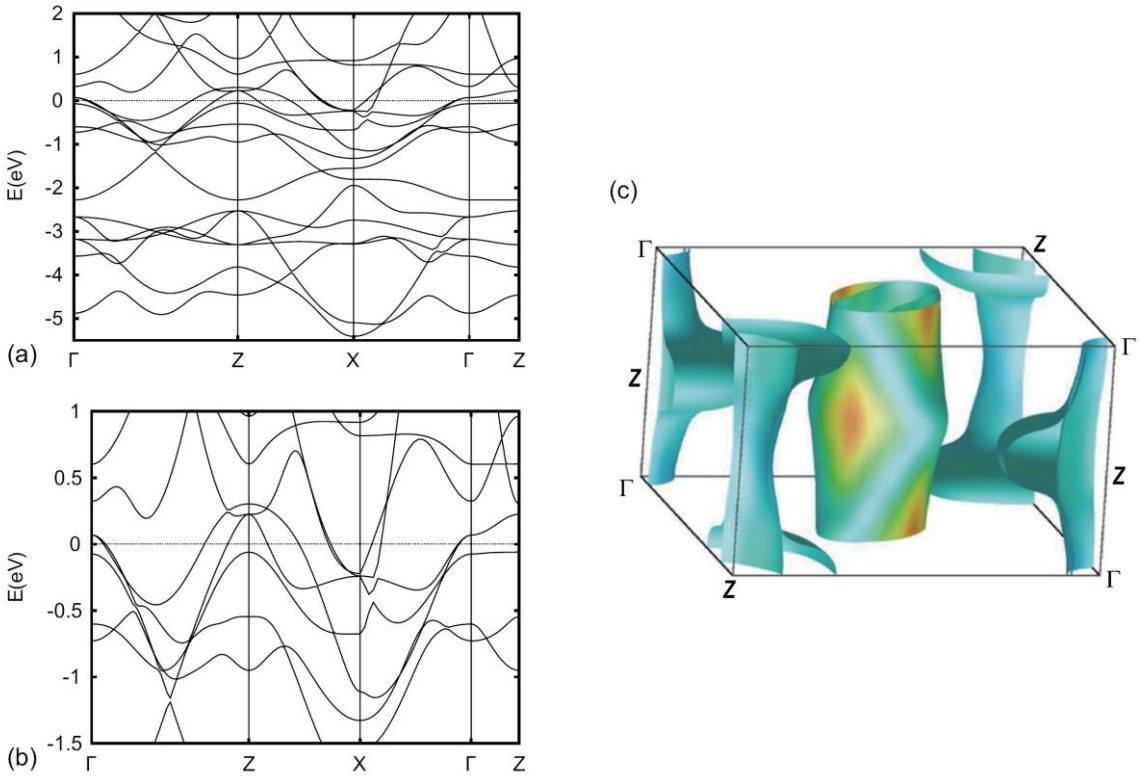

Figure 2.5 Calculated LDA band structure of $BaFe_2As_2$. (a-b) Band dispersions. (c) Fermi surfaces. Colors indicate Fermi velocity. Reprinted from [31].

2.6 In-plane electronic anisotropy in the AFO phase of 122 materials

2.6.1 Resistivity anisotropy

As described above, there is an AFM ground state in most of the parent compounds of FeSCs, which is either accompanied or preceded by a structural transition that breaks C4

rotational symmetry of the high temperature lattice. This is generally expected to result in an anisotropy in the electronic properties, the measurement of which was hampered by twin formation on cooling through T_s. Chu *et al.* first reported the results on in-plane resistivity anisotropy of successfully detwinned samples by applying an uniaxial compressive pressures [5]. The method for detwinning is illustrated in Fig. 2.6. The shorter *b*-axis is favored in the direction of the applied compressive pressure.

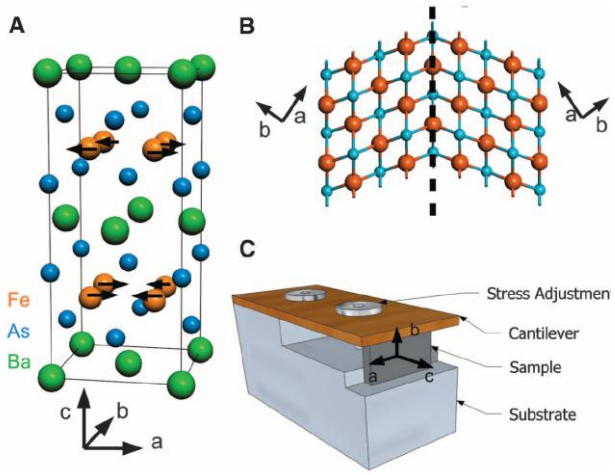

Figure 2.6 Method to detwin single crystals *in-situ* by applying an uniaxial pressure. Reprinted from [5].

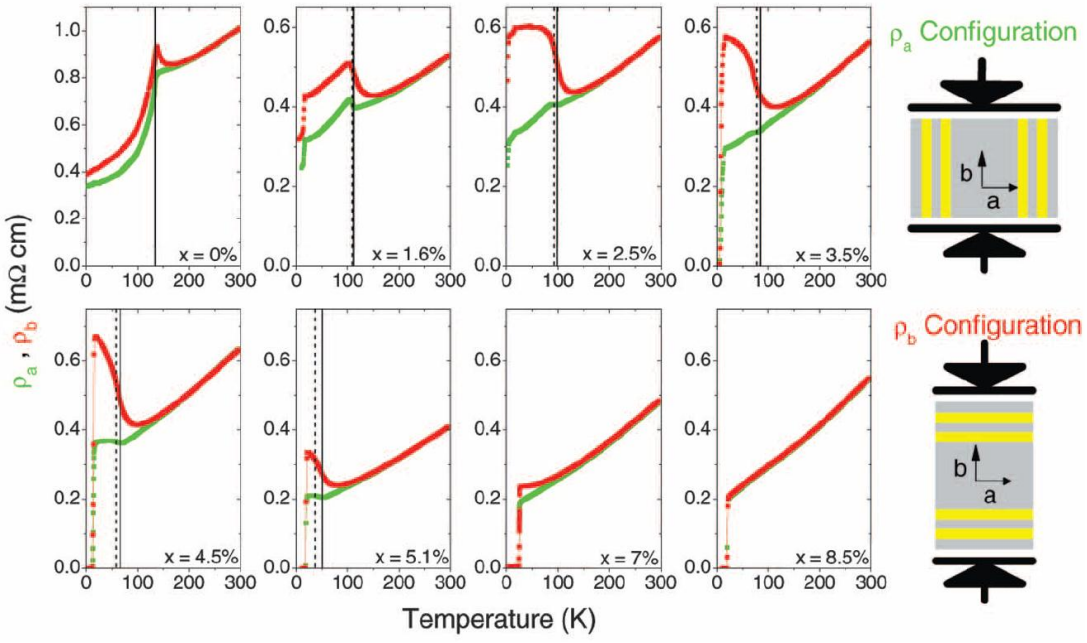

Figure 2.7 Temperature dependence of the in-plane resistivity, ρ_a and ρ_b, for $Ba(Fe_{1-x}Co_x)_2As_2$ detwinned single crystals. Reprinted from [5].

Several important features can be seen from the result of ρ_a and ρ_b in $Ba(Fe_{1-x}Co_x)_2As_2$ shown in Fig. 2.7. 1. Upon cooling, ρ_b is larger than ρ_a, which is unanticipated from the fact that *b*-axis is the shorter and ferromagnetic one, naively thought to be of larger conductivity. 2. The non-monotonic doping dependence of resistivity anisotropy is also striking, first increasing with Co doping, then decreasing and vanishing around 8.5%. ρ_b/ρ_a reaches a maximum of 2 around 3.5%. This large anisotropy and non-monotonic doping dependence is in stark contrast to the structural orthorhombicity, characterized by $(a-b)/(a+b)$, which is small (0.7% for parent compound at 7 K) and monotonically decreases with increasing Co concentration. Thus, it is difficult to explain the large resistivity anisotropy by the structural orthorhombicity. 3. Another notable feature is a finite in-plane resistivity anisotropy appearing well above T_s. Although this is sometimes interpreted as evidences for the nematic electronic state above T_s, it can also be simply explained by the effect of uniaxial pressure which may break the fourfold symmetry of the crystal field [14].

Recently, Ishida *et al*. presented the results on in-plane resistivity anisotropy measured on detwinned $Ba(Fe_{1-x}Co_x)_2As_2$ single crystals with quality much improved by annealing [6], evidenced by the largely reduced residual resistivity (RR) by one order and increased residual resistivity ratio (RRR), as shown in Fig. 2.8. From the results, one can see that the in-plane resistivity becomes almost isotropic in the undoped $BaFe_2As_2$ after annealed. It is found that the anisotropy in resistivity almost arises from the anisotropy in RR

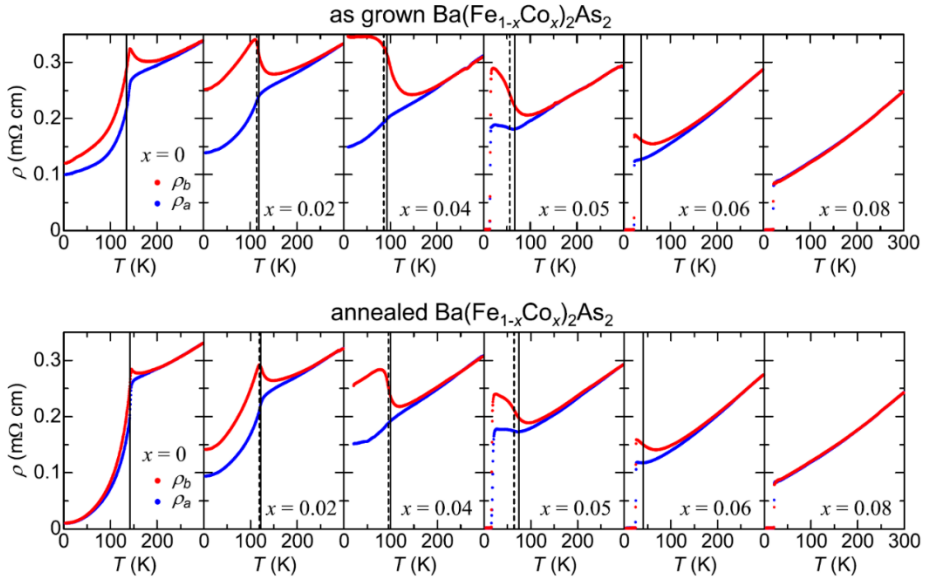

Figure 2.8 Temperature dependence of the in-plane resistivity ρ_a and ρ_b of as-grown and annealed $Ba(Fe_{1-x}Co_x)_2As_2$ detwinned single crystals**.** Reprinted from [6].

component which increases linearly with the Co composition in the “pure” AFO phase. It is also worth noting that the results in K hole-doped systems show a vanishingly small in-plane resistivity anisotropy.

2.6.2 Anisotropic charge dynamics revealed by optical spectroscopy

Optical studies of detwinned samples using polarized light can provide important insights to the effects of the AFO transition on the charge dynamics and electronic structure. As shown [11] in Fig. 2.9, pronounced anisotropy observed in the spectra of non-doped $BaFe_2As_2$ arises from an anisotropic energy gap opening. Since the effective carrier numbers (n/m^*) and the carrier scattering rate ($1/\tau$) can be extracted separately from analysis of a Drude component, it is suggested [10] that the anisotropy in resistivity originates from the anisotropic carrier scattering time rather than anisotropic effective mass of carriers (Fig. 2.10(h-j)). It is proposed that the doped Co atom polarizes its surroundings and works as an anisotropic scattering center (Fig. 2.10(k)).

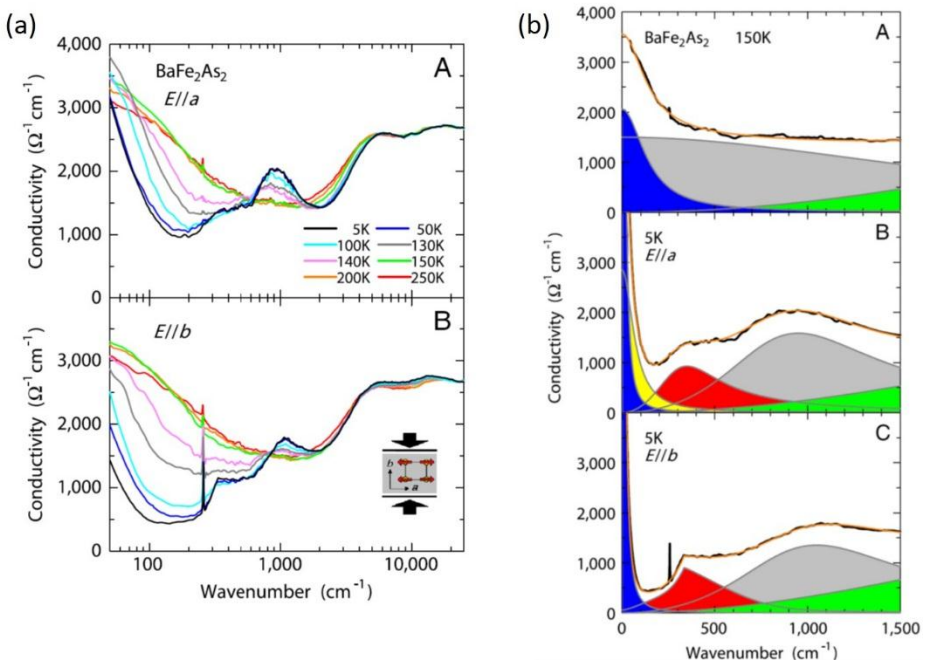

Figure 2.9 (a) Temperature evolution of the optical conductivity spectrum of detwinned $BaFe_2As_2$ for polarization parallel to *a*- and *b*- axes. (b) Decomposition of the low-energy conductivity spectrum. Reprinted from [11].

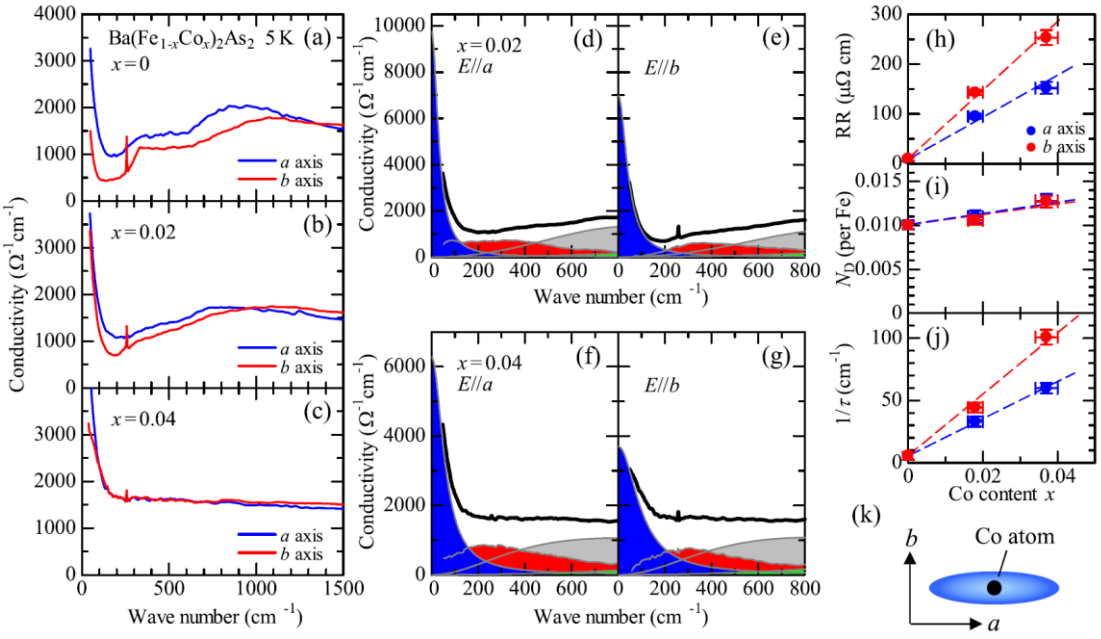

Figure 2.10 Anisotropic optical conductivity spectra at T = 5 K in the low-energy regions for detwinned $Ba(Fe_{1-x}Co_x)_2As_2$. Reprinted from [10].

2.6.3 Electronic anisotropy determined by ARPES

ARPES is a powerful method that can give a direct description of the band structure and FS topology. Measurements on detwinned crystals of $BaFe_2As_2$ revealed the anisotropic reconstructed FSs in the two orthorhombic principal direction correspondingly with the broken fourfold symmetry [13]. A summary of measured FSs is shown in Fig. 2.11(a). The most anisotropic features on the FS are the bright spots along Γ-X and petals along the Γ-Y high-symmetry lines (magenta in color), both arising from the anti-crossing between hole and electron bands. Furthermore, the energy splitting between the originally degenerate d_{yz} band along Γ-X and d_{xz} band along Γ-Y in the SDW state was also revealed in Fig. 2.11(b). The d_{yz} band shifts up and crosses E_F whereas the d_{xz} band shifts down, resulting an unbalanced occupation in the d_{yz} and d_{xz} orbitals. However, it was pointed out that this anisotropy in FS topology does not seem to sufficiently explain the observed large in-plane resistivity anisotropy. On the other hand, the impurity-induced-anisotropy scenario proposed above can give a simple but relatively reasonable explanation for the observed resistivity anisotropy. It is unclear to what extent the electronic anisotropy described above is generic for FeSCs, motivating experiments in other related families.

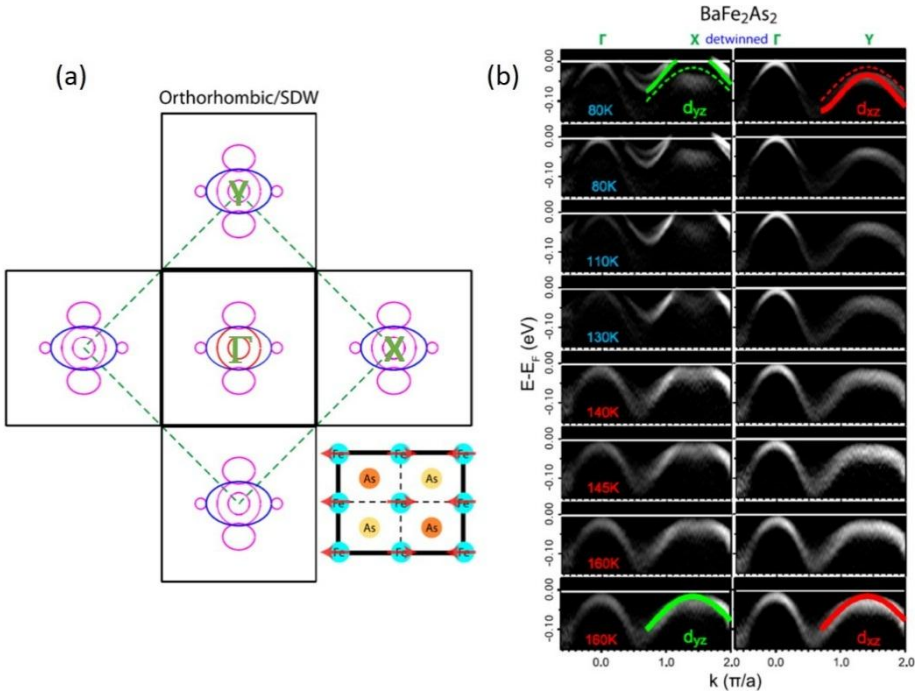

Figure 2.11 (a) Anisotropy in the FS topology of the reconstructed SDW state of $BaFe_2As_2$. Red (blue) pockets indicate hole (electron) character, whereas magenta indicates pockets resulting from hybridization of electron and hole features. (b) Temperature dependence of an anisotropic band shift along Γ-X and Γ-Y high-symmetry lines on detwinned $BaFe_2As_2$. X and Y refer here to orthorhombic *a*- and *b*- directions, respectively. Reprinted from [13].

Chapter 3

Experimental Methods and Principles

3.1 Single crystal growth and transport measurements

In this section, the method of growing 11 single crystals and measuring the transport properties in this thesis shall be introduced.

3.1.1 Crystal growth and characterization

The crystal structure of FeSe exhibiting SC is tetragonal at room temperature, corresponding to the phase FeSe rt in the Fe-Se binary phase diagram [34], as shown in Fig. 3.1(a). Due to the non-existence of a common phase boundary line between the liquid phase and the solid FeSe rt phase, it is thought to be impossible to grow a single crystal of FeSe directly from an Fe-Se liquid solution. Therefore, several other growth methods such as the alkali-halide-flux growth method and the vapor self-transport growth method have been tried to grow millimeter-size single crystals [28]. On the other hand, large single crystals of non-superconducting tetragonal FeTe can be successfully grown [35] through the melt growth techniques, among which the Bridgman method is the typical and the most frequently employed one.

Ru-substituted Ba122 single crystals were grown via a self-flux method [36]. The

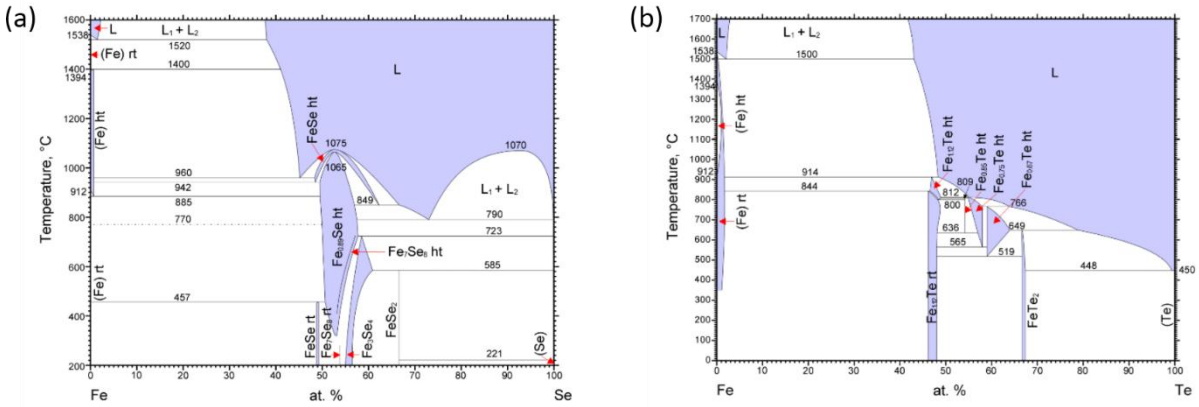

Figure 3.1 (a) Fe-Se binary alloy phase diagram. Reprinted from [34]. (b) Fe-Te binary alloy phase diagram. Reprinted from [35].

crystals measured in this thesis were packed within a quartz tube together with BaAs powder and annealed at 800° for 72 hours. It is know that the annealing process markedly improves the quality of iron pnictide crystals [37], e.g., $BaFe_2As_2$. It was also found that annealed samples show an increase in T_c.

Bridgman method

The Bridgman method involves heating polycrystalline material above its melting point and slowly cooling it from one end where a seed crystal is located. As the temperature of the side of the seed crystal first falls below the solidification temperature, a single crystal with the same crystallographic orientation as the seed crystal is grown on the seed and is progressively formed along the length of the container.

We employed a method similar to the Bridgman one to grow single crystals of $Fe_{1+x}Te_{1-y}Se_y$. The typical synthesis scheme is as follows.

1. Fe, Se and Te powders are weighed, mixed with the desired molar ratio, and then loaded into a cleaned quartz tube. After evacuating and sealing, the tube is put into the furnace and heated at 800° for 20 hours for polycrystal synthesis.
2. The reacted materials are crushed and then mixed, sealed into an evacuated quartz tube as in step 1. Because empirically the quartz tube with Se sealed inside tends to crack easily through high temperature heating, double sealing, that is, one quartz tube is sealed by another one, is necessary.
3. The doubly sealed tubes are put into the furnace with a temperature gradient, heated up to 1000 ~ 1100° for 6 hours, and then cooled to 700 ~ 800° at a cooling rate of 1 ~ 3°/hour, followed by natural furnace cooling.

Although no seed crystal is used in this method unlike the conventional Bridgman method, the cold side of the quartz tubes is inverted-triangular shaped, which can help

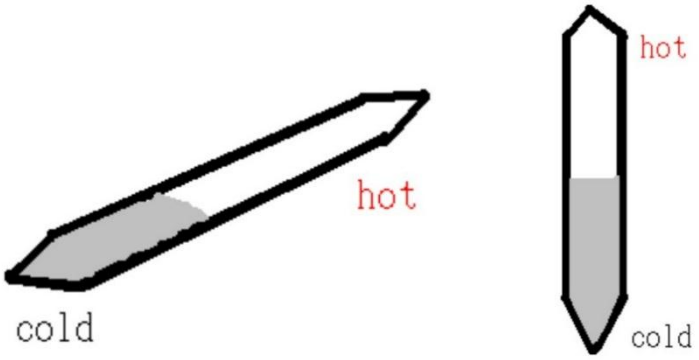

Figure 3.2 Schematic drawings of the horizontal and vertical Bridgman growth.

align the crystallographic orientation of initially nucleated grains and thus play a similar role to that of seed crystal. Instead of moving the tubes or the furnace to achieve a directional solidification in the conventional Bridgman technique, the natural temperature gradient in the furnace is used and a translation of the temperature gradient is implemented by controlling (decreasing) the furnace power/temperature. We tried both the vertical and horizontal configurations for single crystal growth. Figure 3.3 shows the pictures of the crystals grown with the different configurations. Both can grow large-size single crystals. The crystals grown in the horizontal geometry show very shiny, mirror-like cleavage surface corresponding to the a-b plane and high crystalline quality evidenced by the Laue pattern, whereas the ones grown in the vertical geometry show textured surfaces associated with slight misorientation of grains. This is what often happens in the vertical configuration, due to the developed strain effects on the growth interface by the constrained cross section of a quartz tube.

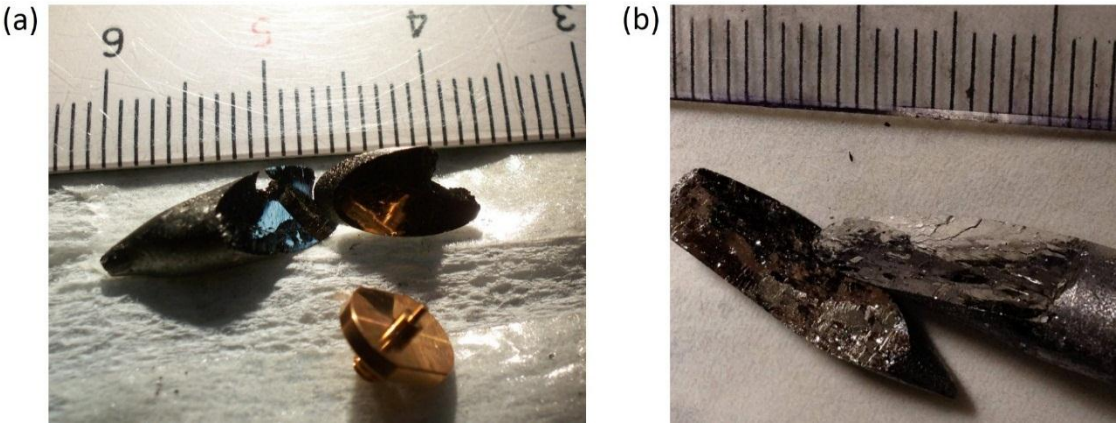

Figure 3.3 Photographs of 11 single crystals grown by the horizontal Bridgman configuration (a) and the vertical Bridgman configuration (b).

Back-reflection Laue

We use the back-reflection Laue method to confirm the crystalline quality and to determine the crystal orientation. Figure 3.4 shows Laue photographs for the ab-plane of FeTe and $Ba(Fe_{0.65}Ru_{0.35})_2As_2$ single crystals, respectively, where the tetragonal a/b axis is shown by a red broken line. The small and clear spots in the Laue photograph indicates good crystalline quality and the fourfold symmetry of the pattern corresponds to the tetragonal crystal structure at room temperature.

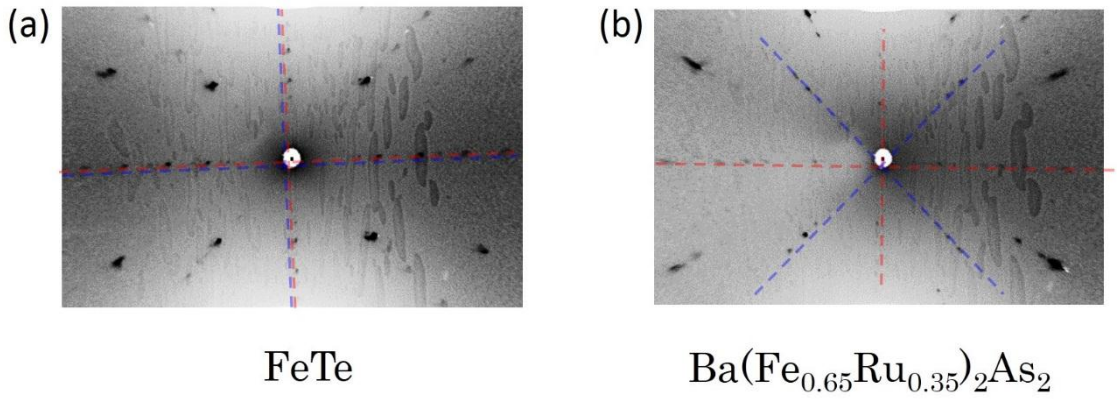

Figure 3.4 Laue patterns of FeTe and $Ba(Fe_{0.65}Ru_{0.35})_2As_2$ single crystals.

Chemical analysis

In this study, chemical compositions of the samples were determined by an energy dispersive x-ray spectrometer (EDXS). Compositions of the $Fe_{1+x}Te_{1-y}Se_y$ crystals grown by the horizontal configuration are listed in the Table 3.1. The actual composition is used in the following paragraphs.

Table 3.1 Compositions of $Fe_{1+x}Te_{1-y}Se_y$ single crystals

Nominal *y*	Composition		
	Fe	Te	Se
0.4	1.00	0.59	0.41
0.2	1.06	0.80	0.20
0.1	1.09	0.90	0.10
0.08	1.07	0.92	0.08
0.05	1.08	0.95	0.05
0	1.08	1	0

3.1.2 Resistivity measurement

A standard four-probe method was used for the regular resistivity measurement and a Montgomery method was used for the in-plane resistivity anisotropy measurement on the detwinned samples which allows the simultaneous measurement of the in-plane two resistivity components along the principle crystal axes. The transport measurements were performed in a Quantum Design physical property measurement system (PPMS).

Four-probe method

A schematic figure of the four-probe method is shown in Fig. 3.5. Samples were cut into a rectangular shape and four electrodes are attached for current flow and voltage measurement. In this study, the magnitude of the resistivity is an important quantity for discussion. In order to improve the accuracy of the measurement, a long slender sample is advantageous, typically with the dimension 2×0.5×0.1 mm^3 and repeated measurements of several times on different pieces are necessary.

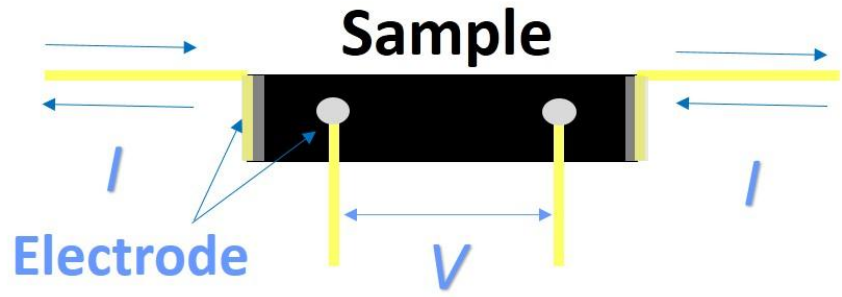

Figure 3.5 Schematic picture of the electrode configuration for resistivity measurement.

Montgomery method [38]

A sample was cut into the form of a rectangular prism with the larger face in the cleaved *ab* plane, the edges of which are along the directions of the two resistivity components to be measured (ρ_a and ρ_b). The dimensions were denoted as l_a and l_b, as shown in Fig. 3.6, and l_c along the c axis. Typical dimension is 1.5×1.5×0.5 mm^3.

The current and the voltage electrodes were attached at the four corners of the a-b face and two sets of voltage and current were measured with the two configurations shown in Fig. 3.6. Then we define

$$R_a = \frac{V_a}{I_a},\ R_b = \frac{V_b}{I_b}$$

It is shown that the rectangular sample cut in the form above with dimensions, l_a, l_b, and l_c, and the resistivity along the principal crystal axes, ρ_a, ρ_b, ρ_c, can be mapped to an equivalent isotropic one with dimensions, l_a', l_b', and l_c', and the resistivity ρ'. The relations are

$$l_i' = l_i(\rho_i/\rho)^{1/2}\ (i = a, b, c), \quad (3.1.1)$$

$$\rho' = \rho_a\rho_b\rho_c, \quad (3.1.2)$$

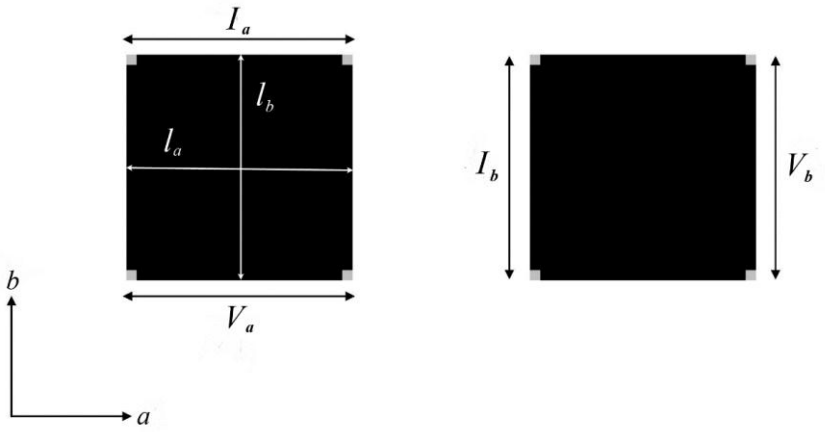

Figure 3.6 Schematic of electrode configurations for the Montgomery method. Reprinted from [39].

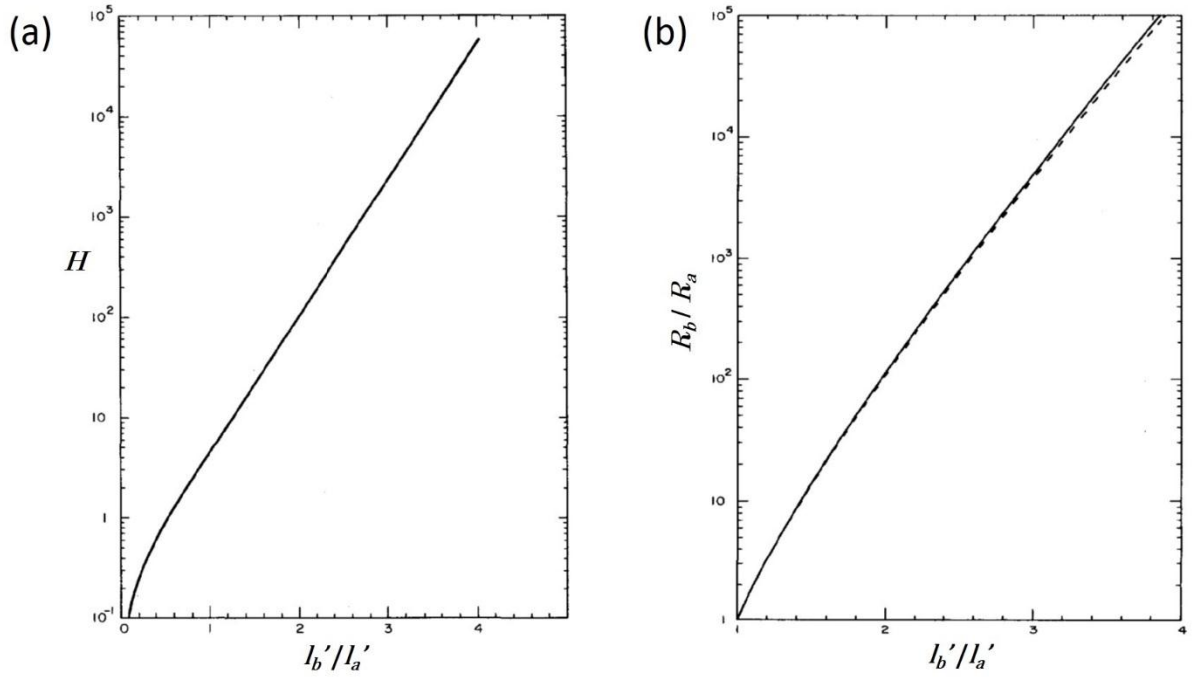

Figure 3.7 (a) H as a function of (l_b'/l_a'). (b) Relationship between (R_b/R_a) and (l_b'/l_a'). Solid line is for a thin sample. Reprinted from [38].

ρ' can also be calculated using the following formula:

$$\rho' = HER_a,$$

where H is a function of l_b'/l_a', as shown in Fig. 3.7(a). E is an effective thickness, which is equal to the actual thickness l_c', when $l_c' \ll (l_a' l_b')^{1/2}$. This is the case for a thin sample we measured.

Then we can get

$$\rho' = Hl_c'R_a = Hl_cR_a\sqrt{\frac{\rho_c}{\rho'}}\ . \qquad (3.1.3)$$

From the equation (3.1.1-3.1.3), we have

$$\sqrt{\frac{\rho_b}{\rho_a}} = (\frac{l_b'}{l_a'})(\frac{l_a}{l_b}),$$

$$\sqrt{\rho_a\rho_b} = Hl_cR_a.$$

The observed R_b/R_a can be converted to l_b'/l_a' according to the relationship shown in Fig. 3.7 (b), which would be further used for the calculation of H. Then ρ_a and ρ_b can be calculated.

In this study, the electrodes were extended along each of the four edges normal to the principle surface in the *ab* plane, which results in the elimination of the contribution of the resistivity along *c* axis and application of the thin-sample formulas. This is usually called two-dimensional Montgomery method.

Here we also note the following equivalences in notation:

Quantities shown above:	R_a	R_b	l_a	l_b	l_c	ρ_a	ρ_b	ρ_c	ρ'	l_a'	l_b'	l_c'
Notations in Ref[38]:	R_1	R_2	l_1'	l_2'	l_3'	ρ_1	ρ_2	ρ_3	ρ	l_1	l_2	l_3

3.1.3 Hall coefficient measurement

The Hall resistivity were measured with the electric current along the *ab* plane and the

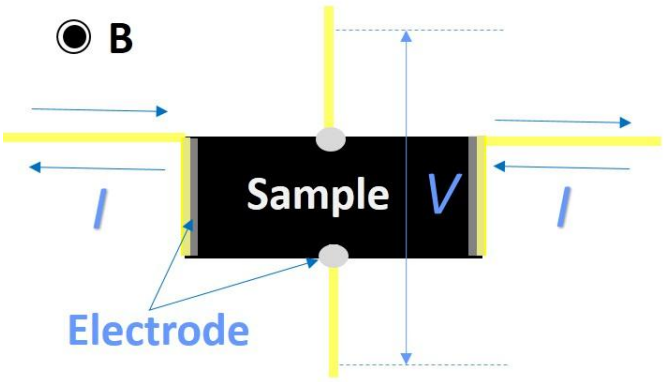

Figure 3.8 Schematic picture of the electrode configurations for Hall coefficient measurement.

magnetic field applied along the *c* axis. The schematic figure is shown in Fig. 3.8. Within the measured range of -5 T-5 T, the Hall resistivity is proportional to *B*, from which the Hall coefficient is obtained.

3.1.4 Detwinning method

As introduced in the previous chapter, a magneto-structural transition appears upon cooling in most of the parent compounds of the iron-based superconductors, breaking a rotational symmetry of the high-temperature phase. On cooling through the transition temperature (T_s), materials tend to form structural twins, which are of course a barrier to intensively study the in-plane electronic anisotropy. Thus far, it is shown that the application of uniaxial stress (either compressive or tensile) is an effective method to detwin crystals [12, 14]. By applying a uniaxial compressive stress along one principal crystal axis in the phase with broken rotational symmetry, the shorter *b* axis would be favored. In the following paragraph, details of detwinning crystals *in-situ* are described.

First, in order to cut samples with the edges along the orthorhombic (monoclinic) principal *a*/*b* axis, the sample direction is confirmed by the back-reflection Laue method. It is known that the orthorhombic *a*/*b* axes in the iron pnictides are oriented by 45° to the tetragonal *a*/*b* axes while the monoclinic and tetragonal *a*/*b* axes stay the same in iron telluride. Thus the direction along which samples were cut is 45° distinct between the two families, shown by the respective blue lines in Fig. 3.4.

After cutting, detwinning devices were used to apply a uniaxial compressive stress *in-situ* so that the intrinsic electronic anisotropy of single crystals can be studied.

Transport measurements

The uniaxial pressure cell designed for the transport measurement is shown in Fig. 3.9 [39]. After having the sample stand in the cell, a uniaxial compressive stress can be applied to the samples if the spring is compressed by the screw. Aluminium foil is used to make four electrodes at the corners and the Montgomery method was employed for the resistivity measurement. The advantage of this method is that the resistivity along the *a*- and *b*-axes can be simultaneously measured without releasing pressure. The pressure can be roughly estimated from the length of the spring [40].

ARPES measurements

The detwinning device for ARPES measurement was designed by Dr. Shin-ichiro Ideta, as shown in Fig. 3.10. Through twisting the screw properly, a compressive stress can be applied to the samples located on the top of the device for detwinning, which allows us to cleave samples *in-situ*.

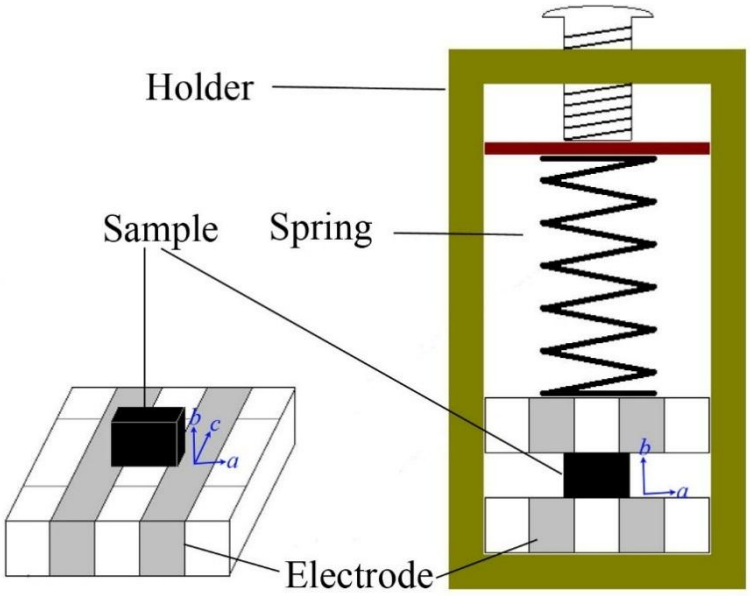

Figure 3.9 Uniaxial pressure cell for detwinning crystals and the electrodes configuration for the Montgomery resistivity measurement. Reprinted from [39].

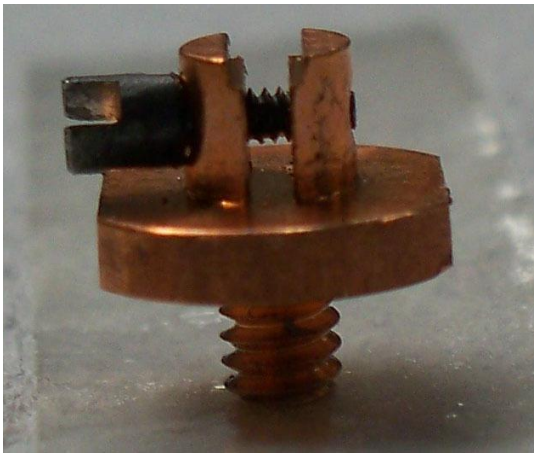

Figure 3.10 Detwinning device for ARPES measurement.

3.2 Photoemission spectroscopy

Photoemission spectroscopy (PES) is to detect the energy distribution of electrons which are excited by absorption of photons from the monochromatized light source. In the three-step model, PES processes can be classified into the following three independent processes [41].

1. Photoionization takes places: locally the photo is absorbed and an electron is excited.
2. This electron escapes through the sample to the surface.
3. The electron escapes through the surface into the vacuum where it is detected.

3.2.1 Basic principles [41-43]

3.2.1.1 General formulation

PES is one of the most powerful tools to investigate the electronic structure of solids, the principle of which is illustrated in Fig. 3.11. When an electron in the solid absorbs a photon of sufficiently high energy $h\upsilon$, it is emitted as a photoelectron. From the energy conservation, the kinetic energy E_{kin}^{vac} is written as

$$E_{kin}^{vac} = h\upsilon - \Phi - E_{\mathrm{B}} \ ,$$

where E_{kin}^{vac} is measured from the vacuum level (E^{vac}), Φ is the work function of the sample, and E_{B} is the binding energy measured for the Fermi level (E_{F}) or chemical potential (μ).

In the one-electron approximation, E_{B} is equal to the negative Hartree-Fock orbital energy,

$$E_{\mathrm{B}} = -\epsilon_k \ ,$$

which is sometimes called Koopmans's binding energy. The assumption is valid when the wave functions of both the initial and final states can be expressed by single Slater determinants of the N- and (N-1)-electron systems, respectively, and the one-electron wave function do not change by the removal of the electron. If one applies this approximation, the photoemission spectrum can be expresses as

$$I(E_{\mathrm{B}}) \propto \sum_k \delta(E_{\mathrm{B}} + \epsilon_k) \propto N(-E_{\mathrm{B}}) \ .$$

Thus, when the one-electron approximation is valid, the photoemission spectrum is proportional to the density of the occupied one-electron states $N(E)$.

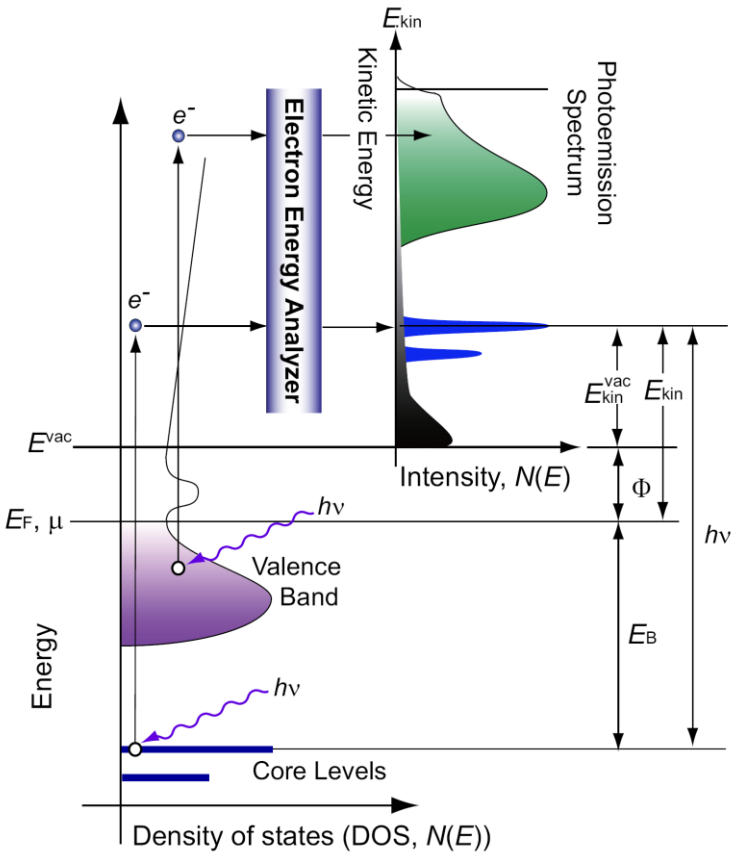

Figure 3.11 Schematic diagram of the principle of photoemission spectroscopy. This shows the relation between the energy levels in a solid and the electron energy distribution produced by photons with energy $h\upsilon$. Reprinted from [41].

3.2.1.2 Angle-resolved photoemission spectroscopy

Angle-resolved photoemission spectroscopy (ARPES) can probe both the energy and the momentum of electrons in the solids. In the photoemission by low-energy photons, the momentum of incident photons $h\upsilon/c$ can be neglected compared to the size of Brillouin Zone (BZ). Therefore, the following relationship is satisfied between the wave vector of the initial state ($\boldsymbol{K}^i$) and that of the final state ($\boldsymbol{K}^f$) due to the conservation of the electron wave number before and after the photoexcitation:

$$\boldsymbol{K}^f = \boldsymbol{K}^i + \boldsymbol{G}$$

where $\boldsymbol{G} = (2n_x\pi/a, 2n_y\pi/a, 2n_z\pi/a)$ is a reciprocal lattice vector and n_x, n_y, n_z are integers.

When the photoelectron is emitted, the wave vector perpendicular to the surface ($\boldsymbol{K}_{\perp}^{f}$), is modified by the potential barrier of the so-called inner potential (V_0), whereas the wave vector parallel to the surface is conserved. Therefore, we can get

$$\boldsymbol{k}_{\parallel} = \boldsymbol{p}_{\parallel}/\hbar = \boldsymbol{K}_{\parallel}^{f} = \boldsymbol{K}_{\parallel}^{i} + \boldsymbol{G}_{\parallel} , \tag{3.2.1}$$

where $\boldsymbol{k}_{\parallel}, \boldsymbol{p}_{\parallel}$ is the wave vector and momentum parallel to the surface of the emitted electron. Since $\boldsymbol{p}_{\parallel} = (p_x, p_y)$ is related to the polar emission angle θ, ϕ and the photoelectron kinetic energy E_{kin}^{vac} through

$$p_x = \sqrt{2mE_{kin}^{vac}}\sin\theta\cos\phi \tag{3.2.2}$$

$$p_y = \sqrt{2mE_{kin}^{vac}}\sin\theta\sin\phi \tag{3.2.3}$$

where *m* is the free electron mass. Summarizing equations (3.2.1-3.2.3), we can directly obtain both the energy $E \equiv -E_{\mathrm{B}}$ and the parallel momentum $\boldsymbol{K}_{\parallel}^{i} = (K_x^i, K_y^i)$ of the hole produced in the sample by the photoemission process as

$$K_x^i = \frac{\sqrt{2m(h\upsilon - \Phi - E_{\mathrm{B}})}}{\hbar}\sin\theta\cos\phi + \frac{2n_x\pi}{a}$$

$$K_y^i = \frac{\sqrt{2m(h\upsilon - \Phi - E_{\mathrm{B}})}}{\hbar}\sin\theta\sin\phi + \frac{2n_y\pi}{a}$$

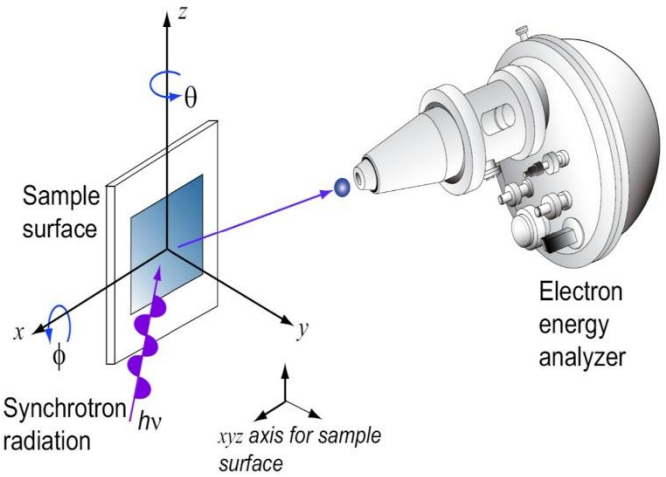

Figure 3.12 Typical experimental geometry of ARPES measurement between sample surface and the analyzer. Reprinted from [41].

where n_x, n_y are integers. If the material under study is a two-dimensional system such as high-T_c cuprate, E and $\boldsymbol{K}_{\parallel}^{i}$ yield enough information to map the energy-momentum dispersion of the band structure through the ARPES experimental geometry shown in Fig. 3.12. If it is a system with three-dimensional character, the determination of $\boldsymbol{K}_{\perp}^{i}$ is necessary. For the determination of $\boldsymbol{K}_{\perp}^{i}$, which is not conserved during the photoemission process, a different approach is required. Suppose a nearly-free-electron description can be adopted for the final Bloch state,

$$E^{f} = \frac{(\boldsymbol{p}^{f})^2}{2m} + E_0$$

where E_0 is the energy bottom of the free electron band. Because $E^{f} = E_{kin}^{vac} + \Phi + \mu$, we can obtain

$$\boldsymbol{K}_{\perp}^{f} = \frac{\sqrt{2m(E_{kin}^{vac}\cos^2\theta + V_0)}}{\hbar} = \boldsymbol{K}_{\perp}^{i} + \frac{2n_z\pi}{a}$$

where $V_0 = \Phi + \mu - E_0$, is the inner potential. If V_0 is known, one can obtain the corresponding value of $\boldsymbol{K}_{\perp}^{i}$.

3.2.1.3 Spectral function and Self-energy

Beyond the one-electron approximation, one takes many-body effects into account. In this more generalized description, photoemission process is regarded as the removal of an electron from the ground state $|\Psi_g^N>$ of the N - electron system with the energy E_g^N, leaving the system in an excited state $|\Psi_i^{N-1}>$ of the (N -1) - electron system with the energy E_i^{N-1}. The photoemission spectrum $A(\boldsymbol{k}, \omega)$, corresponding to the single-particle excitation spectrum of the system, is expressed as

$$A(\boldsymbol{k}, \omega) = \sum_i |<\Psi_i^{N-1}|c_{\boldsymbol{k}}|\Psi_g^N>|^2 \delta(\omega + E_i^{N-1} - E_g^N)$$

where c_k is the annihilation operator of an electron with the momentum k. In the method of quantum field theory, one-particle Green's function can be written as

$$G(\boldsymbol{k},w) = \sum_i |<\Psi_i^{N-1}|c_{\boldsymbol{k}}|\Psi_g^N>|^2\left[\frac{P}{\omega + E_i^{N-1} - E_g^N} - i\pi\delta\left(\omega + E_i^{N-1} - E_g^N\right)\right] + \sum_i |<\Psi_i^{N+1}|c_{\boldsymbol{k}}^{\dagger}|\Psi_g^N > |^2\left[\frac{P}{\omega + E_i^{N+1} - E_g^N} - i\pi\delta\left(\omega - E_i^{N+1} + E_g^N\right)\right]$$

where P denotes the principal value of the integral. It can be proved that the photoemission spectral function $A(\boldsymbol{k},\omega)$ is related to $G(\boldsymbol{k},w)$ by

$$A(\boldsymbol{k},\omega) = -\frac{1}{\pi}\,\mathrm{Im}\,G(\boldsymbol{k},w)$$

for $w \le \mu$ (chemical potential). In the presence of electron-electron interactions, the single-particle Green's function $G(\boldsymbol{k},w)$ can be given by the self-energy which renormalizes all the interaction between particles,

$$G(\boldsymbol{k},w) = \frac{1}{\omega - \epsilon_{\boldsymbol{k}}^0 - \sum(\boldsymbol{k},w)}$$

Thus, the photoemission spectral function $A(\boldsymbol{k},\omega)$ is given by

$$A(\boldsymbol{k},\omega) = -\frac{1}{\pi}\frac{\mathrm{Im}\sum(\boldsymbol{k},w)}{(\omega - \epsilon_{\boldsymbol{k}}^0 - \mathrm{Re}\sum(\boldsymbol{k},w))^2 + (\mathrm{Im}\sum(\boldsymbol{k},w))^2}$$

Assume that the interacting $G(\boldsymbol{k},w)$ has a pole at $w = E_{\boldsymbol{k}}^*$, it is determined by the equation

$$E_{\boldsymbol{k}}^* - \epsilon_{\boldsymbol{k}}^0 - \mathrm{Re}\sum(\boldsymbol{k},E_{\boldsymbol{k}}^*) = 0$$

We introduce the residue Z_k at the pole, given by

$$Z_{\boldsymbol{k}} = \left(1 - \frac{\partial \mathrm{Re}\sum(\boldsymbol{k},w)}{\partial w}|_{w=E_{\boldsymbol{k}}^*}\right)^{-1}$$

Then, near $w \simeq E_{\boldsymbol{k}}^*$, we can obtain,

$$\omega - \epsilon_{\boldsymbol{k}}^0 - \mathrm{Re}\sum(\boldsymbol{k},\omega) \cong \frac{1}{Z_{\boldsymbol{k}}}(w - E_{\boldsymbol{k}}^*)$$

Therefore,

$$A(\boldsymbol{k},\omega) = -\frac{Z_{\boldsymbol{k}}}{\pi}\frac{Z_{\boldsymbol{k}}\mathrm{Im}\sum(\boldsymbol{k},w)}{(w - E_{\boldsymbol{k}}^*)^2 + (Z_{\boldsymbol{k}}\mathrm{Im}\sum(\boldsymbol{k},w))^2}$$

In the vicinity of E_F, $E_{\boldsymbol{k}}^*$ can be written as $E_{\boldsymbol{k}}^* = v_{\boldsymbol{k}}^*(k - k_F)$, where $v_{\boldsymbol{k}}^*(\equiv|\nabla E_{\boldsymbol{k}}^*|)$ is the renormalized Fermi velocity and $\boldsymbol{k}$ is taken perpendicular to the Fermi surface. Then the momentum distribution curve (MDC) at the Fermi level ($\omega = 0$) is given by

$$A\,(\boldsymbol{k},0) = -\frac{Z_{\boldsymbol{k}}/v_{\boldsymbol{k}}^{*}}{\pi}\,\frac{Z_{\boldsymbol{k}}\mathrm{Im}\sum(\boldsymbol{k},0)\,/v_{\boldsymbol{k}}^{*}}{(k-\,k_F)^2+\,(Z_{\boldsymbol{k}}\mathrm{Im}\sum(\boldsymbol{k},0)/v_{\boldsymbol{k}}^{*})^2}$$

Thus, the MDC is given as a Lorentzian with a full width at half maximum (FWHM) of $\Delta k = 2|Z_{\boldsymbol{k}}\mathrm{Im}\sum(\boldsymbol{k},0)\,/v_{\boldsymbol{k}}^{*}|$, if the $\boldsymbol{k}$-dependence of $Z_{\boldsymbol{k}}$, $\mathrm{Im}\sum(\boldsymbol{k},0)$ and $v_{\boldsymbol{k}}^{*}$ can be neglected. Since the inverse life time of the quasi-particle is given by $1/\tau_{\boldsymbol{k}} = -2Z_{\boldsymbol{k}}\mathrm{Im}\Sigma$, $1/\Delta k$ represents the mean free path $l_{\boldsymbol{k}} = v_{\boldsymbol{k}}^{*}\tau_{\boldsymbol{k}} = 1/\Delta k$.

3.2.1.4 Electron escape depth

PES is a surface sensitive experiment technique. The escape depth of photoelectrons is determined by electron-electron and electron-phonon interactions. Generally, electron-phonon scattering plays a role only at low energies below the phonon frequencies. The escape depth of the electrons λ is then determined largely by electron-electron interaction. The cross-section for electron-electron scattering σ is given by

$$\frac{d^2\sigma}{d\Omega d\varepsilon} = \frac{\hbar^2}{\pi e a_0}\frac{1}{q^2}\mathrm{Im}(-\frac{1}{\epsilon(q,\varepsilon)})$$

where $\epsilon(q,\varepsilon)$ is the dielectric function, $\hbar q$ is the momentum transfer and ε the energy transfer in the scattering process, $a_0 = 0.529$ Å, and Ω is the solid angle into which the

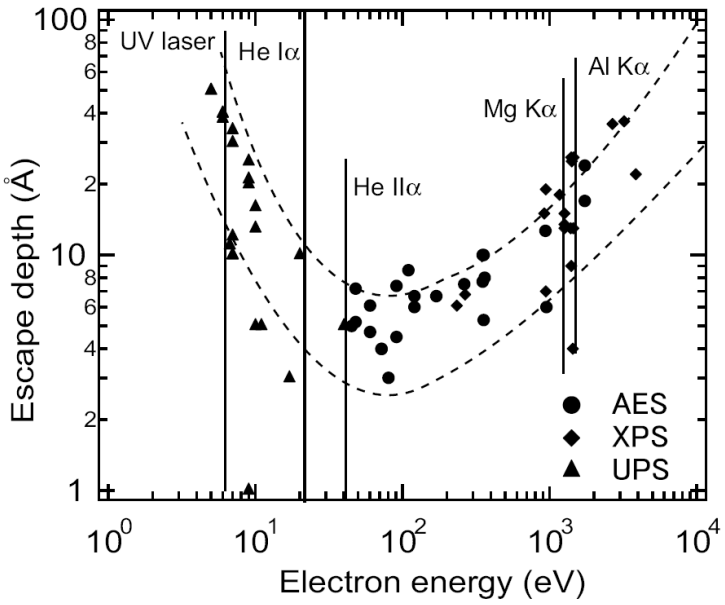

Figure 3.13 Escape depth of electrons in solids. Dashed curves indicate the approximate range of the experimental data. This shows that in case of using He Iα and He II for UPS measurement, escape depth is ~15 and 10 Å, respectively. Laser source is known very bulk sensitive and the escape depth of photoelectrons is 70 ~ 100 Å. Reprinted from [44].

electrons are scattered. Although $\epsilon(q,\varepsilon)$ differs from material to material, the escape depth as a function of energy roughly follows the universal curve, as shown Fig. 3.13 [44], for all materials. In the free-electron case, the inverse escape depth λ^{-1} is described by the mean electron-electron distance r_s, which is roughly equal for all materials, and one obtains

$$\lambda^{-1} \cong \sqrt{3}\frac{a_0 R}{E_{kin}} r_s^{-\frac{3}{2}} \ln\left\{\left(\frac{4}{9\pi}\right)^{2/3} \frac{E_{kin}}{R} r_s\right\}$$

where R = 13.6 eV, and r_s is measured in units of the Bohr radius a_0. Therefore, electron-escape depth λ is given as a function of electron kinetic energy E_{kin} as observed experimentally, and almost all materials show a similar energy dependence of the mean electron escape depth.

3.2.2 Experimental Setup

3.2.2.1 Photoemission measurement system [41]

Basically, photoemission measurements were carried out using a hemispherical analyzer. Fig. 3.14 shows a schematic description of the photoemission measurement system. Samples are introduced in the bank chamber and transferred to the preparation chamber and the main chamber successively. In the ultrahigh vacuum main chamber, the

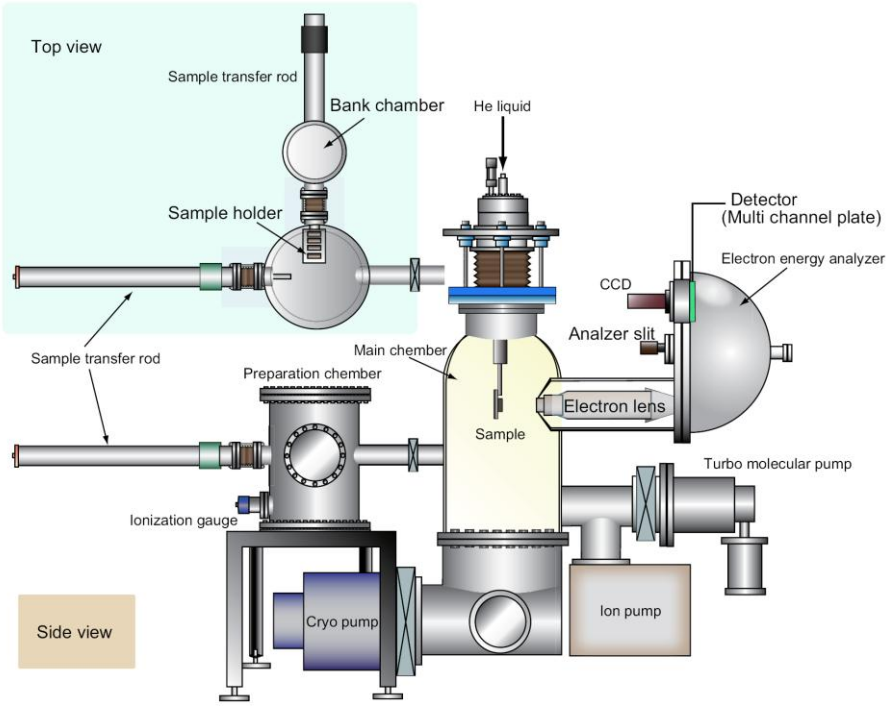

Figure 3.14 Schematic description of the photoemission measurement system. Reprinted from [41].

sample is cleaved and photoelectrons excited by incident photons enter the electron lens and are focused by electrostatic field. The photoelectrons are deaccelerated by a retarding potential eV_R before entering the electron analyzer. The analyzer transmits only photoelectrons with a given energy (pass energy E_P). The relationship between the retarding potential eV_R and the pass energy E_P is given by

$$E_\mathrm{P} = E_\mathrm{kin} - eV_R - \phi_A = \frac{eV_\mathrm{P}}{R_2/R_1 - R_1/R_2}$$

where ϕ_A is the work function of the analyzer as shown in Fig. 3.15 and V_P is applied voltage between inner and outer hemispherical analyzer. One can sweep E_kin by sweeping E_P or V_R. Then, the energy resolution ΔE is determined by the slit width ω of hemispheres:

$$\Delta E = \frac{\omega E_\mathrm{P}}{R_1 + R_1}$$

In experiment, E_P is usually kept as a constant and V_R is swept so that ΔE is kept as a constant and independent of E_kin. Recently, a multi-channel detection system with a micro-channel plate (MCP) has been installed in the SCIENTA analyzers as a detector, allowing each channel to detect electrons with different pass energies.

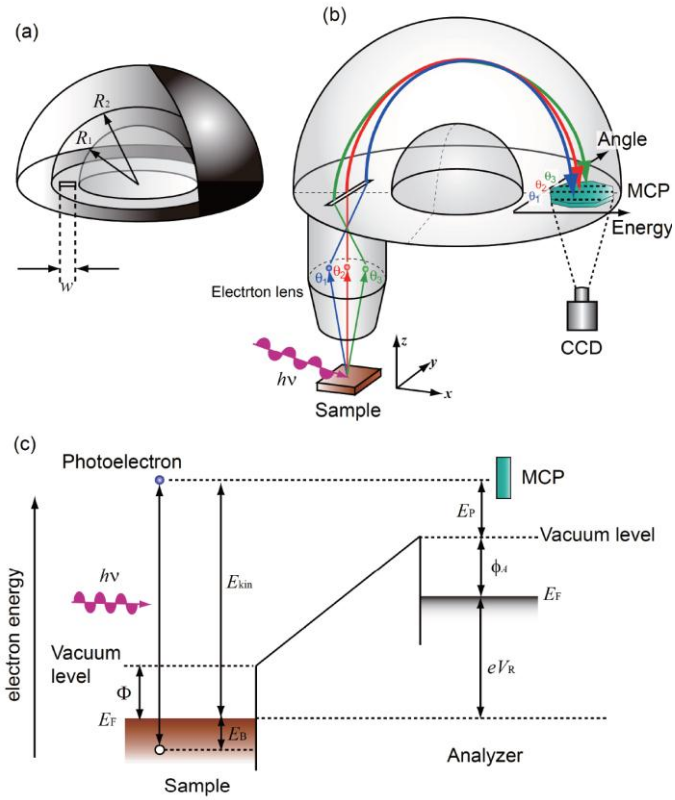

Figure 3.15 Schematic diagrams inside of the analyzer, and energy levels of the sample and analyzer. Reprinted from [41].

3.2.2.2 ARPES endstations

Here, the geometry of facilities where measurements in this thesis were performed, beamline 5-4 at Stanford Synchrotron Radiation laboratory (SSRL), beamline 28A at Photo Factory in High Energy Accelerator Research Organization (KEK) and laser-excited APRES at Institute of Solid State Physics (ISSP), University of Tokyo, is briefly introduced. Beamline 5-4 at SSRL can provide photons of the vacuum ultraviolet (VUV) range in an undulator beamline with a normal incidence monochromator (NIM), which has much higher throughput for the low energy photons as shown in Fig. 3.16(a). The beamline 28A at PF is an undulator beamline with a Spherical Grating Monochromator (SGM) as shown in Fig. 3.16(b). In the laser-APRES at ISSP, a Nd:YVO_4 laser system with a Fabry-Petot etalon and a non-linear optical crystal $KBe_2BO_3F_3$ is used to produce 6.994 eV photons [45]. A half wave ($\lambda/2$) plate and a quarter wave ($\lambda/4$) plate have been set up so as to move it between laser-spot positioning mirrors and serves the purpose of choosing the incident light polarization. This laser-excited ARPES can achieve a maximum energy resolution of 70 μeV and lowest cooling temperature of 1.5 K. Table 3.2 gives comparison among each APRES apparatus.

Table 3.2 Comparison among each APRES apparatus.

apparatus	beamline 28A @ PF	beamline 5-4 @ SSRL	laser-ARPES @ ISSP
photon energies	32 ~ 90 eV	7 ~ 40 eV	6.994 eV
temperature	9 ~ 300 K	5 ~ 300 K	1.5 ~ 300 K
analyzer	Scienta SES2002	Scienta R4000	Scienta HR8000
degrees of rotation freedom	θ, ϕ	θ, ϕ	θ
slit configuration (relative to the ground)	parallel	perpendicular	perpendicular
light polarization	P, circularly	P	P, S, left-circularly (l.c.), right-circularly (r.c.)
vacuum in the main chamber	$\leq 1 \times 10^{-10}$ Torr	$\leq 2 \times 10^{-11}$ Torr	$\leq 2 \times 10^{-11}$ Torr

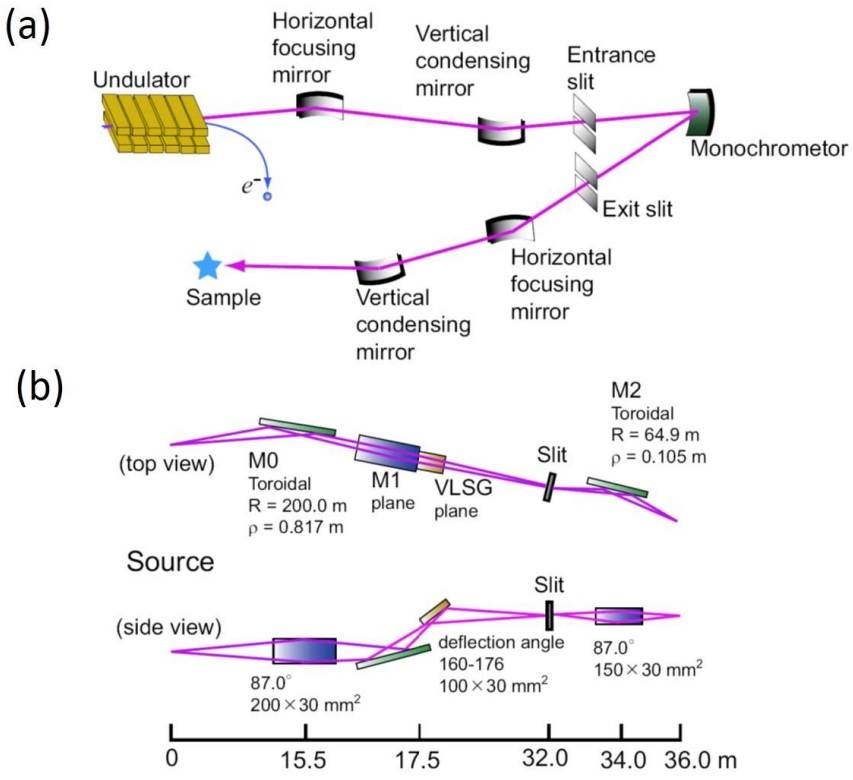

Figure 3.16 Schematic layout of beamline 5-4 at SSRL (a) and beamline 28A at PF (b). Reprinted from [42].

Chapter 4

Electronic transport properties of Cu- and Se-substituted $Fe_{1+x}Te$

4.1 Introduction

In the 11 family of FeSCs, FeSe with a simple α-PbO-type crystal structure was first found to have superconductivity around 8 K [46]. FeTe, realized upon complete substitution of Te for Se, exhibits an AFM ground state. The magnetic ordering can be suppressed by Se substitution and thus has been demonstrated proximity to a SC state in the phase diagram. In analogy to other families, FeTe is usually regarded as the "parent" compound of 11 family. FeTe exhibits a bicollinear magnetic ordering with different directions of the magnetic wave vector compared to $BaFe_2As_2$. In the 122 system, a major role of doping in the PT phase is known to change the FS by supplying charge carriers or exerting chemical pressure. It has also been revealed that the dominant role of doping in the AFO phase of the 122 materials is to introduce disorder to the system, resulting in the increase in the magnitude of the residual resistivity and controlling the suppression rate of the AFO ordering temperature [7]. Thus it is necessary to clarify the transport properties and the effect of atom substitutions in the 11 system. In this Chapter, the transport properties of $Fe_{1+x}Te_{1-y}Se_y$ with $y \leq 0.4$ and $Fe_{1+x-y}Cu_yTe$ with $y \leq 0.03$ are investigated.

4.2 "Parent" compound $Fe_{1+x}Te$

In the $Fe_{1+x}Te_{1-y}Se_y$ compounds, the interstitial sites of (Te,Se) layers usually allow the partial occupation of iron atoms [47], resulting in the existence of excess Fe in the chemical formula, which are thought to have a large effect on the physical properties. The schematic crystal structure of $Fe_{1+x}Te_{1-y}Se_y$ with excess Fe is illustrated in Fig. 4.1 [48]. The excess Fe is denoted by Fe(2). Experimentally, the content of excess Fe in the grown single crystals is sensitive to the actual growth condition (e.g., temperature gradient),

resulting in a variety of excess Fe content in the literature, although the molar ratio in the starting materials is the same.

It has been clarified through neutron diffraction experiments that the excess Fe content controls the crystal structure and magnetic ordering in the ground state [49]. The magneto-crystallographic phase diagram of $Fe_{1+x}Te$ is shown in Fig. 4.2. The ordering vector and crystal structure exhibit a crossover around a critical amount of excess Fe, $x \sim$

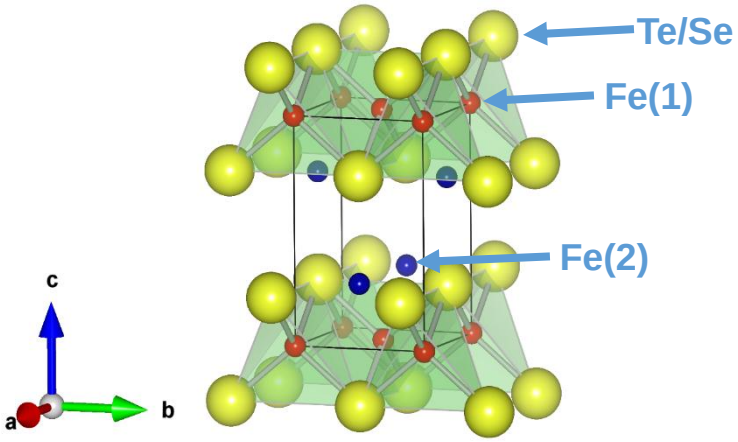

Figure 4.1 Crystal structure of $Fe_{1+x}Te_{1-y}Se_y$ with excess Fe. The iron at the interstitial sites of the (Te,Se) layers is the excess Fe, denoted by Fe(2). The figure was drawn using VESTAR [48].

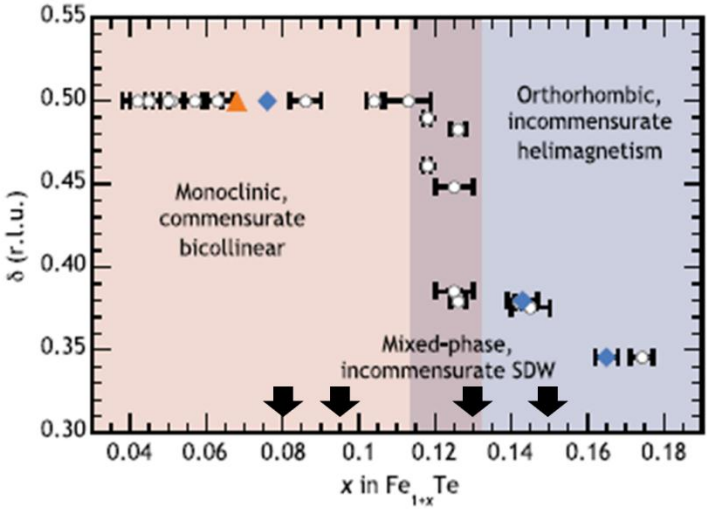

Figure 4.2 Magneto-crystallographic phase diagram of the ground state for $Fe_{1+x}Te$ constructed by plotting the δ of the propagation vector $k = (\delta\ 0\ \frac{1}{2})$ versus concentration of the interstitial iron. The black arrows indicate the concentrations of the interstitial iron of the single crystals studied in this chapter. Reprinted from [49].

0.12. The ground state at the region of low excess Fe concentration is monoclinic in structure with a commensurate AFM ordering, while it is orthorhombic at the region of high excess Fe concentration associated with an incommensurate AFM ordering. Around $x \sim 0.12$, there is an intermediate region where a structurally mixed-state exists.

$Fe_{1+x}Te$ single crystals with different excess Fe contents were grown to investigate their transport properties. The black arrows in Fig. 4.2 indicate the concentrations of the interstitial iron of the single crystals studied in this chapter. Figure 4.3 shows the temperature (T) dependence of the in-plane resistivity for the samples with different excess Fe contents. For $x \sim 0.08$, the T dependence is characterized by a sudden drop at 69 K, corresponding to an accompanying tetragonal-monoclinic structural transition and paramagnetic-AFM magnetic transition clarified through neutron diffraction [29] and X-ray diffraction measurements [50]. The T dependence of resistivity is divided into two distinct regions by the phase transition: in the paramagnetic-tetragonal phase, it is semiconductor-like whereas in the AFM-monoclinic phase resistivity decreases as T is lowered, showing the metallic behavior. In the perspective of spectroscopy measurements, ARPES spectra near E_F are characterized by a very broad feature in the PT phase [51], indicating an incoherent character of carriers and consequently causing semiconductor-like transport behavior in resistivity. This is also consistently reflected in the optical conductivity spectra [52], where no well-defined Drude component is observed. In the AFM phase, the ARPES spectra exhibit a "peak-dip-hump" line shape, where sharp coherent quasi-particle peaks emerge [53]. Correspondingly, in the optical conductivity spectra, a Drude component develops, responsible for the metallic behavior in the resistivity. The change in electric resistivity with temperature is probably related to the

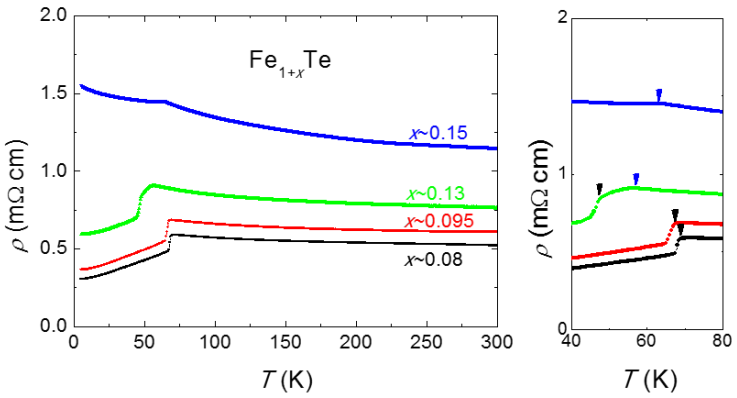

Figure 4.3 Temperature dependence of the in-plane resistivity of $Fe_{1+x}Te$ with different excess Fe content x. The right figure shows the enlarged plot around T_s.

emergence of new coherent carriers. Ref[53] also shows that the "peak-dip-hump" line shape of the ARPES spectra in the AFM phase is characteristic of polaron formations, reflecting the strong interaction among the charge, spin, and lattice. For a comparison, in the 122 parent compound, the band folding by the magnetic ordering vector of (π, 0) in the 1-Fe BZ induces strong Fermi surface reconstruction [54], resulting in a sharper drop in the resistivity as T decreases in the AFO phase.

For $x \lesssim 0.13$, the T dependence of the resistivity retains similarity, characterized by a drop at 50-70 K, which is the reflection of the magneto-structural transition. For $x \sim 0.08$, resistivity drops discontinuously at 69 K, indicating an almost first order transition. For $x \sim 0.13$, the T dependence of the in-plane resistivity shows a two-step feature in the transition. From the phase diagram in Fig. 4.2, one can see that this composition falls in the region with a structurally mixed state. Further X-ray diffraction measurements [50] have shown that in this region the tetragonal lattice first distorts into orthorhombic and then mostly becomes monoclinic with further cooling, which is reflected in the T dependence of resistivity as the observed two-step transition. If one evaluates T_s from the onset temperature where the resistivity begins to drop, as denoted by the arrows in Fig.

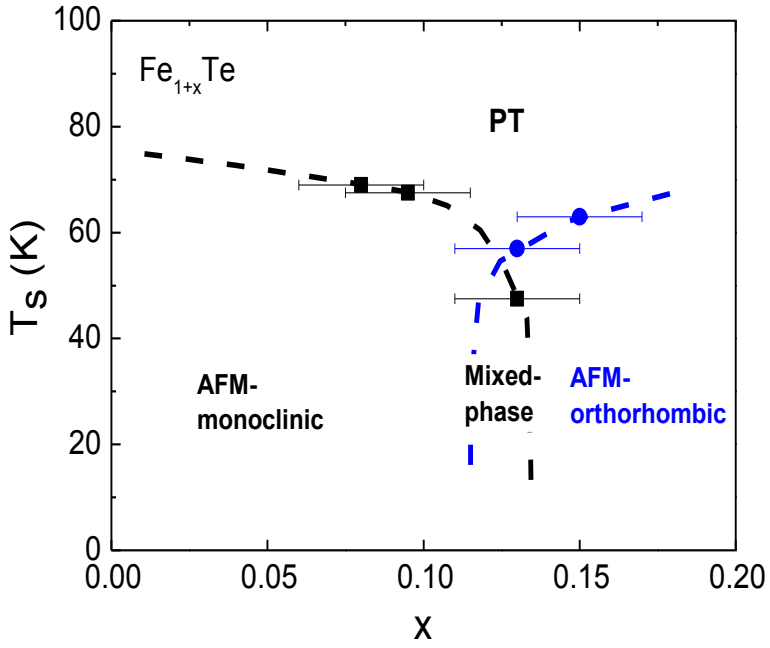

Figure 4.4 Transition temperature (T_s) plotted against the excess Fe content x. T_s is determined from the T dependence of resistivity and denoted by arrows in Fig. 4.3. $T_s \sim 75$ K was reported in the polycrystal materials [55], the constitution of which is perhaps close to the pure FeTe. The color bar schematically illustrates the evolution of the magneto-structural phase of the ground state.

4.3, T_s decreased with increasing excess Fe content. (Since the obtained FeTe single crystals always have a certain amount of excess Fe, the reported smallest amount of excess Fe, to our knowledge, is 0.02 with T_s ~ 72 K [53], while T_s ~ 75 K was also reported in the polycrystal material [55], the constitution of which is perhaps close to the pure FeTe.) For x ~ 0.15, there is a kink feature at T ~ 63 K in the T-dependent resistivity, corresponding to the tetragonal-orthorhombic transition in the phase diagram of Fig. 4.2. In this case, both the PT phase and AFM phase show semiconducting behaviors. It is very likely that the coherent Drude component observed in the ground state of $Fe_{1+x}Te$ with low x disappears [52] and all the carriers become incoherent. From the kink temperature, the evaluated transition temperature is 63 K, larger again than that of samples with x ~ 0.13. T_s evaluated from the resistivity results is plotted against x in Fig. 4.4. Given the neutron diffraction results, the schematic phase diagram is illustrated, which is consistent with the results from magnetic susceptibility measurements [50].

There is another important feature about the magnitude of the resistivity. One can see clearly that the magnitude of the resistivity monotonically increases with excess Fe content both in the PT phase and AFM phase, indicating a strong scattering character of excess Fe. In the well-studied 122 system, the impurities, e.g., dopants added into the parent compound, usually show strong elastic scattering in the AFO phase but weak scattering in the PT phase [6]. In contrast, excess Fe exhibits strong scattering effects in both phases. Perhaps related to this strong scattering effect in the PT phase, the deleterious effect of interstitial iron on superconductivity has been reported [56].

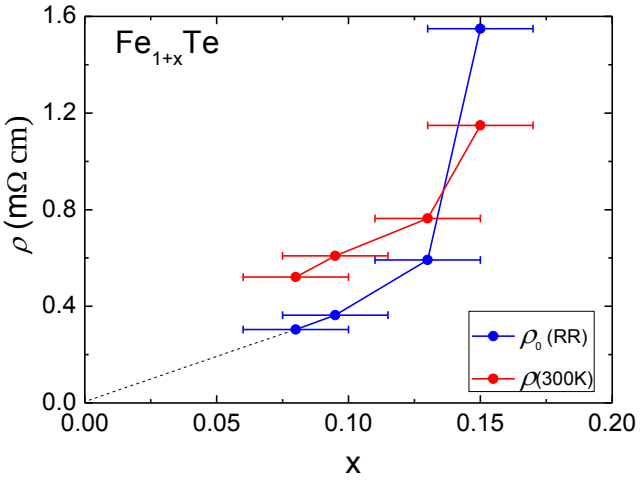

Figure 4.5 Magnitude of the resistivity at 5 K and 300 K, respectively, plotted against the excess Fe content x.

In Fig. 4.5, $\rho(5\mathrm{K})$ and $\rho(300\mathrm{K})$ is plotted against *x*. For $x \lesssim 0.13$, RR shows a good linear relationship with *x*, which can be extrapolated roughly to the origin. This implies that excess Fe can be taken as elastic impurity scattering centers towards the carriers in the AFM-monoclinic phase. When *x* exceeds the critical amount of excess Fe, a sharper increase in the magnitude of the electric resistivity with excess Fe content appears for $x \sim 0.15$. Given the semiconducting behavior even blow T_s, no coherent carrier presumably develops in the new magnetic ground state. It also appears that excess Fe changes its character with *x*. When *x* exceeds the critical value, excess Fe behaves as a relatively strong scattering center compared to that in the monoclinic phase. For $x \lesssim 0.13$, a weak decrease in T_s/T_N and a large increase in the magnitude of the resistivity with excess Fe content *x* suggest a very weak carrier-doping role, if any, of excess Fe. Thus excess Fe may have a neutral valence state. When the content exceeds the critical value, it may start to have some bonds with neighbor Te, triggering the structure of the ground state from monoclinic to orthorhombic. Consequently, the excess Fe may change its valence state, e.g., to positive, and thereby, scatters carriers more effectively.

4.3 Isovalent-substituted $Fe_{1+x}Te_{1-y}Se_y$

4.3.1 In-plane resistivity and magnetic susceptibility

Similar to the case of isovalent substitution in iron pnictides, Se substitution for Te in FeTe suppresses the magnetic ordering and induces superconductivity. We have grown single crystals of $FeTe_{1-y}Se_y$ with $y \leq 0.4$. As shown previously, a large amount of excess Fe usually exist in the grown single crystals. Generally, there is a trend that, with Se substitution, excess Fe content becomes less. Table 3.1 shows chemical compositions of the grown single crystals. For $y \leq 0.1$, there is almost no change in the excess Fe content, a small decrease for $y = 0.2$, and no excess Fe for $y = 0.4$.

The *T* dependence of the in-plane resistivity is shown in Fig. 4.6 (a). T_s is suppressed as denoted by arrows in the figure. For $y = 0.08$, the *T* dependence of the resistivity at T_s evolves into a kink feature, as in the case of $Fe_{1+x}Te$ with $x \sim 0.15$, while for $y = 0.1$, although the kink structure seems to more or less remain, the transition temperature cannot be unambiguously evaluated from the resistivity curve. However, a magnetic transition can still be seen for $y = 0.1$ from the magnetization measurement as shown in Fig. 4.7. Superconducting transition also appears for $y = 0.1$, as shown in Fig. 4.6(b). But the resistivity does not reach zero until 5 K, which is also the case for $y = 0.2$. Magnetization measurements at low field could not confirm the Meissner diamagnetism,

indicating the observed superconducting transition is filamentary. Single crystals with $y = 0.41$ show zero resistivity below 14 K. (As-grown samples show a small SC shielding fraction in the magnetization measurement whereas it is largely improved after annealing.) The critical temperatures evaluated from the resistivity measurement and the magnetization measurement are summarized in Fig. 4.8, where the superconductivity region is filamentary except $y = 0.41$. Note that moderate annealing would induce bulk superconductivity. The effect of annealing will be discussed below. The obtained phase diagram here is consistent with other studies on as-grown $Fe_{1+x}Te_{1-y}Se_y$ crystals [57, 58].

As can be seen from the resistivity normalized to $\rho(300K)$ in Fig. 4.6(c), there is no change in the T dependence in the PT phase for $y \leq 0.2$ while a weakly metallic behavior appears for $y = 0.41$. This can be naturally expected since the end material FeSe shows a good metallic character, as reported both in single crystals and polycrystals. For $y \leq 0.1$, it is shown that the metallic T dependence in the AFM phase is suppressed,

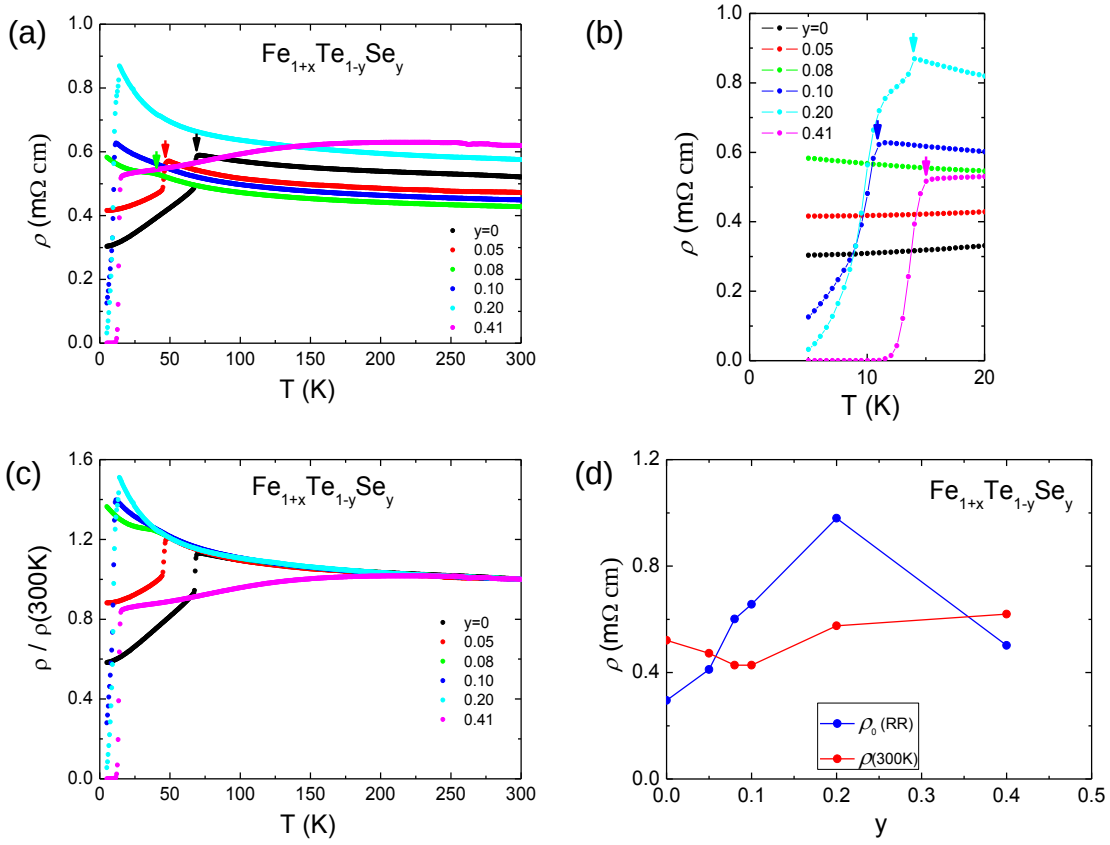

Figure 4.6 (a-c) Temperature dependence of the in-plane resistivity of $Fe_{1+x}Te_{1-y}Se_y$. (d) The magnitude of the resistivity at 5 K and 300 K, respectively, plotted against the substituted Se content y. The content of excess Fe x is shown in Table 3.1.

evolving into the semiconducting behavior, reflecting the suppression of the metallic AFM state. Figure 4.6(d) illustrates $\rho(5\mathrm{K})$ and $\rho(300\mathrm{K})$. For $y \leq 0.1$ where the AFM ground phase survives, $\rho(5\mathrm{K})$ increases with y, which can be ascribed to the suppression of the metallic AFM state and the elastic scattering effect from substituted Se atoms, indicating the resemblance in $Fe_{1+x}Te_{1-y}Se_y$ to that in isovalent P-doped 122 materials [7].

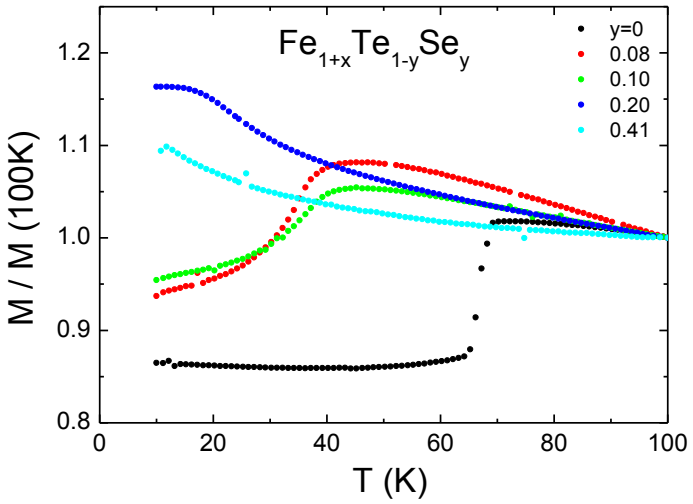

Figure 4.7 Temperature dependence of the magnetization of $Fe_{1+x}Te_{1-y}Se_y$.

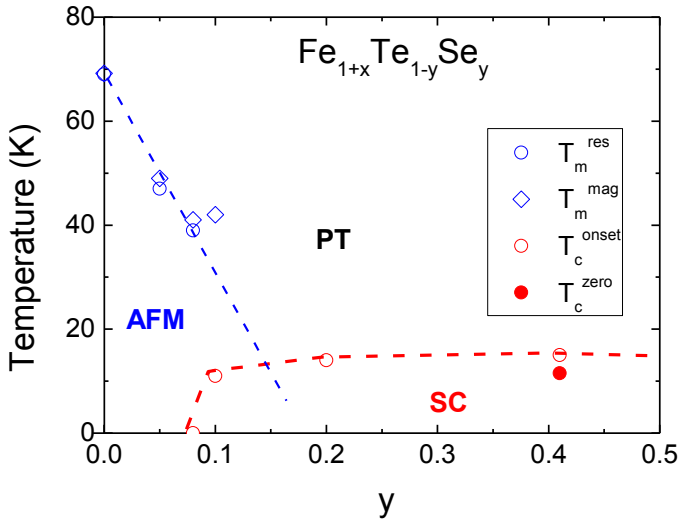

Figure 4.8 Phase diagram of $Fe_{1+x}Te_{1-y}Se_y$ ($y \leq 0.4$).

Furthermore, the question of what role Se substitution plays in inducing superconductivity needs to be answered. Studies on this system show that neither substitution at the Fe site nor applying pressure to FeTe can induce superconductivity [20], unlike in other families of FeSCs. It is reported [59] that, however, FeTe films, in which the misfit between the films and the substrates induce a tensile strain, exhibit superconductivity. The effect of isovalent Se substitution to induce superconductivity is also likely to be application of chemical pressure effect. The limited variety to induce superconductivity in 11 may be related to the large deviation from the structural optimization of chalcogen height and/or bond angle.

4.3.2 Annealing effect on superconductivity

It is found that annealing can remarkably improve the transport properties of $BaFe_2As_2$, particularly, reflected in the large decrease of the magnitude of RR [37]. Vacuum annealing on $Fe_{1+x}Te$ crystals was also tried but no improvement was observed in resistivity. On the contrary, the *T* dependence becomes insulating in the ground state [39], close to that of crystals with high excess Fe content. This is presumably because vacuum annealing leads Te to being drawn out of crystals.

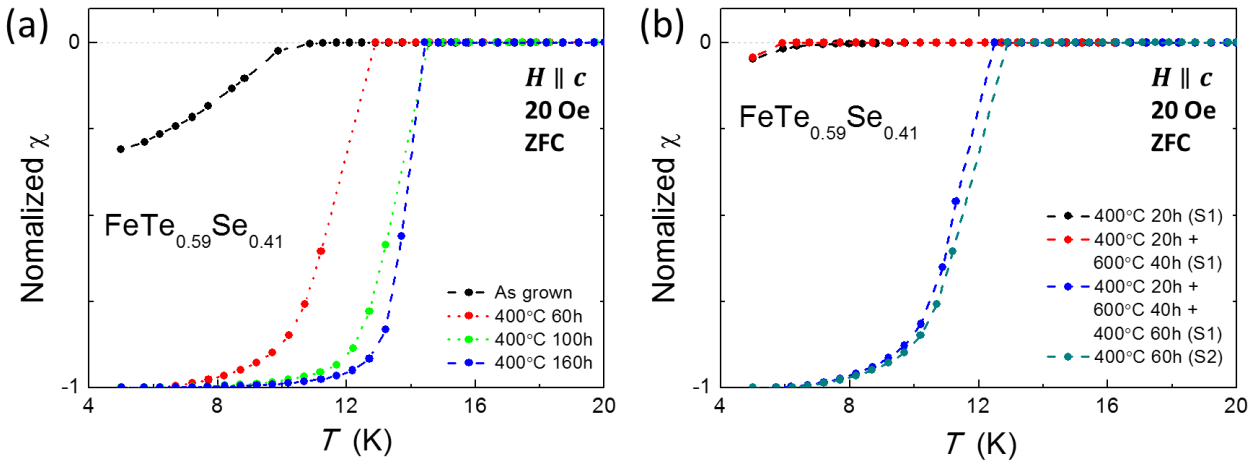

Figure 4.9 *T* dependence of normalized χ for $FeTe_{0.59}Se_{0.41}$ single crystals annealed in a vacuum under different conditions. In order to get rid of the effect of demagnetization factor, the magnetic susceptibility is normalized to the magnitude of the same piece at 5 K after having optimally annealed. In Fig. (b), the evolution of the magnetization with a series of vacuum annealing for the same sample (S1) is shown, while the results for the sample (S2) are illustrated for comparison.

We have also focused on the annealing effect on superconductivity in $FeTe_{0.59}Se_{0.41}$. The single crystals are sealed into a quartz tube after pumped below 10 Pa. In order to get rid of the effect of demagnetization factor, the magnetic susceptibility is normalized to the magnitude of the same piece at 5 K after having optimally annealed. In Fig. 4.9(a), as-grown samples show diamagnetic signals but a low shielding fraction and low T_c. T_c increases through annealing at 400°and diamagnetic signals become saturate at low temperature. Annealing for longer time is favorable for better superconducting transition. After having annealed for 160h, the single crystals show T_c ~ 14 K with the transition width of ~ 1.5 K, comparable to that reported in the literature. It is reported [60] that high inhomogeneity exists in $Fe_{1+x}Te_{1-y}Se_y$, a possible reason for hindering superconductivity. Annealing reduces crystal inhomogeneity effectively, thus resulting in the improvement of superconductivity.

Figure 4.9(b) shows the effect of annealing at 600°. No improvement was observed after annealing at 600° for 40h. One may consider that 600° was so high that Se/Te atoms are drawn out of the crystals. However, the improvement in superconductivity after annealing at 400° on the same piece rules out this possibility. This finding shows that 400° is a good annealing temperature, further confirming that annealing at a moderate temperature can reduce disorders/inhomogeneity which degrades superconductivity. However, vacuum annealing was found to be ineffective in inducing superconductivity in both $FeTe_{0.8}Se_{0.2}$ and $FeTe_{0.9}Se_{0.1}$ whereas O_2 annealing is effective.

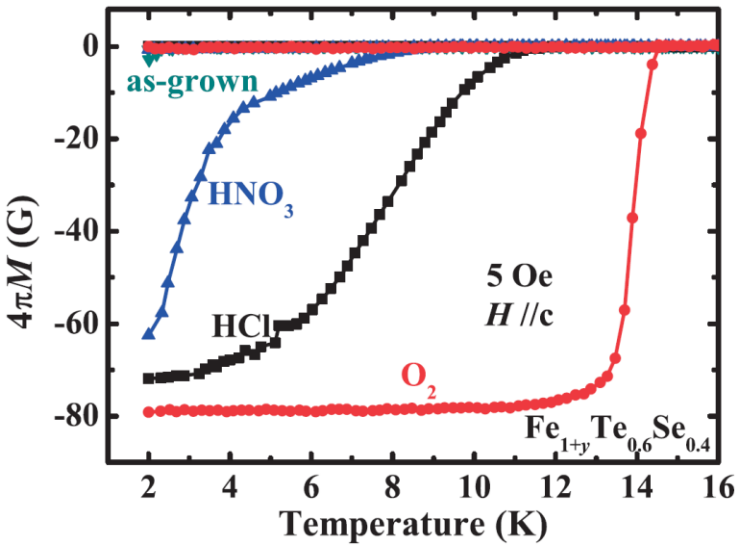

Figure 4.10 Temperature dependence of the magnetization for the post-treated $Fe_{1+y}Te_{0.6}Se_{0.4}$ samples. Reprinted from [57].

It has been also reported that either annealing in O_2 for more than one day or putting samples in acid can induce bulk superconductivity in $Fe_{1+x}Te_{1-y}Se_y$. Among them O_2 annealing was the most effective, as shown in Fig. 4.10 [57]. The mechanism of how O_2 annealing works to induce superconductivity is still under debate. It was argued that O_2 annealing results in the deintercalation of excess Fe [57], which has a deleterious effect on superconductivity. The composition analyses show no change in the Fe content on the annealed samples. Thus O_2 annealing may oxidize the excess Fe and thereby equivalently reduce the actual excess Fe content. It should be noted that the molar ratio of oxygen sealed into quartz tubes to the total amount of Fe was controlled to be only ~ 1.5%, whereas it has such a large effect.

4.4 Cu-substituted $Fe_{1+x}Te$

In order to establish the comparison with transition-metal doped iron pnictides, the Cu-substituted $Fe_{1+x}Te$ single crystals were grown and investigated. The composition was analyzed by EDAX, resulting in x around 0.08 and y = 0, 0.01, and 0.03. Figure 4.11 shows the T dependence of the in-plane resistivity of $Fe_{1+x-y}Cu_yTe$.

Upon Cu substitution, T_s is reduced systematically from T_s = 69 K for Cu-free samples to T_s = 44 K for 3% Cu-substituted samples. The phase diagram is summarized in Fig.

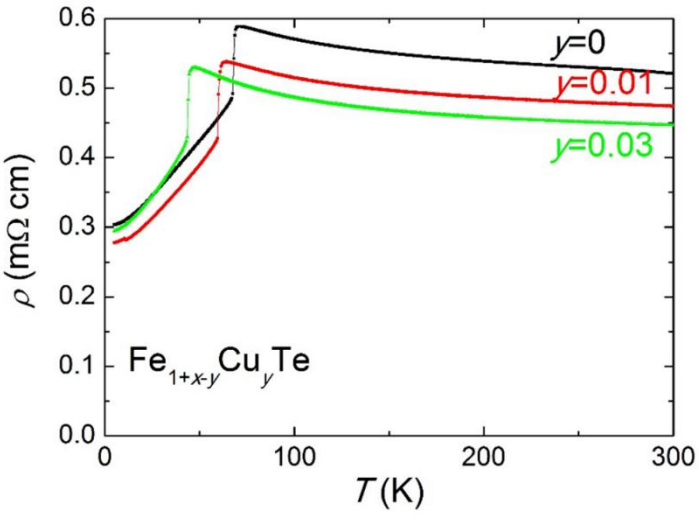

Figure 4.11 Temperature dependence of the in-plane resistivity of $Fe_{1+x-y}Cu_yTe$ with x ~ 0.08 and y ~ 0, 0.01, and 0.03, respectively.

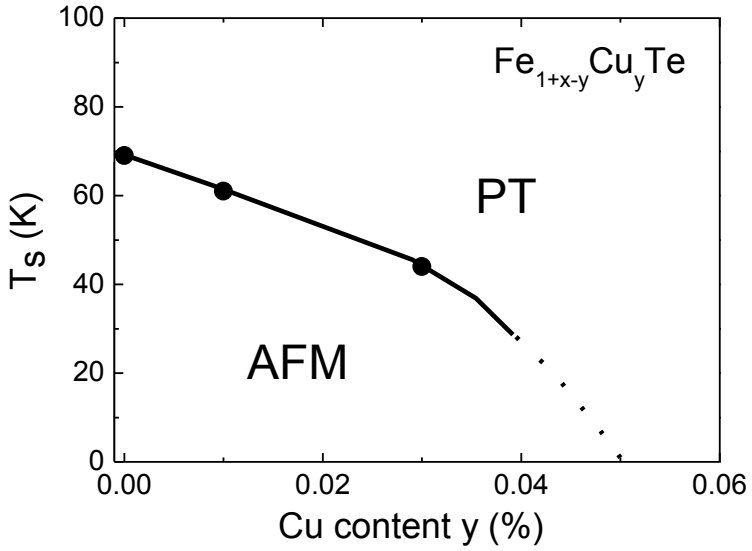

Figure 4.12 Phase diagram of $Fe_{1+x-y}Cu_yTe$.

4.12. This observation suggests that Cu atoms effectively substitute for in-plane Fe atoms, causing a reduction in ordering temperature probably due to magnetic frustration of a Cu ion with smaller magnetic moment [61].

Contrary to the strong scattering effect of excess Fe on the absolute value of resistivity, upon Cu substitution resistivity shows small change in the metallic region below T_s while in the PT phase it becomes slightly smaller. It has been revealed that doped Cu atoms in 122 have a deep impurity potential, acting to strongly increase the elastic scattering rate in the AFO phase [8]. In contrast, the small change of RR in $Fe_{1+x-y}Cu_yTe$ suggests the distinct effect on transport properties upon Cu substitution from that in the 122 system. In the 11 materials, the contribution to residual resistivity purely from elastic scattering of Cu atoms could be masked by the incoherent component in the AFM state which has a large contribution to conductivity. Details shall be discussed in Chapter 5.

Chapter 5

In-plane resistivity anisotropy in the magneto-structural phase of iron telluride

5.1 Introduction

As described in Chapter 2, using detwinned $Ba(Fe_{1-x}Co_x)_2As_2$ single crystals, anisotropic gap opening in optical spectroscopy [11], symmetry-breaking orbital anisotropy by ARPES [13], and remarkable in-plane resistivity anisotropy via transport measurement [5, 6, 8, 9] have been revealed to be related to the unique fourfold symmetry-broken AFO ground state. In the resistivity measurement, the resistivity along *b* axis (shorter axis with ferromagnetic spin alignment) is larger than that along *a* axis (longer axis with AFM spin alignment), which is somewhat counterintuitive. One more important feature is the monotonic increase of the resistivity anisotropy initially when doped with transition metal atoms. The origin of the resistivity anisotropy in the AFO phase has been discussed in terms of either anisotropic spin exchange interactions [62] or orbital ordering [15]. The relatively small in-plane resistivity anisotropy of the parent compound has been ascribed to the presence of an isotropic, high mobility pocket of the reconstructed Femi surface associated with a Dirac cone [8]. On the other hand, an impurity-induced-anisotropy scenario has also been proposed [6, 10, 16] to explain the results. That is, the in-plane resistivity anisotropy arises from the elastic impurity scattering by dopants/impurities which polarize their environment with inherent electronic anisotropy in the AFO phase and thereby produce an anisotropic scattering cross section.

The "parent" compound of iron chalcogenide superconductors, $Fe_{1+x}Te$, also has an AFM ground state with broken fourfold rotational symmetry, but shows bicollinear magnetic order with different direction of the magnetic wave vector (by 45°) from that of $BaFe_2As_2$ (Fig. 2.4). Here, it is necessary to indicate again the definition of *a*- and *b*-axes in the AFM state. For both 122 and 11 materials, the *a*-axis is defined as the longer axis with AFM spin alignment while the *b*-axis is the shorter axis with ferromagnetic spin alignment, as illustrated in Fig. 2.4. Since the directions of the AFM ordering wavevector

in 122 and 11 materials is 45° different, the defined *a*- and *b*-axes for 11 and 122 materials are 45° rotated from each other. Thus extending the resistivity anisotropy measurement to the 11 system would shed light on further understanding the resistivity anisotropy observed in iron pnictides. In this Chapter, the results on the in-plane resistivity anisotropy in 11 compounds are shown and discussed.

5.2 "Parent" compound $Fe_{1+x}Te$

As explained in the chapter 4, excess Fe usually exists in the 11 system by partially occupying the interstitial site of chalcogen layers (Fig. 4.1). Both in the PT phase and AFM phase, excess Fe demonstrates its strong scattering character. The in-plane resistivity anisotropy of $Fe_{1+x}Te$ single crystals with three different excess Fe contents, which have the same ground state with the commensurate AFM ordering and the monoclinic crystal structure, were investigated. The results are shown in Fig. 5.1. No anisotropy was observed well above T_s, similar to the case of $SrFe_2As_2$ and $CaFe_2As_2$, the phase transition of which is also essentially of first order. A clear anisotropy appears when the temperature is decreased below T_s. The resistivity along *a*-axis (ρ_a) becomes larger than that along *b*-axis (ρ_b) in the AFM phase, i.e., $\rho_a > \rho_b$, which is consistent with the results by Jiang *et al*. [63]. Note that this is opposite to the resistivity anisotropy observed in the iron pnictide. For example, ρ_b becomes larger than ρ_a for the detwinned $BaFe_2As_2$ crystals, as shown in Fig. 5.2 [37]. In the AFM phase of $Fe_{1+x}Te$, ρ_a and ρ_b show similar temperature dependence, more clearly seen in the weak T dependence of the difference of ρ_a and ρ_b ($\Delta\rho = |\rho_a - \rho_b|$), as shown in Fig. 5.3(a). This means that the resistivity anisotropy mostly originates from the anisotropy of residual resistivity (RR) component. Furthermore, the magnitude of the resistivity anisotropy increases with amount of excess Fe, as summarized in Fig. 5.3(b), while excess Fe atoms induce a weak decrease in AFM ordering temperature. This implies that the absolute value of resistivity anisotropy has a close relationship with the existing excess Fe atoms in $Fe_{1+x}Te$. This reminds us of the annealing effect on the in-plane resistivity anisotropy in $BaFe_2As_2$ (Fig. 5.2). Absolute values of the anisotropy decrease, after single crystal quality is improved by annealing [37], evidenced by the remarkable reduction in RR and an increase in the transition temperature. This implies the sensitivity of the resistivity anisotropy to disorder, in analogy with the excess Fe impurity atoms in $Fe_{1+x}Te$.

From the evolution of the magnitude of the resistivity anisotropy with x in Fig. 5.3, one can see a more effective effect of excess Fe on $\Delta\rho$ for the samples with $x \sim 0.13$ than those with lower excess Fe content, if $\Delta\rho$ is normalized to x. We have discussed in Chapter 4

that the excess Fe controls the magneto-structural phase in the ground state, and changes its scattering character with *x*, which might be related to the change in its valence state. For $x \sim 0.13$, which is located at the intermediate region of the phase diagram, it is reasonable to consider the more effective role of excess Fe in accounting for the resistivity anisotropy.

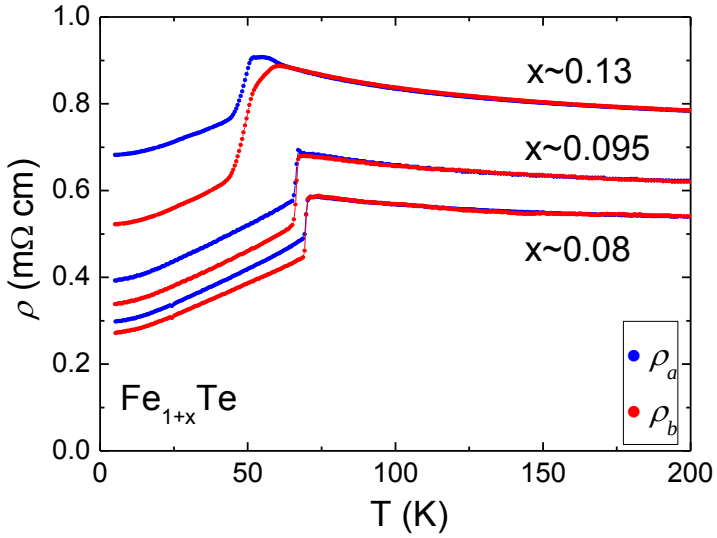

Figure 5.1 Temperature dependence of the in-plane resistivity measured on detwinned $Fe_{1+x}Te$ crystals with different excess Fe content *x*.

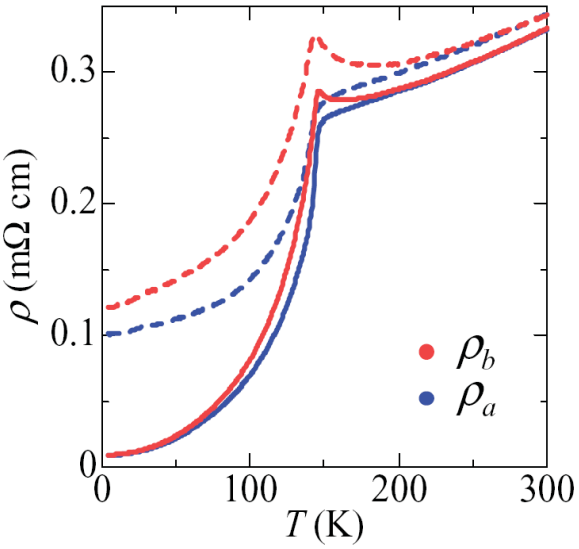

Figure 5.2 Temperature dependence of the in-plane resistivity measured on detwinned $BaFe_2As_2$ crystals. The dashed line and the solid line correspond to as-grown and annealed crystals, respectively. Reprinted from [37].

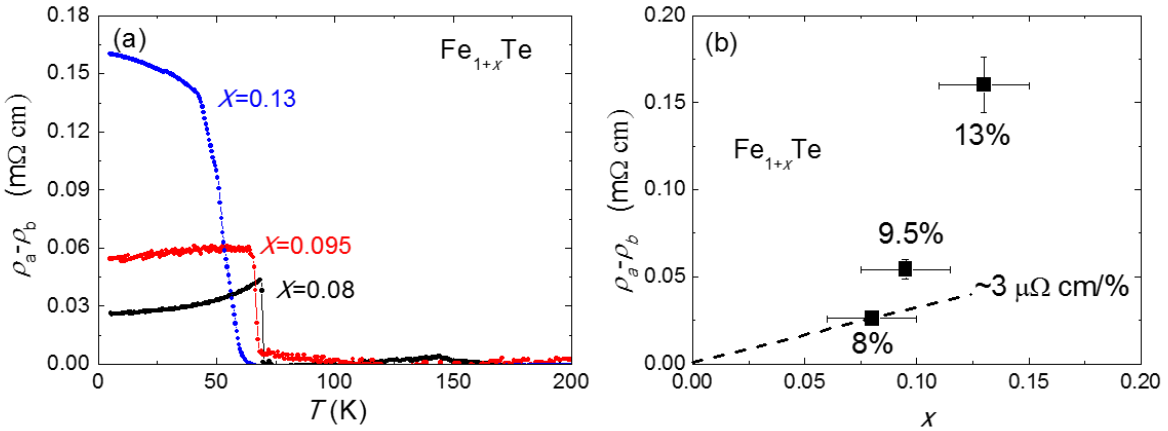

Figure 5.3 (a) Temperature dependence of the difference of the in-plane resistivity (ρ_a-ρ_b). (b) (ρ_a-ρ_b) at 5 K for $Fe_{1+x}Te$ plotted against the excess Fe content x.

5.3 Se-substituted $Fe_{1+x}Te$

With Se isovalently substituting for Te, the $Fe_{1+x}Te_{1-y}Se_y$ single crystals with $y \leq 0.08$ were detwinned to investigate the in-plane resistivity anisotropy. The results are shown in Fig. 5.4-5.5. Anisotropy with $\rho_a > \rho_b$, the same as that in $Fe_{1+x}Te$ while opposite to that in iron pnictides, appears in the AFM phase of $Fe_{1+x}Te_{1-y}Se_y$, persisting up to $y = 0.08$. For

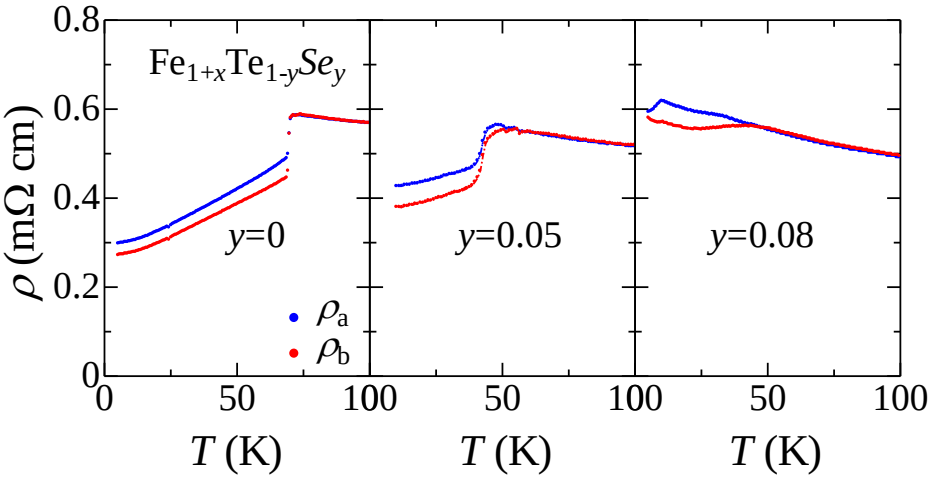

Figure 5.4 Temperature dependence of the in-plane resistivity for detwinned $Fe_{1+x}Te_{1-y}Se_y$ crystals. The content of excess Fe x is shown in Table 3.1.

y = 0.08, the resistivity anisotropy suddenly becomes small below 10 K, which results from the appearance of the filamentary superconductivity. Upon Se substitution, it appears that $\Delta\rho$ initially becomes larger and has small change with further substitution ($y \leq 0.08$). If the substituted Se atoms are also responsible for the induction of resistivity anisotropy, the effect becomes weaker for y = 0.08 than that for y = 0.05. This can be understood given that the metallic AFM ordering was strongly weakened for y = 0.08, evidenced by the insulating behavior of the in-plane resistivity below T_s. This is also the case in $Ba(Fe_{1-x}Co_x)_2As_2$, where resistivity anisotropy becomes weak in the highly-doped region.

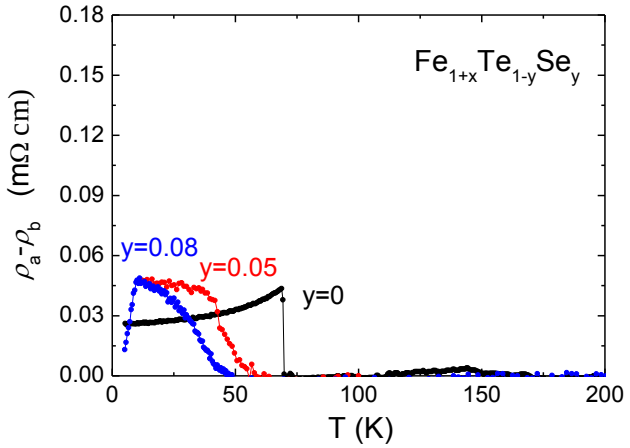

Figure 5.5 Temperature dependence of the difference of the in-plane resistivity (ρ_a-ρ_b) for $Fe_{1+x}Te_{1-y}Se_y$ crystals.

5.4 Cu-substituted $Fe_{1+x}Te$

The results on ρ_a and ρ_b measured on detwinned Cu-substituted $Fe_{1+x}Te$ crystals are shown in Fig. 5.6. They have the similar T dependence to that in the Cu-free samples (Fig. 5.7). The resistivity anisotropy appearing in the AFM phase is also the same as that in $Fe_{1+x}Te$, $Fe_{1+x}Te_{1-y}Se_y$. The magnitude of the resistivity anisotropy appears to increase monotonically for the samples with more Cu substituting for Fe.

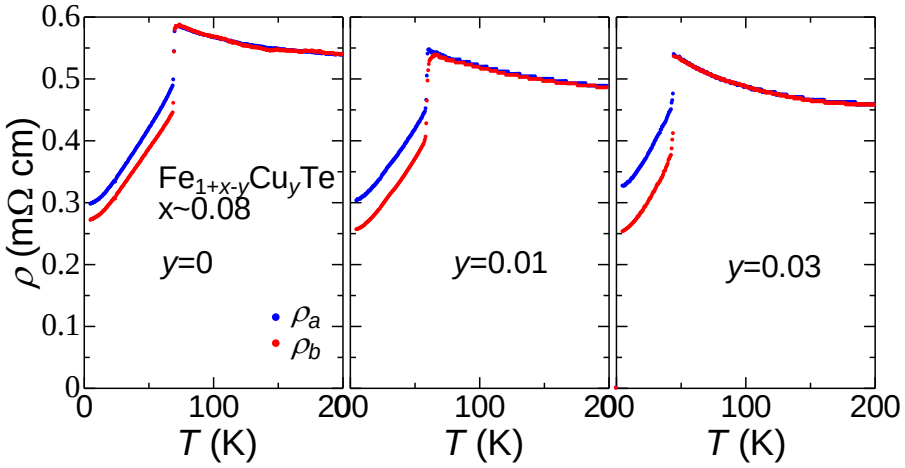

Figure 5.6 Temperature dependence of the in-plane resistivity for detwinned $Fe_{1+x-y}Cu_yTe$ crystals with x~0.08 and y~0, 0.01, and 0.03, respectively.

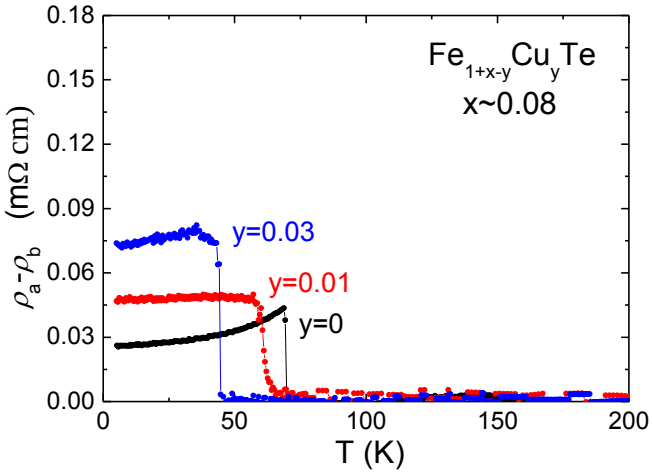

Figure 5.7 Temperature dependence of the difference of the in-plane resistivity (ρ_a-ρ_b) for $Fe_{1+x-y}Cu_yTe$.

5.5 Discussions

Firstly, we recall the results for the 122 materials. It is known that effective annealing can lead to a remarkable decrease of the resistivity anisotropy without obvious change in the electronic structure and the resistivity anisotropy initially increases with doping (Fig. 5.8). This is in striking contrast to that either structural orthorhombicity [22] or electronic anisotropy [13] revealed by optical spectroscopy and ARPES is suppressed by doping. These experimental results have been ascribed to the presence of an isotropic Dirac pocket with highly mobile carriers, which might mask the resistivity anisotropy contributed by other anisotropic pockets [8]. If this scenario is correct, a remarkable anisotropy in 4% Co-doped samples ($\rho_b/\rho_a \sim 2$) would be contributed by the anisotropic pockets. However, analyses on the magneto-transport measurements found that the highly mobile carriers corresponding to the Dirac-cone-like pocket equally contribute to the conductivity to other pockets [37]. Therefore, such a remarkable anisotropy ($\rho_b/\rho_a \sim 2$ in 4% Co-doped samples) seems unlikely to be almost completely masked by the Dirac pocket in the parent compounds. Further studies using annealed samples demonstrate that resistivity anisotropy increases linearly with the Co composition in the "pure" AFO phase [6] (Fig. 5.8). Analysis of a Drude component in the optical spectroscopy suggests that the anisotropy in the resistivity originates from the anisotropic carrier scattering rate rather

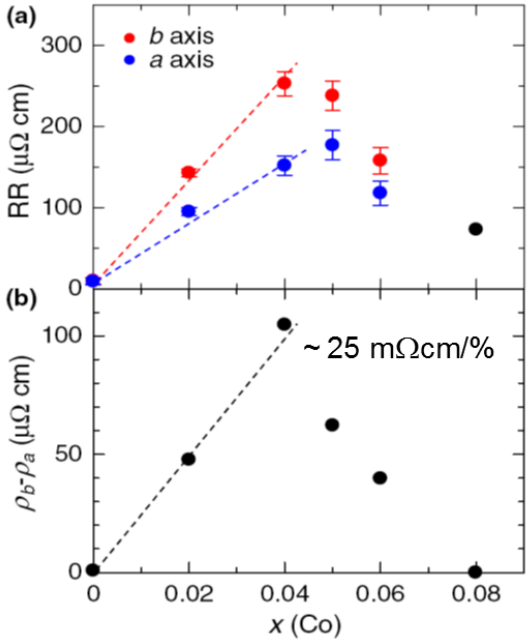

Figure 5.8 RR and (ρ_b-ρ_a) at low temperature plotted against the Co content for annealed $Ba(Fe_{1-x}Co_x)_2As_2$ single crystals. Reprinted from [6].

than anisotropic effective mass [10]. These results help us to establish the scenario that the doped Co atoms work as anisotropic scattering centers. The scanning-tunneling-spectroscopy (STS) measurement of $Ca(Fe_{1-x}Co_x)_2As_2$ provided a direct observation of the formation of anisotropic dopant-induced impurity states [16]. Each impurity center is ~ 8 Fe-Fe unit cells in length, showing the shape of *a*-axis aligned electronic dimmers, as illustrated in Fig. 5.9 (a). It is found that these impurity states scatter quasiparticles in a highly anisotropic manner with the maximum scattering rate concentrated along the *b* axis.

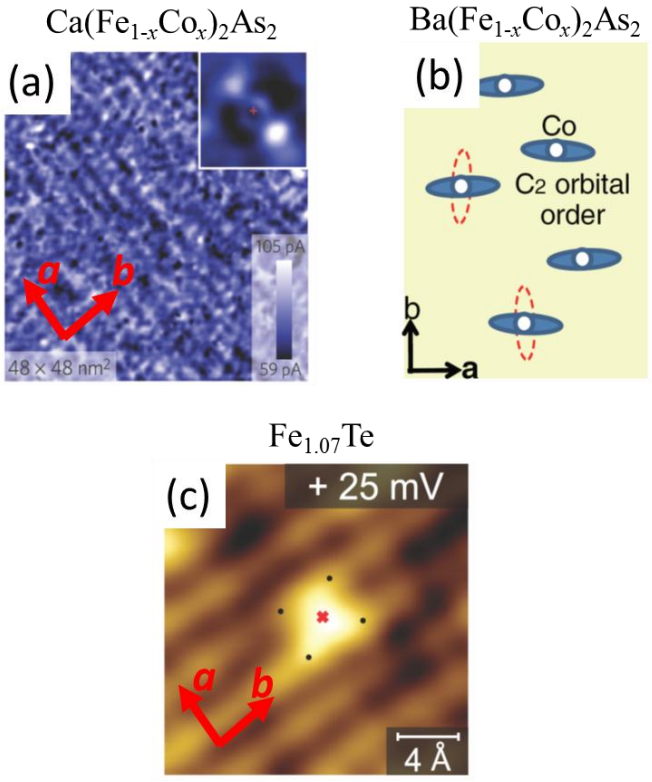

Figure 5.9 (a) The current map taken at -37mV on $Ca(Fe_{1-x}Co_x)_2As_2$, showing a "dimer"-shaped electronic impurity state around a Co-dopant atom. Reprinted from [16]. (b) Alignment of the impurity-induced C2 orders calculated for $Ba(Fe_{1-x}Co_x)_2As_2$. Reprinted from [65]. (c) STM images taken at bias voltage V_B=+25mV on $Fe_{1.07}Te$, showing a triangular pattern around the excess Fe atom. Reprinted from [64].

From the *T* dependence of $\Delta\rho$ for different substitutions, one can see that the *T* dependent component in $Fe_{1.08}Te$ is weak and reaches a maximum at T_s. For other cases, either with larger amount of excess Fe or Cu-, Se-substitution, $\Delta\rho$ remains almost constant. This means that the resistivity anisotropy observed is mostly determined by that at 0 K limit, i.g., the anisotropy in RR component.

For each case, the magnitude of the resistivity anisotropy increases while the ordering temperature is suppressed, from which the intrinsic anisotropy of the electronic states in the ordered phase is expected to weaken. Thus, the anisotropy in RR component seems unlikely to arise directly from the intrinsic electronic anisotropy, e.g., anisotropic effective mass, or the anisotropic spin structure in the ground state. In other words, these results provide evidence of an extrinsic origin of the resistivity anisotropy in 11 materials, that is to say, the resistivity anisotropy is closely correlated with the impurity effect, similar to that in 122 materials. For $Fe_{1+x}Te$, it is excess Fe that induces the resistivity anisotropy. As a result, the magnitude of the resistivity anisotropy increases with the amount of excess Fe. Very recent STS studies around an excess Fe atom in $Fe_{1+x}Te$ found that an anisotropic electronic structure with the shape of isosceles triangular forms around it, as shown in Fig. 5.9(c) [64], in agreement with our resistivity measurements. Note that the observed anisotropy in the local electronic state around excess Fe is not so large as that in Co-doped 122 materials.

For Cu- and Se-substituted $Fe_{1+x}Te$, it cannot be completely ruled out that the excess Fe content increases with Se/Cu doping. Although the EDAX analysis indicates no significant change of x, it is subject to some uncertainty (± 0.02). Given a large increase in the magnitude of resistivity anisotropy $\Delta\rho$ with a small increase of excess Fe content, as shown in Fig. 5.3(b), it might be possible that the observed change is due to a tiny change in x within the EDAX error bars. However, in view of the systematic decrease with Cu-substitution and insensitiveness to the Se-substitution in the magnitude of the PT phase resistivity which increases with excess Fe content, it is likely that the change of the excess Fe content is small enough not to significantly affect the result of the resistivity anisotropy in the Cu- and Se-substituted 11 crystals. If these atom substitutions are really responsible for the observed increase of resistivity anisotropy, the present results suggest that the Cu and Se atoms also work as anisotropic scattering centers. Note that the sign of the resistivity anisotropy in iron telluride is always opposite to that in iron pnictide irrespective of dopant site. This implies that around each excess Fe atom and substituted Cu/Se atom, exotic anisotropic impurity states might be formed by anisotropically polarizing its electronic environment as schematically illustrated in Fig. 5.10(c), and the polarization cloud is oriented along the crystallographic b axis (in the case of 122 its orientation is along a axis). From the present results and discussions, the impurity scenario may be the common phenomenological origin to explain the resistivity anisotropy in both 11 and 122 compounds.

Moreover, even if there might be some contributions from a slight increase of the excess Fe content to the observed increase in $\Delta\rho$, a stronger carrier scattering from Cu

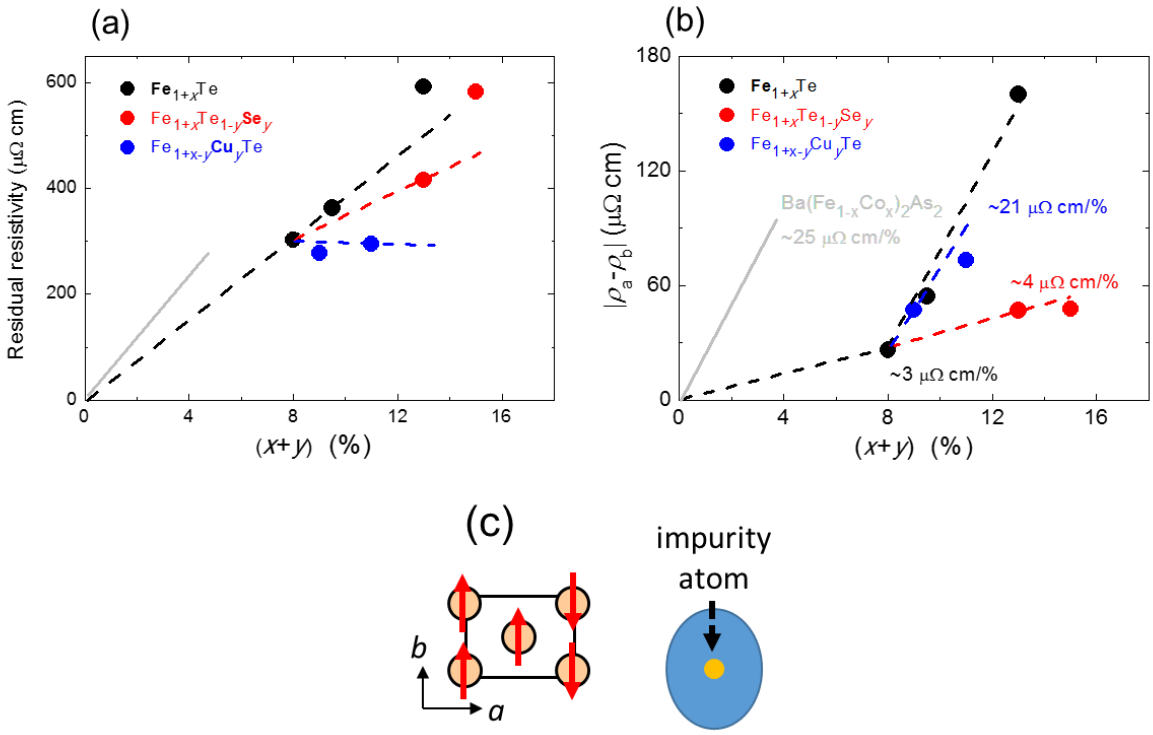

Figure 5.10 (a) Residual resistivity plotted against the total impurity content (x+y) for $Fe_{1+x}Te$, $Fe_{1+x}Te_{1-y}Se_y$ and $Fe_{1+x-y}Cu_yTe$, respectively. (b) Difference of the in-plane resistivity (ρ_a-ρ_b) at low temperature (5 K for $Fe_{1+x}Te$ and $Fe_{1+x-y}Cu_yTe$, 10 K for $Fe_{1+x}Te_{1-y}Se_y$) plotted against the total impurity content (x+y) for $Fe_{1+x}Te$, $Fe_{1+x}Te_{1-y}Se_y$ and $Fe_{1+x-y}Cu_yTe$, respectively. The grey solid lines illustrate the dependence of substituted Co content for $Ba(Fe_{1-x}Co_x)_2As_2$, which is reproduced from [6]. (c) Schematic figure of the anisotropic electronic state around an impurity atom in iron telluride.

impurity atoms than that from Se atoms is evident in the plot of Fig. 5.10(b). As will be shown in Chapter 6, the isovalent (Ru, P) substitution in the 122 materials has a much weaker effect on $\Delta\rho$ than heterovalent (transition-metal) substitution.

One of the most striking aspects of the results described above is the sign of the resistivity anisotropy. In 122 compounds, ρ_b is larger than ρ_a while it is opposite in 11. Our results suggested that the observed magnitude of the resistivity anisotropy in the 11 materials is also related to the formation of an anisotropic impurity state, which is similar to that in 122 compounds. Under the impurity-induced-anisotropy scenario, the unique AFO ground state in 122 or monoclinic-AFM ground state in 11 with intrinsic electronic anisotropy provides the stage/background, where anisotropic impurity states are formed and are responsible for the anisotropic scattering rate. Therefore the reason for the opposite anisotropy in the two families of materials possibly lies in the different ground

state. It was theoretically proposed that, for Co-doped $BaFe_2As_2$, an impurity-induced local orbital order with broken C4 symmetry which can result in the sizable resistivity anisotropy develops in the presence of strong orbital fluctuations near T_s (Fig. 5.9(b)) [65]. On the other hand, the AFM ordering in iron telluride is bicollinear type with the ordering wave vector of (π/2, π/2) in contrast to the collinear AFM type with (π, 0) ordering in iron pnictides. The band folding effect by the (π, 0) ordering vector in the 122 materials results in the strong Fermi surface construction and the formation of new electron pockets (See Chapter 6). In contrast, the strong band construction around E_F is not expected in the 11 materials, but formation of the new coherent polaron-like quasiparticles below T_s has been reported by ARPES [53]. The distinct orbital characters in the electronic band structures near E_F between 122 and 11 materials may be related to the opposite resistivity anisotropy. Also, the interplay between the impurity and the specific electronic structure associated with the different spin configurations needs further investigation.

5.6 Summary

The in-plane resistivity anisotropy in the 11 materials has been investigated with the help of detwinning by applying uniaxial pressure. It is found that the resistivity anisotropy is mostly determined by the anisotropy in the RR component. Notably, ρ_a is higher than ρ_b, just opposite to the anisotropy observed in iron pnictide. It is also revealed that the magnitude of resistivity anisotropy increases with the amount of excess Fe or atom substitution while the AFM order is correspondingly suppressed. These results potentially suggests that the resistivity anisotropy in 11 is also induced by impurities, the same as that in 122. Therefore, the impurity-induced-anisotropy scenario may be a generic mechanism for the observed resistivity anisotropy in iron-based materials.

5.7 Supplementary information

Figure 5.10(a) shows RR plotted against the total amount of impurities for the parent and Cu-, Se-substituted $Fe_{1+x}Te$, respectively. One can see a relatively weak effect of Cu substitution on RR compared to that of excess Fe and Se. Note that this is different from the 122 materials, where the correlation between the magnitude of RR and the resistivity anisotropy has been found in the AFO phase of $Ba(Fe_{1-x}Co_x)_2As_2$. A possible explanation is given below. In the AFO phase of $Ba(Fe_{1-x}Co_x)_2As_2$, the incoherent component is (pseudo)gapped and the conductivity is dominated by the coherent Drude component [11]. As a matter of fact, a remarkable increase in both RR and resistivity anisotropy is

observed since the Co impurities are found to anisotropically broaden the width of the Drude component. In contrast, in the optical spectrum of $Fe_{1+x}Te$, the contribution of the coherent Drude component to the conductivity is limited even in the AFM state and the conductivity is largely dominated by the incoherent component [52], as shown in Fig. 5.11. The resistivity of $Fe_{1+x-y}Cu_yTe$ could then be written as

$$\rho_0(y) \equiv \rho^{residual}(y) = \frac{1}{\sigma^{incoherent}(y) + \sigma^{coherent}(y)} = \frac{1}{\sigma^{incoherent}(y) + \frac{1}{\rho_0 + ky}}$$

where y is the Cu content, k is the averaged residual resistivity produced by unit amount of impurities, ρ_0 reflects the elastic scattering effect of the preexisting excess Fe. Thus,

$$\rho_0(y) - \rho_0(0) \propto \left[\frac{k}{{\rho_0}^2}y\right] - \left[\sigma^{incoherent}(y) - \sigma^{incoherent}(0)\right]$$

$$\rho_{a0}(y) - \rho_{b0}(y) \propto \frac{k_a - k_b}{{\rho_0}^2}y$$

where k_a, k_b is the residual resistivity along a- and b-axes produced by unit amount of impurities, respectively. It should be noted that, since the incoherent component has a very large spectral width, it will not contribute to the resistivity anisotropy. One can see that the increase of RR which results from the broadening of the width of the coherent Drude component by Cu ions, could be canceled by the effect of the incoherent component. On the other hand, the resistivity anisotropy which arises from the anisotropic width of the coherent Drude component is not much affected.

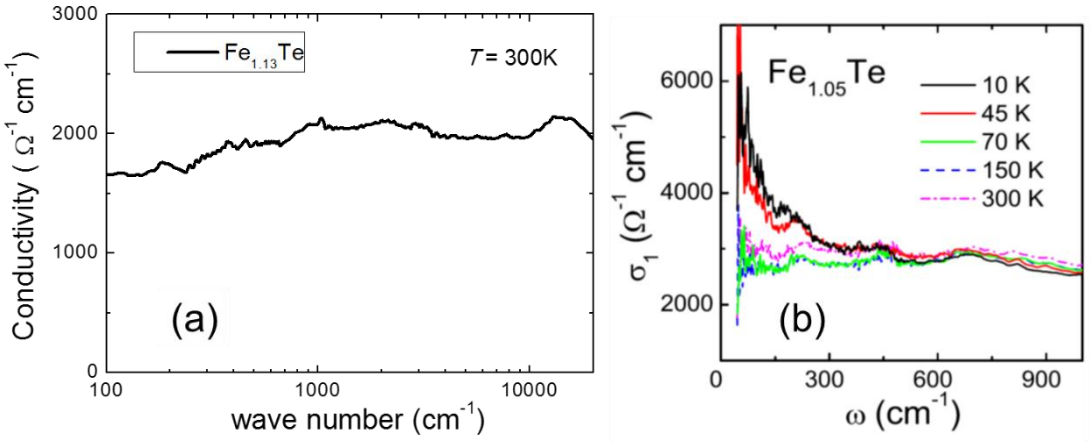

Figure 5.11 (a-b) Optical conductivity spectra for $Fe_{1+x}Te$. The conductivity spectra was obtained by the Kramers-Kronig transformation of the optical reflectance spectra. Fig. (b) is reprinted from [52].

Chapter 6

In-plane electronic anisotropy in the antiferromagnetic orthorhombic phase of $Ba(Fe_{1-x}Ru_x)_2As_2$

6.1 Introduction

In the underdoped region of the iron pnictide superconductors, there exists an antiferromagnetic-orthorhombic (AFO) phase with a broken fourfold rotational symmetry, as described in Chapter 2. A schematic drawing of the 3D BZ of the body-centered tetragonal (bct) lattice for the PM state and its folded BZ for the AFO state is illustrated in Fig. 6.1. It has been found that the major effect of doping on the AFO phase of the iron pnictides is to introduce disorder [7]. An STM study has revealed that an anomalous, anisotropic impurity state around a dopant atom is formed, which has been discussed to account for the sizable in-plane resistivity anisotropy [16]. A comparative study of the in-plane resistivity in doped $BaFe_2As_2$ with doping into three different sits (Co for Fe, K for Ba, and P for As) showed that the impurity scattering by dopant atoms becomes weaker as the dopant sites moved farther away from the Fe plane. Since Co- and K-substitutions dope the materials with carriers, it is difficult to clearly separate the carrier-doping effect from the impurity effect. Ru substitution for Fe in $Ba(Fe_{1-x}Ru_x)_2As_2$ [66] is thought to be another way to realize isovalent substitution besides P substitution for As [24]. Thus Ru substitution is an ideal access to investigating the impurity effect of doping into the Fe plane, especially compared with that of Co and P substitutions.

Moreover, previous ARPES measurements on lightly-doped $Ba(Fe_{1-x}Co_x)_2As_2$ clarified an anisotropic feature on the FSs and a d_{xz}/d_{yz} band splitting near the corner of the 2-Fe BZ, indicating a reflection of the reduced rotational symmetry [13]. The energy scale related to the band splitting is shown to be sharply suppressed for 4.5% Co substitution. However, the relationship between the results by transport and ARPES measurements is still far from well understood. In this Chapter, we also scrutinize the electronic structure of the AFO state of the isovalent-substituted $Ba(Fe_{1-x}Ru_x)_2As_2$. Combining these with the transport results, a possible origin of the anomalous impurity state shall be discussed.

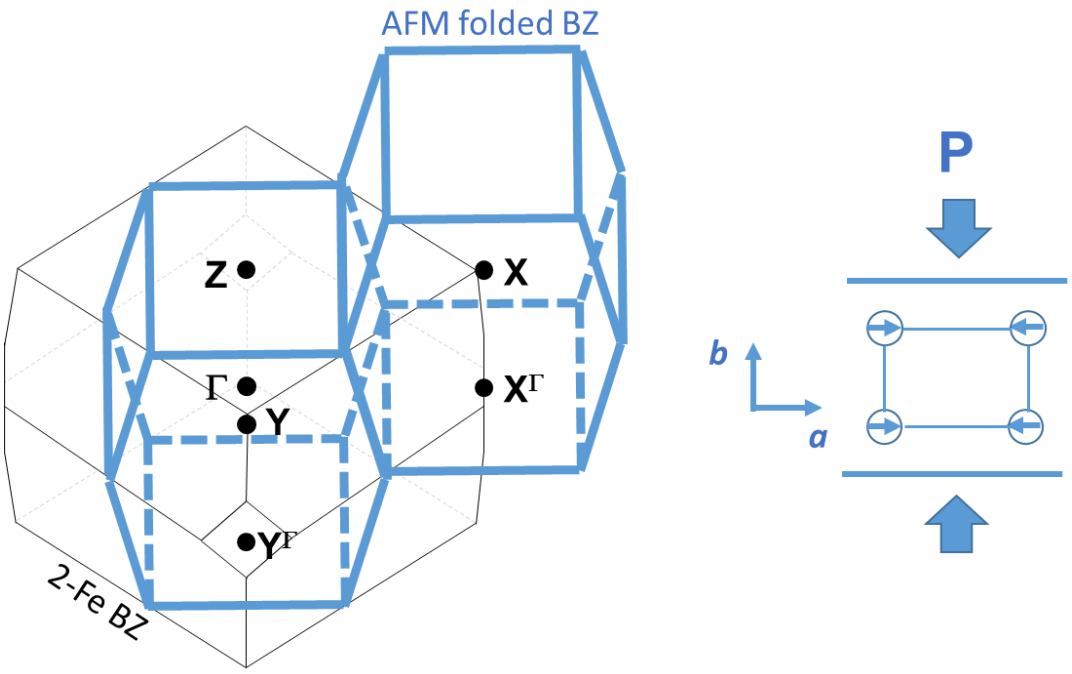

Figure 6.1 3D BZ of the bct structure for the PM state (black) and that for the AFO state (blue). Notation in the PM BZ (2-Fe BZ) is used, where Z-X/Γ-X^{Γ} is along the AFM direction and Z-Y/Γ-Y^{Γ} is along the FM direction. The right figure illustrates the crystal axis in the AFO state after detwinned by applying uniaxial pressure.

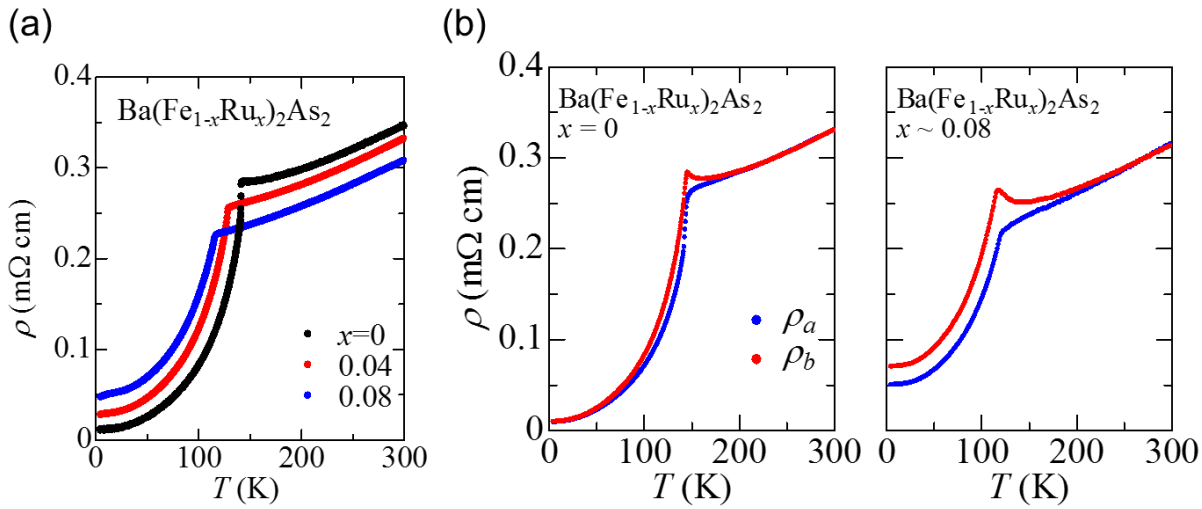

Figure 6.2 Temperature dependence of the in-plane resistivity for annealed $Ba(Fe_{1-x}Ru_x)_2As_2$ single crystals. (a) Free-standing samples. (Figure courtesy of Takuya Mikami.) (b) Detwinned samples. (The data for detwinned $BaFe_2As_2$ crystals is courtesy of Shigeyuki Ishida.)

6.2 In-plane resistivity anisotropy

Given that Ru is a 4d element, it must be chemically quite different from the 3d element Fe and thereby may introduce a strong impurity potential. Figure 6.2(a) shows the temperature dependence of the in-plane resistivity for annealed $Ba(Fe_{1-x}Ru_x)_2As_2$ (x = 0, 0.04, 0.08) crystals [67]. Surprisingly, Ru substitution exhibits a much weak effect on the increase of the residual resistivity compared with Co substitution. The results on RR for annealed Co-, Ru-, and P-substituted $BaFe_2As_2$ single crystals are summarized in Fig. 6.3 (a). One can see that the doping dependence of the residual resistivity for the Ru- and P-substituted $BaFe_2As_2$ can be described along the same line, indicating similar effects of the atoms doped into the Fe plane and the As plane on scattering carriers.

Figure 6.2 (b) shows the in-plane resistivity anisotropy measured on detwinned $Ba(Fe_{1-x}Ru_x)_2As_2$ (x = 0.08) crystals. The anisotropy in the AFO phase, $\rho_b > \rho_a$, is qualitatively the same as that of $Ba(Fe_{1-x}Co_x)_2As_2$, whereas the magnitude of the resistivity anisotropy is much smaller than that of $Ba(Fe_{1-x}Co_x)_2As_2$. As for $BaFe_2(As_{1-x}P_x)_2$, measurements of the resistivity anisotropy has been reported only on as-grown samples so far [7]. The genuine resistivity anisotropy caused by P atoms was estimated [7], as plotted with a green point in Fig. 6.3 (b). Our results for annealed $Ba(Fe_{1-x}Ru_x)_2As_2$ confirmed the appearance of the resistivity anisotropy, also with isovalent substitution.

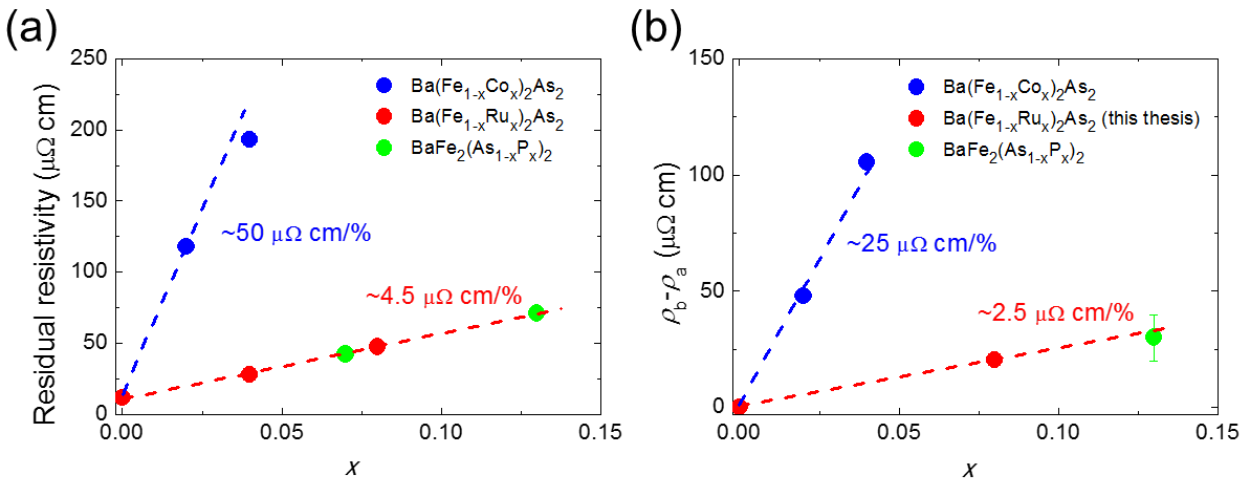

Figure 6.3 Residual resistivity (a) and in-plane resistivity anisotropy (ρ_b-ρ_a) at 5 K (b) plotted against the dopant content x for Co [6], Ru and P [7] substituted $BaFe_2As_2$ single crystals. The genuine resistivity anisotropy caused by P atoms was estimated by [7], as plotted with a green point in Fig. (b). Data for free-standing $Ba(Fe_{1-x}Ru_x)_2As_2$ are courtesy of Takuya Mikami.

Compared with the P-substituted case, one can see that the isovalent Ru-substitution and P-substitution have a similar effect on both RR and resistivity anisotropy, regardless of the substitution at the Fe sites or the As sites, reflecting the important role of the As block in iron arsenide. On the other hand, from the comparison the between Ru-substitution and Co-substitution, the much stronger impurity effect of the heterovalent substitution was revealed. Figure 6.4 (a) shows correlation between the difference of the resistivity anisotropy and RR for various atom substitutions [7], in which the result for $Ba(Fe_{0.92}Ru_{0.08})_2As_2$ is plotted. One can see a clear linear correlation between the resistivity anisotropy and RR. Generally, the elastic scattering strength of an impurity can be described by the parameter of scattering cross section. The resistivity anisotropy in FeSCs is related to the formation of anomalous impurity states around an impurity atom, which gives rise to anisotropic scattering cross sections along the *a*- and *b*-axes, as schematically shown in Fig. 6.4(b). The fact that the correlation between resistivity anisotropy and RR for various substitutions, especially Co and Ru substitution, can be described by the same line, suggests that the impurity states around different kinds of impurities (Co and Ru) have the same ratio between the cross sections along *a*- and *b*-axes, while having different scales in the spatial expansion, as shown in Fig. 6.4(b).

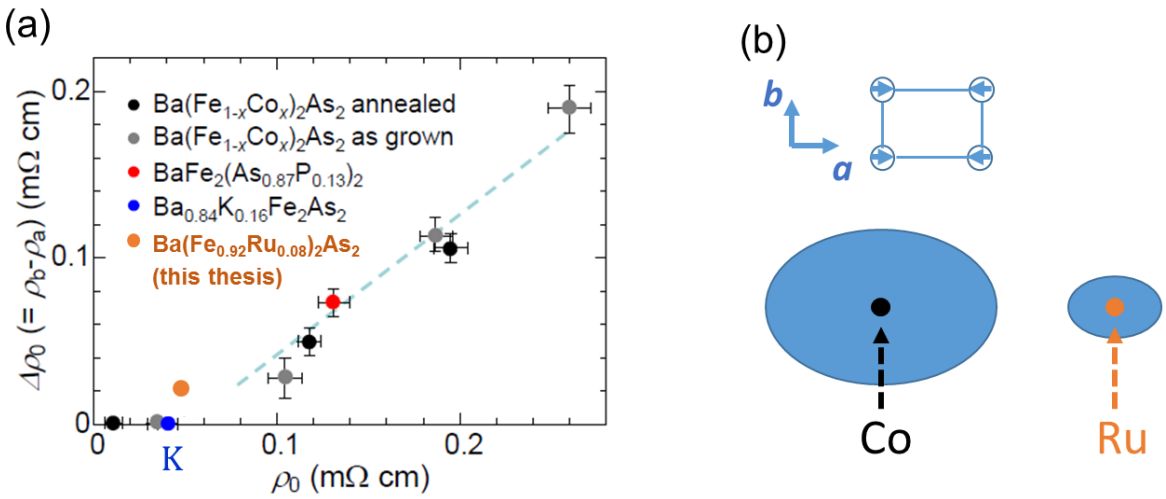

Figure 6.4 (a) In-plane resistivity anisotropy (ρ_b-ρ_a) at 5 K plotted against the residual resistivity for Ba-122 compounds with various substitutions. Reprinted from [7]. The result for $Ba(Fe_{0.92}Ru_{0.08})_2As_2$ studied in this thesis is also plotted in the figure. (b) Schematic view of the anomalous impurity state around the Co and Ru impurities, respectively.

6.3 Anisotropic electronic structure studied by ARPES

6.3.1 Experimental condition

High-quality single crystals of $Ba(Fe_{0.96}Ru_{0.04})_2As_2$ (T_s = 128 K) were grown using the self-flux method. In order to detwin the samples in the AFO phase, we applied a uniaxial compressive stress along the tetragonal (110) direction using a mechanical device illustrated in Fig. 3.10. Angle-resolved photoemission (ARPES) experiments were carried out at BL-28A of Photon Factory using a SCIENTA SES2002 electron analyzer. Circularly-polarized light was used. The total energy resolution was set to ~ 20 meV. The crystals were cleaved *in situ* at T = 20 K and measured in an ultra-high vacuum of ~ 1×10^{-10} Torr.

6.3.2 Results and discussions

Figure 6.5 shows the photon energy dependence of ARPES intensity along the X-Γ-X cut in the AFO state. All FS mappings in this chapter are made with an integration window of 10 meV about E_F. From the k_z dependence of the intensity, we may assign k_z ~ 0 for hν = 50 eV, k_z ~ $2\pi/c$ for hν = 64 eV.

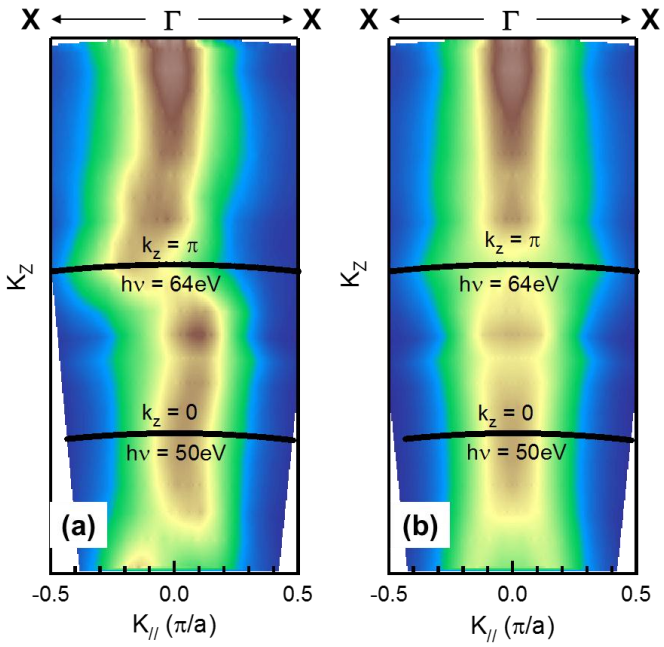

Figure 6.5 APRES intensity map in the $k_z-k_{\|}$ (X–Γ–X) plane measured at 20 K probed by varying incident photon energy (40-85 eV). The mapping shows k_z dependence. (a) raw data; (b) symmetrized with respect to $k_{\|} = 0$ line.

Using 63eV photons with $k_z \sim 2\pi/c$, FS mapping in the k_x-k_y plane was performed on the detwinned crystals in the AFO state, as shown in Fig. 6.6. One can see clear anisotropy in FS mapping intensity around the X and Y points, corresponding to the broken fourfold rotational symmetry in the AFO state. Since we used a light source with circular polarization, suppression of photoelectron intensity from each orbital subject to symmetry selection rules is not expected. We also performed the measurements with samples 90° rotated in the k_x-k_y plane, the results of which are compared in Fig. 6.6. One can see that the ARPES intensity map in the k_x-k_y plane correspondingly rotated 90°, confirming that the observed anisotropy in FS mapping is intrinsic. We also notice the resemblance in the FS intensity map between our results and those reported for $BaFe_2As_2$ by Yi *et al*. [13], indicating that the samples in our measurement were also effectively detwinned.

So far, the complete FS in the reconstructed AFO BZ of the parent compound $BaFe_2As_2$ has been investigated using detwinned single crystals using both ARPES measurement [13] and Shubnikov-de Haas oscillation measurement (Fig. 6.7) [68]. However, the agreement between each other is limited. It is shown by the ARPES measurement that FSs consist of two hole pockets and one electron pocket centered at BZ center, surrounded by two bright spots along Γ-X and two bigger petal pockets along Γ-Y. On the other hand, only one hole and two electron pockets were observed via Shubnikov-de Haas oscillation measurements. The agreement on the Sommerfeld coefficient between that evaluated based on the results of the quantum oscillation measurement and that by a direct

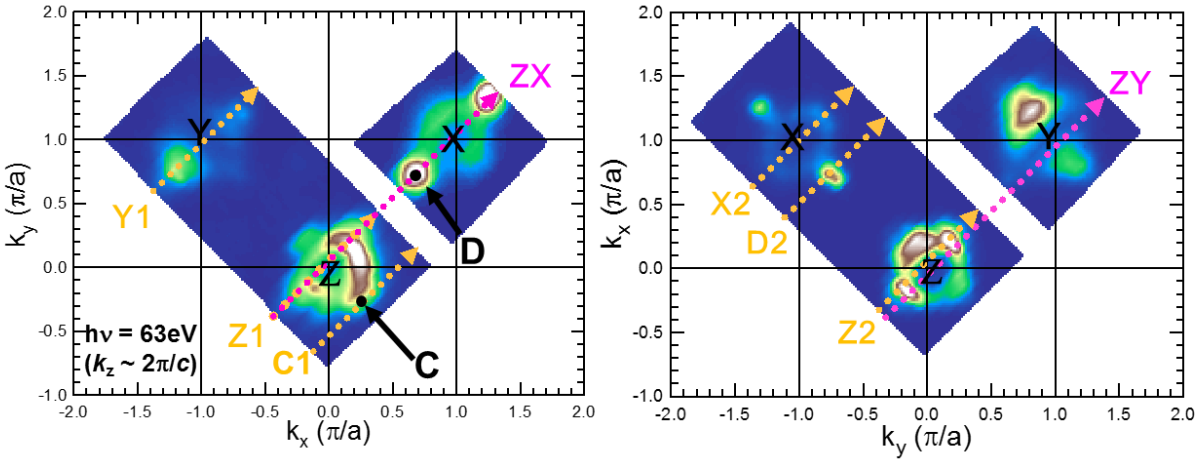

Figure 6.6 FS mapping in the k_x-k_y plane measured at 20 K. The right figure was obtained with 90° rotated in the k_x-k_y plane relative to the left one. Band dispersions along cut Z1, C1, Y1, Z2, X2, D1, ZX, and ZY, respectively, are shown in Fig. 6.8-6.9. The points C and D are also indicated.

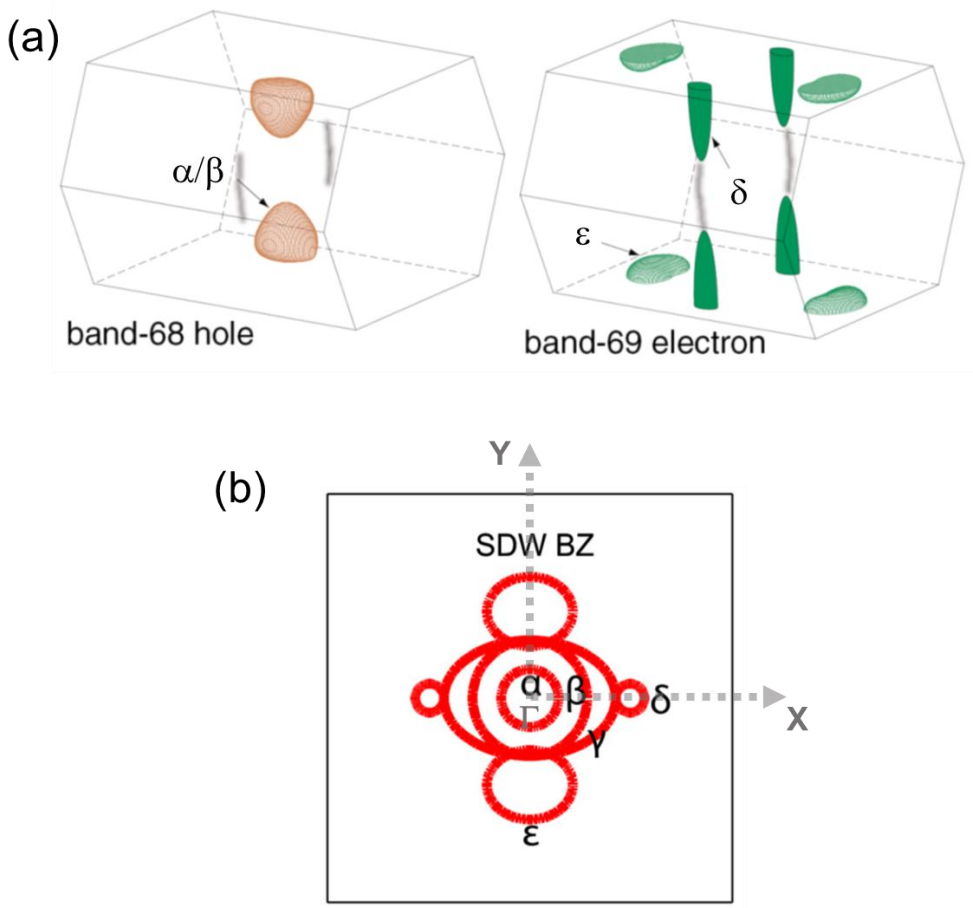

Figure 6.7 FSs of $BaFe_2As_2$ in the AFO state. (a) Determined by Shubnikov-de Haas oscillation measurement. Reprinted from [68]. (b) Determined by ARPES measurement. Reprinted from [13]. The notations of the FSs have been unified between each other.

measurement was found, which rules out existence of unobserved FS pockets of significant sizes.

Our FS mapping shows bright spots around the X point along Z-X, one of which we denote as point D. Cut D2 across this point shown in Fig. 6.6 demonstrates that it is a tiny electronic pocket, originating from the band crossing ~ 20 meV below E_F. (The size is evaluated to be 0.03% of the 2-Fe BZ.) The band dispersion is Dirac-cone-like, which was also reported in twinned samples [27]. Since FSs still seem much complicated even after the problem of multi-domains have been avoided by detwinning, it is difficult to determine other FS pockets. We then turn to the band dispersion, first focusing on cuts Z1 and Z2 across Z, as shown in Fig. 6.8. In both cuts Z1 and Z2, hole-like band

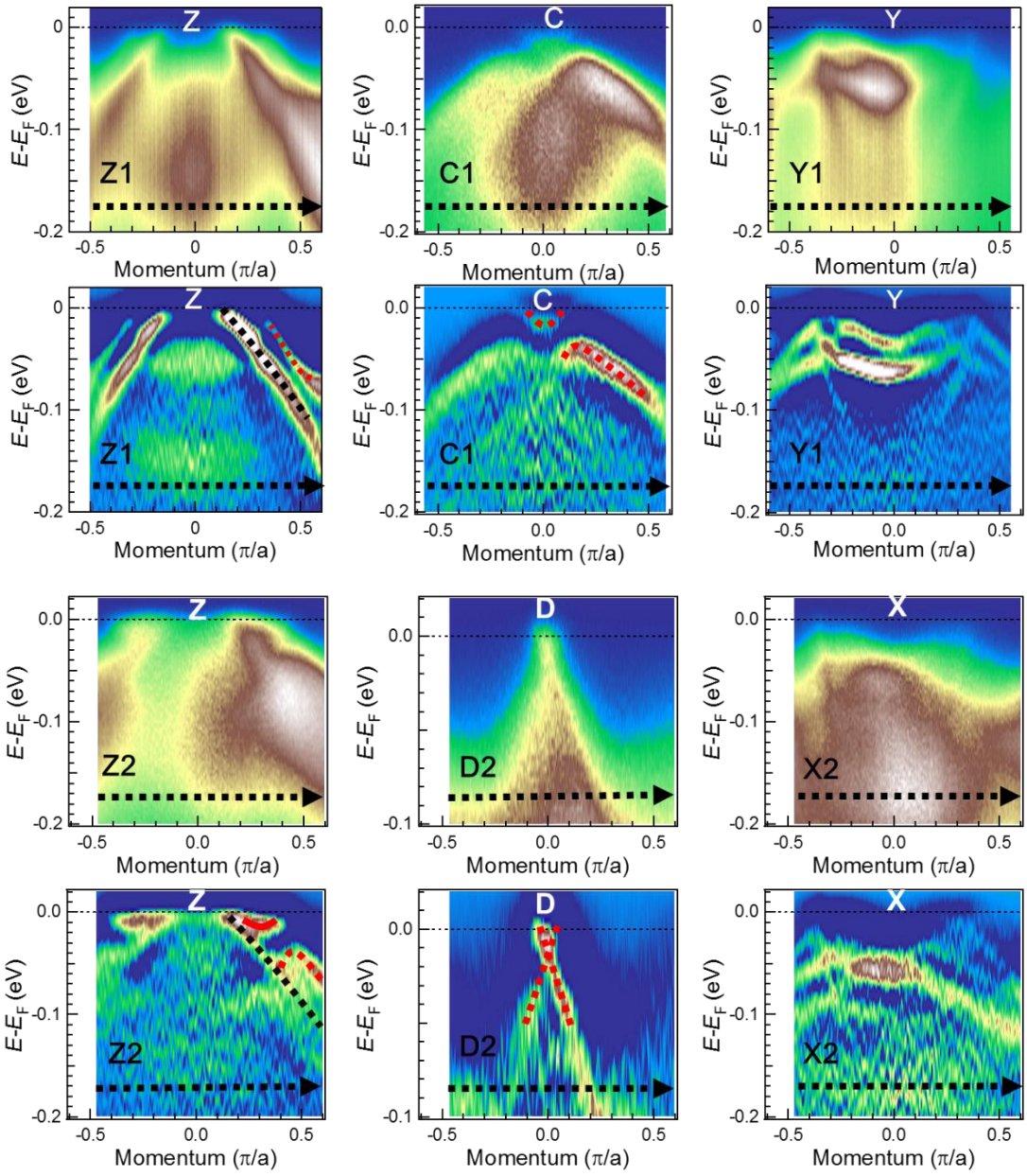

Figure 6.8 Band dispersions along cuts Z1, Z2, Y1, X2, C1, and D2, respectively, denoted in Fig. 6.6 and the corresponding energy second-derivatives of the energy-momentum (*E*-*k*) plots.

dispersions are illustrated as a guide to the eye by black broken line. Both give the same k_F value ~ ± 0.16 π/a, indicating the existence of a hole pocket with circular shape, which is consistent with the quantum oscillation measurement. A clear anisotropic feature of band dispersions on the two cuts is reflected in the outer band. As for the outer band dispersion (red broken line) of cut Z2, there seems to be a gap opening, probably due to the band folding and consequent band reconstruction, which results in the formation of

an electron pocket. More details of the pocket can be seen from cut C1, where the band reconstruction effect is clearly demonstrated with the appearance of the gap and the formation of an electron pocket. This character is different from that of cut D2, which indicates that the Dirac-cone-like electron pocket is the result of crossing between hole- and electron-like dispersions. Although cut Z2 can not tell the accurate size of this pocket along Z-Y, it is ~ 3 times larger than the Dirac-cone-like pockets, roughly based on the information of cut C1. On the other hand, cut Z1 shows only hole-like dispersion along Z-X, showing anisotropy from that of cut Z2. Because the intensity around E_F (< 20 meV) is very weak, it cannot be concluded whether there is a FS pocket or not. Given the quantum oscillation results and the observed Dirac-cone like pocket surrounding X in the neighboring AFM folded BZ, it is very likely that similar Dirac-cone-like pockets are located around Z along Z-X. If this is the case, our results are consistent with the quantum oscillation measurement in reaching FSs, although the measured sample here is with 4% Fe substituted by Ru.

One more important feature manifesting the broken fourfold rotational symmetry of the electronic structure in the AFM state is an anisotropic band shift with d_{xz} orbital character around Y and d_{yz} orbital character around X, both of which are degenerate in the PM state. As temperature is lowered toward T_s, the d_{yz} band along Γ-X shifts up and crosses E_F, whereas the d_{xz} band along Γ-Y shifts down. The band dispersions along Z-X and Z-Y in $Ba(Fe_{0.96}Ru_{0.04})_2As_2$ are shown in Fig. 6.9. One can see a similar appearance of the anisotropy in the band splitting along Z-X and Z-Y (marked by red broken lines).

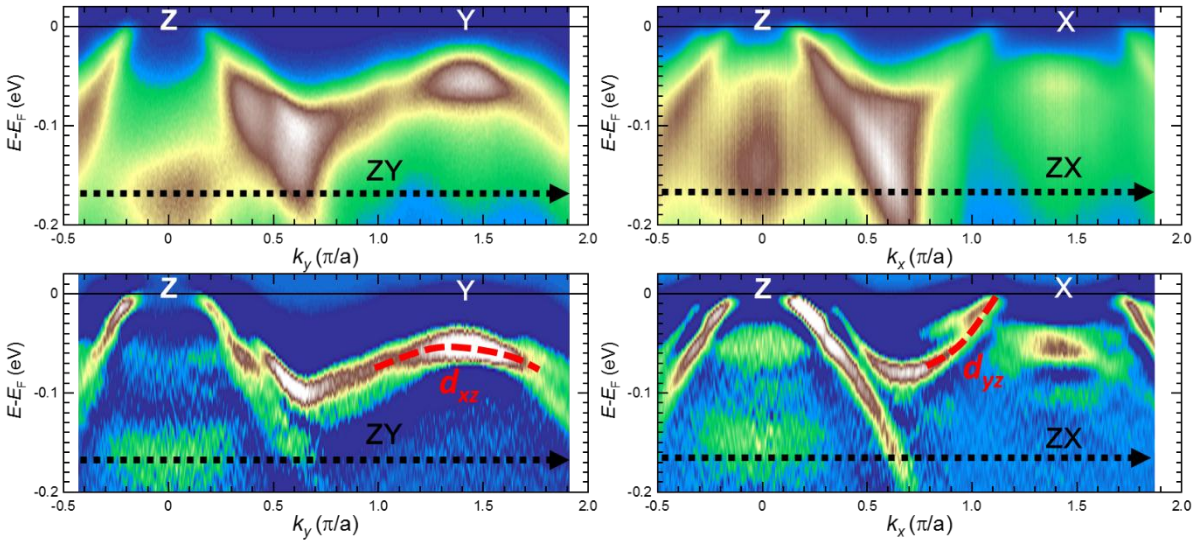

Figure 6.9 Spectral image plots along high-symmetry lines and their energy second-derivatives demonstrating the anisotropy in the band dispersions.

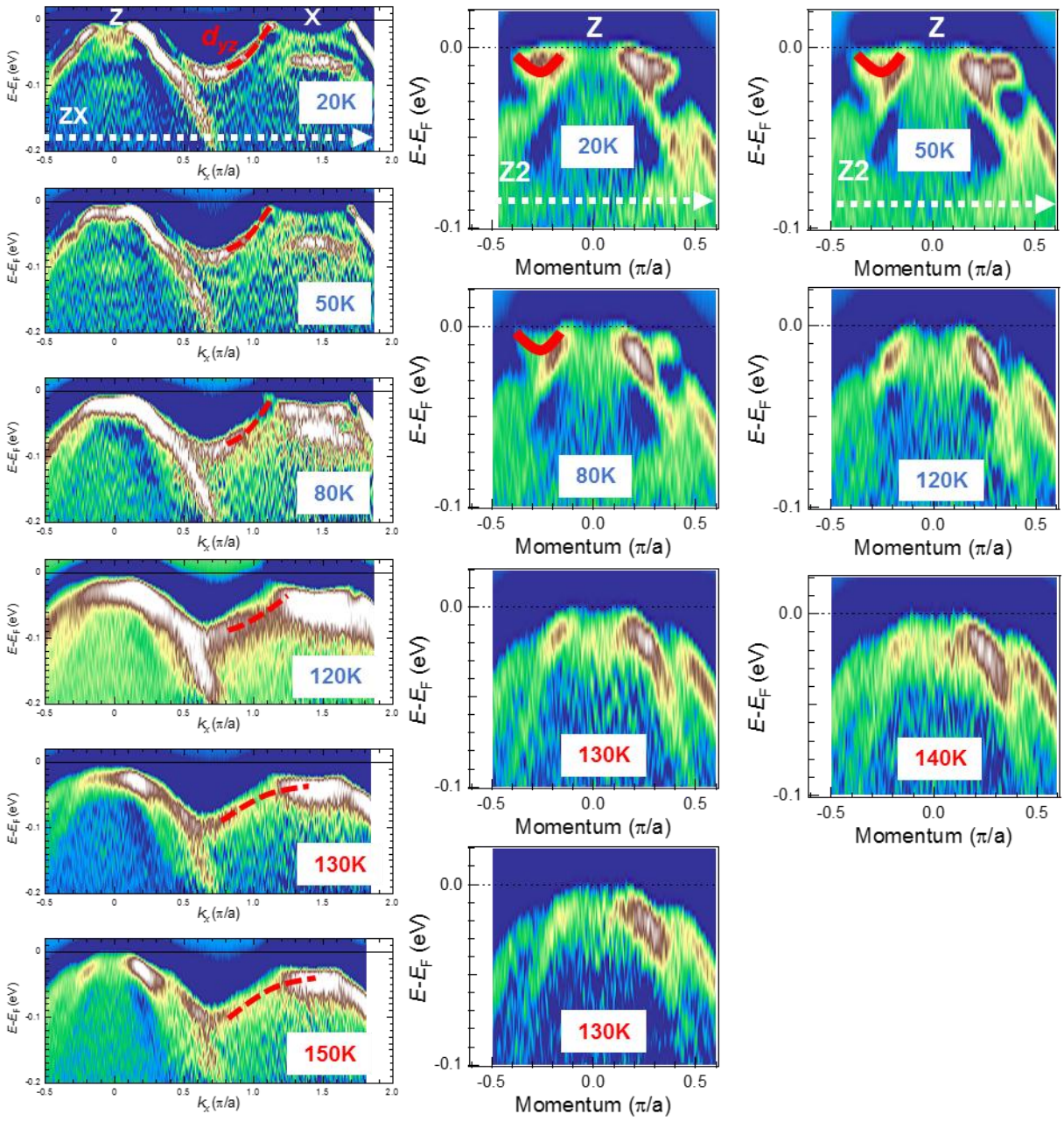

Figure 6.10 Evolution of band structures along high symmetry cuts with increasing temperature across T_s/T_N.

Our measurements using a P-polarized light with the polarization vector in the mirror plane of the analyzer slit show a sharp suppression of the intensity both along Z-X around X and along Z-Y around Y, confirming the same orbital character as that determined for the $BaFe_2As_2$ [13].

In order to further investigate the evolution of the spectral images along high-symmetry

lines with increasing temperature, we performed a temperature-dependent study. Figure 6.10 shows the evolution of band dispersions along the Z-X and Z2 cuts with temperature. The band with d_{yz} orbital character crosses E_F near X at 20 K and sinks below E_F with temperature across T_s/T_N. As for cut Z2, the electron pockets located around Z, as shown by red lines in Fig. 6.10, disappear and finally two hole pockets show up in the PM phase while no large band shift is observed. If compared with the spectral images along cut Z-X above T_s/T_N, one can see the same band dispersion around Z, since equivalency can be expected from the fourfold rotational symmetry in the PM phase. It should also be noted that even at 120 K the d_{yz} band has shifted down a lot, much close to that above T_s/T_N. This may be ascribed to the surface effect of samples, which leads to a slight suppression in T_s/T_N compared to that of bulk.

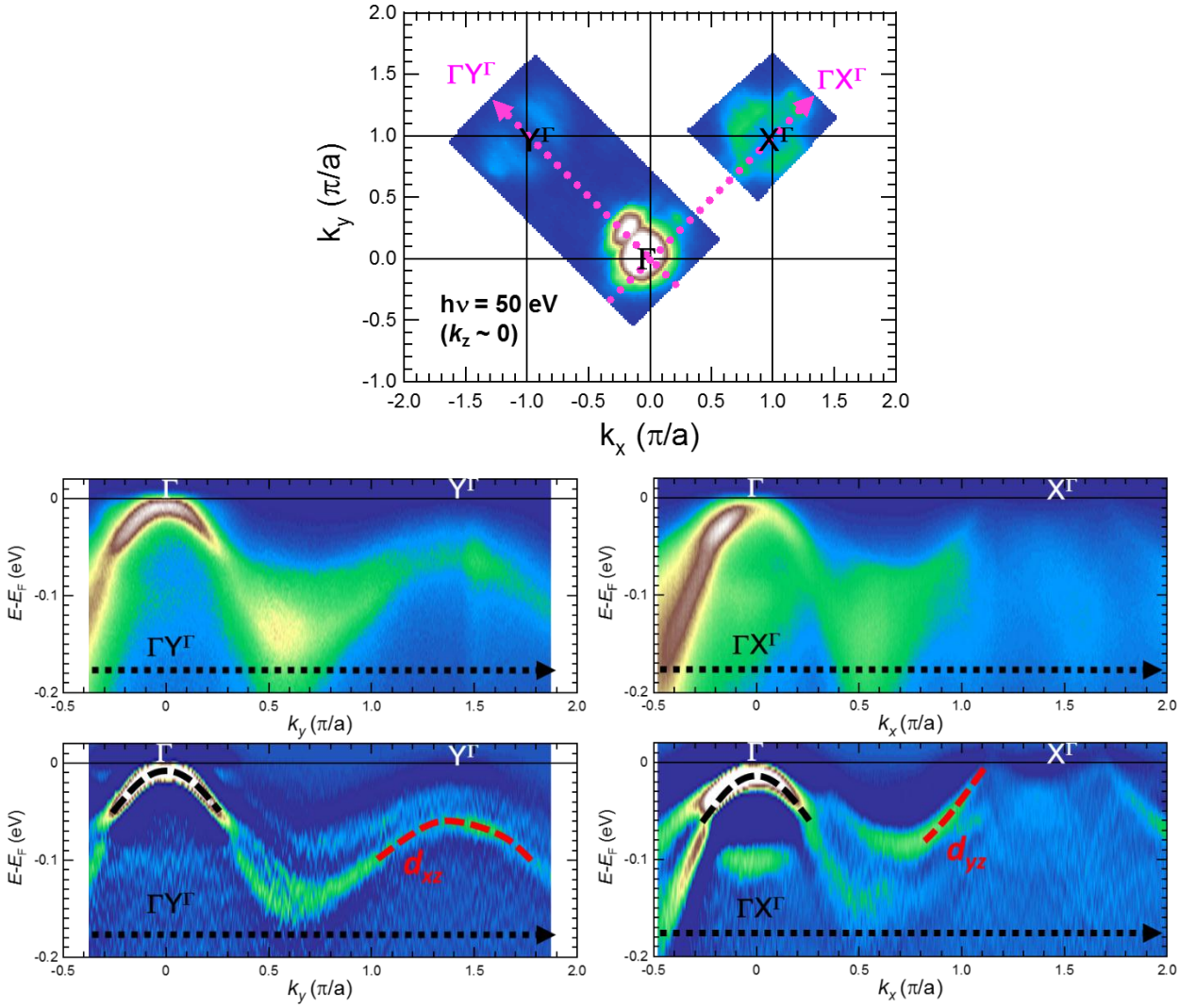

Figure 6.11 FS mapping in the k_x-k_y plane measured at 20 K using hν = 50 eV (figure above); Spectral images along high-symmetry lines and their energy second-derivatives (figures below).

As shown in Fig. 6.7(a), Shubnikov-de Haas oscillation measurements demonstrate that all of the FS pockets are three dimensional and closed, indicating a non-negligible dispersion along the k_z direction. In order to clarify the k_z dependence of the electronic structure, we also performed an ARPES measurement using 50 eV photons, roughly corresponding to $k_z \sim 0$ at BZ center. The FS intensity map is shown in Fig. 6.11. Although the intensity is weak, similar shape around X and Y to that obtained by 63 eV photons can be seen, whereas the appearance of the intensity map around Γ is somewhat different. The bright petal along Γ-Y^{Γ} and the relatively weak spot along Γ-X^{Γ} implies the survival of the two kinds of electron pockets. The spectral images along high symmetry lines Γ-X^{Γ} and Γ-Y^{Γ} may give more information. The most anisotropic feature near X^{Γ} and Y^{Γ} is robust, that is, the hole-like pocket crosses E_F at almost the same k_F near X^{Γ}, where the Dirac-cone-like electron pocket is situated when using 63 eV photons. This is probably related to the possible existence of tiny pockets marked by the grey line in Fig. 6.7(a). On the other hand, the energy scale related to the band splitting, e.g., energy difference between the hole like dispersions near X^{Γ} and Y^{Γ} at momentum $k = 0.9\pi/a$, is much larger (~ 55 meV, magnitude similar to that in $BaFe_2As_2$) than that with $k_z \sim \pi$ (~ 15 meV), as shown in Figure 6.12. Band dispersions near Γ show a downward shift below E_F

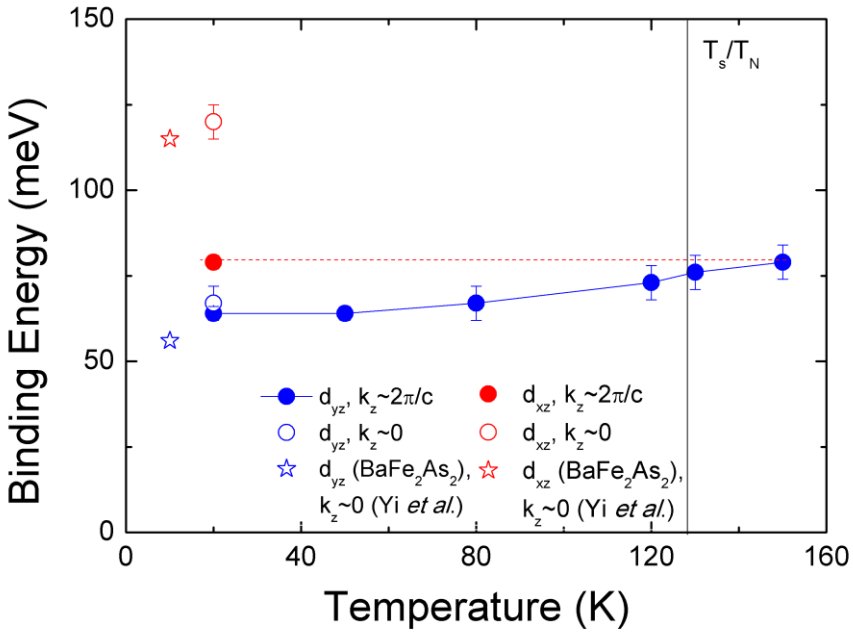

Figure 6.12 Energy positions of the d_{xz} and d_{yz} bands relative to E_F at momentum $k = 0.9\pi/a$ plotted as a function of temperature. The data for $BaFe_2As_2$ are reproduced from [13].

compared to that taken at 63 eV photons. As a results, the hole pocket disappears, indicating its nature of strong three dimensionality, consistent with the quantum oscillation measurement. Along Γ-Y^{Γ} beside Γ, there seem to exist band dispersions about E_F, implying the existence of electron pockets (FS δ in Fig. 6.7(a)) as in the case of 63 eV. However, it is shown in the oscillation measurement that these electron pockets are also highly three dimensional.

It has been shown that the energy scale related to the d_{xz}/d_{yz} band splitting is sharply suppressed for 4.5% Co substitution, ~ 25 meV with $k_z \sim 0$ [13], while it is ~ 55 meV for 4% Ru substitution. On the other hand, the magnitude of the resistivity anisotropy for Co-substituted $BaFe_2As_2$ is ~ 10 times larger than that for $Ba(Fe_{1-x}Ru_x)_2As_2$, suggesting that there is no direct correlation between the two features of electronic anisotropy. Moreover, a clear correlation between the magnitude of the residual resistivity and the resistivity anisotropy in the Ru isovalent- and Co electron-substituted 122 materials strongly support the extrinsic origin of the resistivity anisotropy, that is to say, the dopants/impurities anisotropically scatter carriers with the formation of an exotic impurity state. In this scenario, the AFO phase provides the stage/background for it. However, it was reported that there is no discernable resistivity anisotropy in the hole-doped $Ba_{1-x}K_xFe_2As_2$ ($x \geq 0.1$) [7, 9, 69]. Although the scattering strength of the K atoms is very weak, the disappearance of the temperature dependence of the resistivity anisotropy is not expected. Given this fact, we shall discuss the possible clues on the origin of the exotic impurity state based on our ARPES measurements. It has also been described previously that three types of Fermi pockets were resolved, the two electron pockets of which arise from the band folding and consequent band construction around E_F. Both bottoms of the corresponding dispersions are ~ 20 meV below E_F. In the rigid-band model, a certain amount of K hole-doping would result in the disappearance of the two electron pockets, whereas they survive upon isovalent- and electron-doping. Thus, it is very likely that the observed resistivity anisotropy in the 122 compounds is related to the electron pockets the carriers of which are scattered anisotropically.

6.4 Summary

The resistivity anisotropy was observed in $Ba(Fe_{1-x}Ru_x)_2As_2$, the sign of which is the same as that in $Ba(Fe_{1-x}Co_x)_2As_2$ and the magnitude is relatively small. ARPES measurements using 63 eV photons ($k_z \sim 2\pi/c$) on detwinned $Ba(Fe_{0.96}Ru_{0.04})_2As_2$ crystals were also performed. It is shown that FSs in the AFO phase consist of three types of pockets: isotropic hole pocket, Dirac-cone-like tiny electron pocket along Z-X and

another relatively larger electron pocket along Z-Y, which is well consistent with the complete FSs, albeit of parent compound $BaFe_2As_2$, determined by quantum oscillation measurements. The most anisotropic feature in band dispersions is the d_{xz}/d_{yz} band splitting around 2-Fe BZ corner, similar to that reported in $Ba(Fe_{1-x}Co_x)_2As_2$. Our results also demonstrate a strong three dimensional character either in the hole pocket, or in the energy scale related to the band splitting which is one of the important reflections of the anisotropic electronic structure. Our results indicate no direct correlation between the energy scale of the band splitting and the magnitude of the resistivity anisotropy. We speculate that the key parameter of the resistivity anisotropy is possibly related to the anisotropic scattering on the electron pockets.

Chapter 7
Superconducting gap of $Ba(Fe_{0.65}Ru_{0.35})_2As_2$ observed by angle-resolved photoemission spectroscopy

7.1 Introduction

The superconducting (SC) order parameter in FeSCs has been intensively discussed and investigated due to its close relationship with paring interaction [17]. However, even for the most studied 122 system, the situation is still fairly complex. As for the optimally isovalent substituted $BaFe_2(As_{1-x}P_x)_2$ (x = 0.33) compound, it was revealed by the penetration depth and thermal conductivity measurements that there exist line nodes in the SC gap structure [70]. Recent ARPES experiments showed a circular horizontal node at $k_z = 2\pi/c$ on the three-dimensional (3D) hole FS of $BaFe_2(As_{1-x}P_x)_2$ (x = 0.3) [71]. It has been pointed out based on the random phase approximation (RPA) calculation that, 3D nodal structures appear around Z point in the largely warped hole FS, which has a strong d_{z^2} orbital character [72]. Thus, it is interesting to investigate whether such a feature of the SC gap is common or not in another isovalent substituted iron pnictide superconductors $Ba(Fe_{1-x}Ru_x)_2As_2$, which also exhibits a highly warped hole FS along k_z direction [66]. Indeed, recent thermal conductivity measurements suggest nodal superconductivity in both optimally doped and underdoped $Ba(Fe_{1-x}Ru_x)_2As_2$ [73]. In order to clarify the SC gap structure and the location of the suggested nodes in the momentum space, we performed an ARPES study of 35% Ru-substituted $BaFe_2As_2$.

In this study, two kinds of APRES experiments were performed. One is bulk-sensitive laser-ARPES, the other is based on a synchrotron radiation photon source, which allows us to trace the k_z dependence of the SC gap by tuning the incident photon energy. Calibration of the Fermi level (E_F) of the samples was achieved by referring to that of gold. In-plane (k_x, k_y) and out-of-plane momenta (k_z) are expressed in units of π/a and $2\pi/c$ [23], where a = 4.03 Å and c = 12.76 Å are the in-plane and out-of-plane lattice constants , respectively. Here, x and y axes point toward the tetragonal (100) direction.

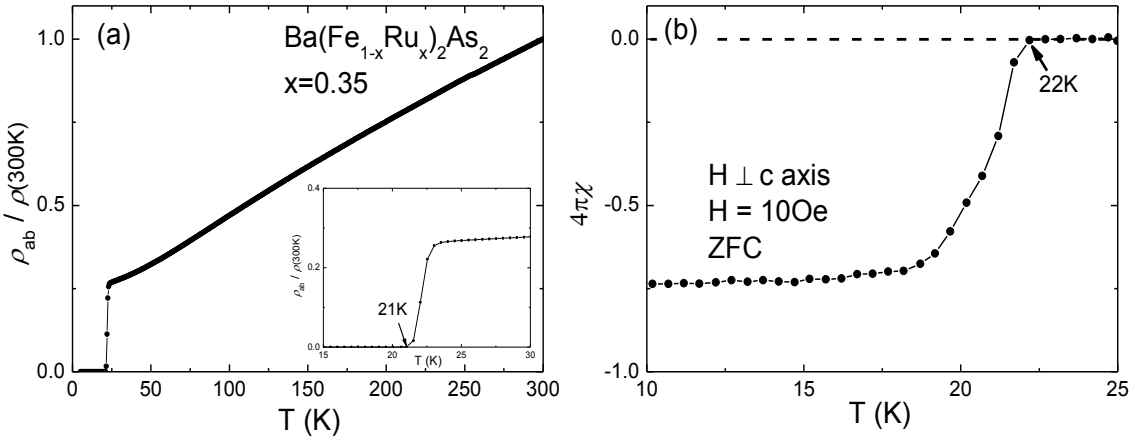

Figure 7.1 (a) Temperature dependence of the normalized resistivity of $Ba(Fe_{1-x}Ru_x)_2As_2$ (x = 0.35). Inset shows an enlarged plot around T_c. (Data courtesy of Takuya Mikami.) (b) Temperature dependence of the dc magnetic susceptibility of $Ba(Fe_{1-x}Ru_x)_2As_2$ (x = 0.35).

Magnetic measurements indicate an onset of superconductivity at ~ 22 K while resistivity measurements exhibit the zero resistivity at ~ 21 K, as shown in Fig. 7.1. This is higher than that of the reported optimal composition (~ 20 K) [74], indicating good quality for our measured samples. The superconductivity transition width is 2-3 K, which is broader than that of $BaFe_2(As_{1-x}P_x)_2$ with a typical width of less than 0.5 K [36]. This is presumably due to the inhomogeneity of Ru content in the grown single crystals, since the larger ion size of Ru would result in difficulty with substitution.

7.2 Laser-excited ARPES study

7.2.1 Experimental condition

Laser-ARPES experiments were carried out at the Institute of Solid State Physics (ISSP, Japan) [45]. The VG-Scienta HR8000 analyzer and 6.994 eV quasi-CW laser were used with the total energy resolution set to ~ 3 meV for FS mapping and ~ 1.2 meV for SC gap measurement. The angular resolution was 0.1 deg. Crystals were cleaved *in-situ* at T = 3 K in an ultrahigh vacuum better than 2×10^{-11} Torr.

7.2.2 Results and discussions

Figure 7.2(a) shows the FS intensity map using a left-circularly polarized light. Two hole FSs can be resolved, namely α and β respectively, as indicated by red and blue markers. It is revealed in Fig. 7.4 (a) that 7 eV photons probe the hole FSs profile near Z.

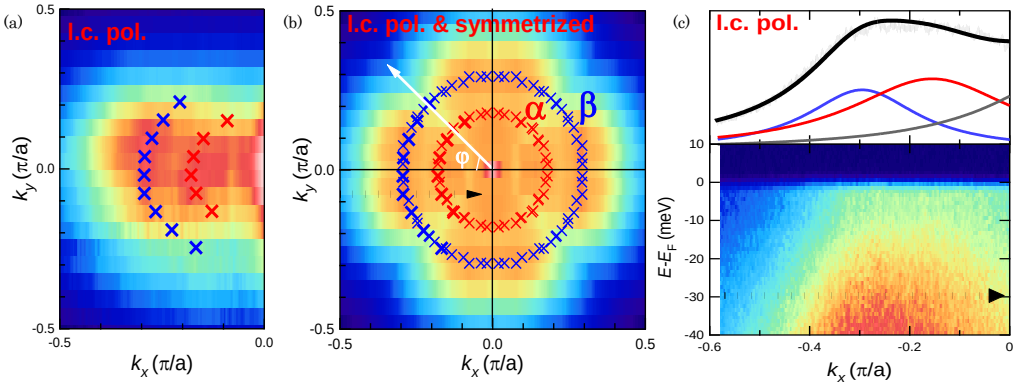

Figure 7.2 (a) FS intensity map of $Ba(Fe_{0.65}Ru_{0.35})_2As_2$ measured at 25 K with left-circularly polarized light. (b) FS image map obtained by symmetrizing the spectra in (a), taking into account the tetragonal fourfold rotational symmetry. The integration energy window is ± 5meV around E_F. The red and blue markers indicate the positions of k_F for the two hole FSs, namely α and β, respectively. Definition of the FS angle φ is also shown. (c) MDC at E_F and E-k map for the cut as indicated by the broken line in (b). The k_F positions were determined by fitting the MDC at E_F to the three Lorentzians. The red one and the blue one correspond to α and β FSs respectively, while the grey one arises from the contribution of k_F on the other side of α FS.

In order to have a full view of the hole FSs, we have symmetrized the experimentally obtained FS intensity map and obtained the image map of Fig.7.2(b) by taking into account the tetragonal fourfold rotational symmetry of the crystal structure. One can see that both of the two observed FSs are almost circular.

We then turn to the SC gap of $Ba(Fe_{0.65}Ru_{0.35})_2As_2$ in the k_x-k_y plane. Figure 7.3(c) shows the temperature evolution of the energy distribution curves (EDCs) at one k_F on the β FS. With decreasing temperature below T_c, the leading edge shifts to the lower energy and a peak-like structure develops, clearly indicating the opening of a SC gap. The FS angle φ is defined as indicated in Fig. 7.2(b). Figure 7.3 (a)-(b) show the EDCs at k_F below T_c (~ 3 K) and above T_c (~ 25 K) on the α and β FSs for the various FS angles. In order to cancel out the effect of Femi-Dirac cutoff, EDCs were symmetrized with respect to E_F. One can see a significant loss of intensity at E_F and the formation of a peak-like structure below and above E_F in the symmetrized EDCs. To make clear the SC gap energy, vertical solid bars are added where the intensity begins to weaken in the symmetrized EDCs. As with the $BaFe_2(P_{0.65}As_{0.35})_2$ and $Ba_{0.6}K_{0.4}Fe_2As_2$ [75], the observed SC gap on the hole FSs is almost isotropic and FS-independent also for $Ba(Fe_{0.65}Ru_{0.35})_2As_2$. The magnitude is ~ 2.5 meV for $Ba(Fe_{0.65}Ru_{0.35})_2As_2$.

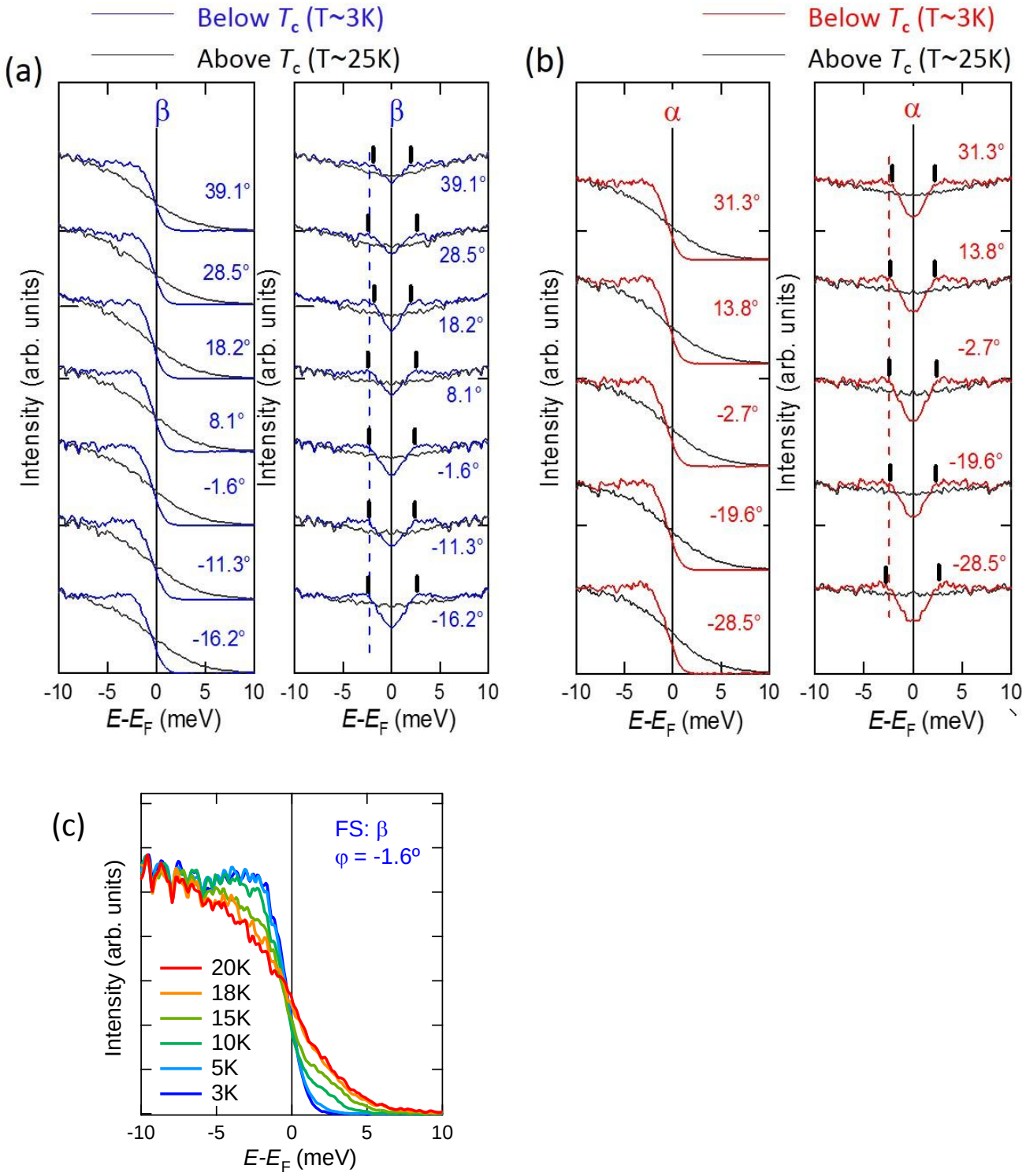

Figure 7.3 (a)-(b) EDCs and symmetrized EDCs at k_F measured below T_c (~ 3 K) and above T_c (~ 25 K) for various FS angles. Vertical solid bars indicate the gap energy for the various FS angles. The dashed lines are guides to the eye at the energy of -2.5 meV. (c) Temperature dependence of EDCs at a k_F on the β FS.

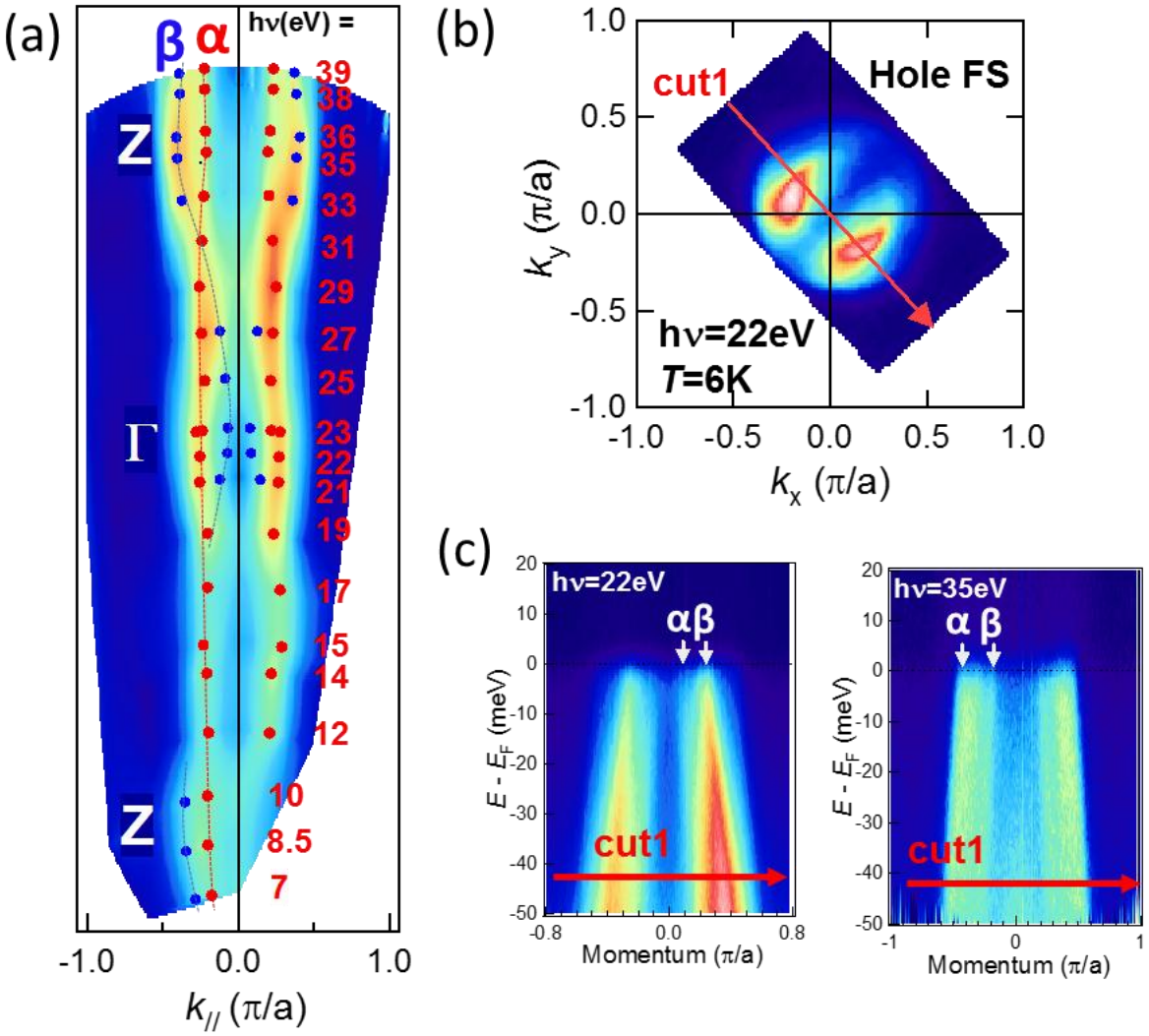

Figure 7.4 Hole FSs and band dispersions of $Ba(Fe_{0.65}Ru_{0.35})_2As_2$. (a) Photon energy dependence of ARRES intensity map of cut1 (shown in (b)) measured at 6 K, showing k_z dependence of the hole FSs (7-39 eV). Red and blue dots indicate k_F positions of FS α and β respectively. (b) FS mapping around zone center in the k_x-k_y plane taken at 22 eV. (c) Band dispersions corresponding to cut1 in (b) taken at 22 eV (near Γ) and 35 eV (near Z), respectively.

7.3 ARPES study using synchrotron light

7.3.1 Experimental condition

ARPES experiments were performed at beamline 5-4 of Stanford Synchrotron Radiation Lightsource (SSRL) with a Scienta R4000 analyzer. The energy resolution was 6-8 meV for gap measurements depending on the photon energy. Crystals were cleaved *in-situ* at 6 K in an ultrahigh vacuum of ~ 2.5×10^{-11} Torr.

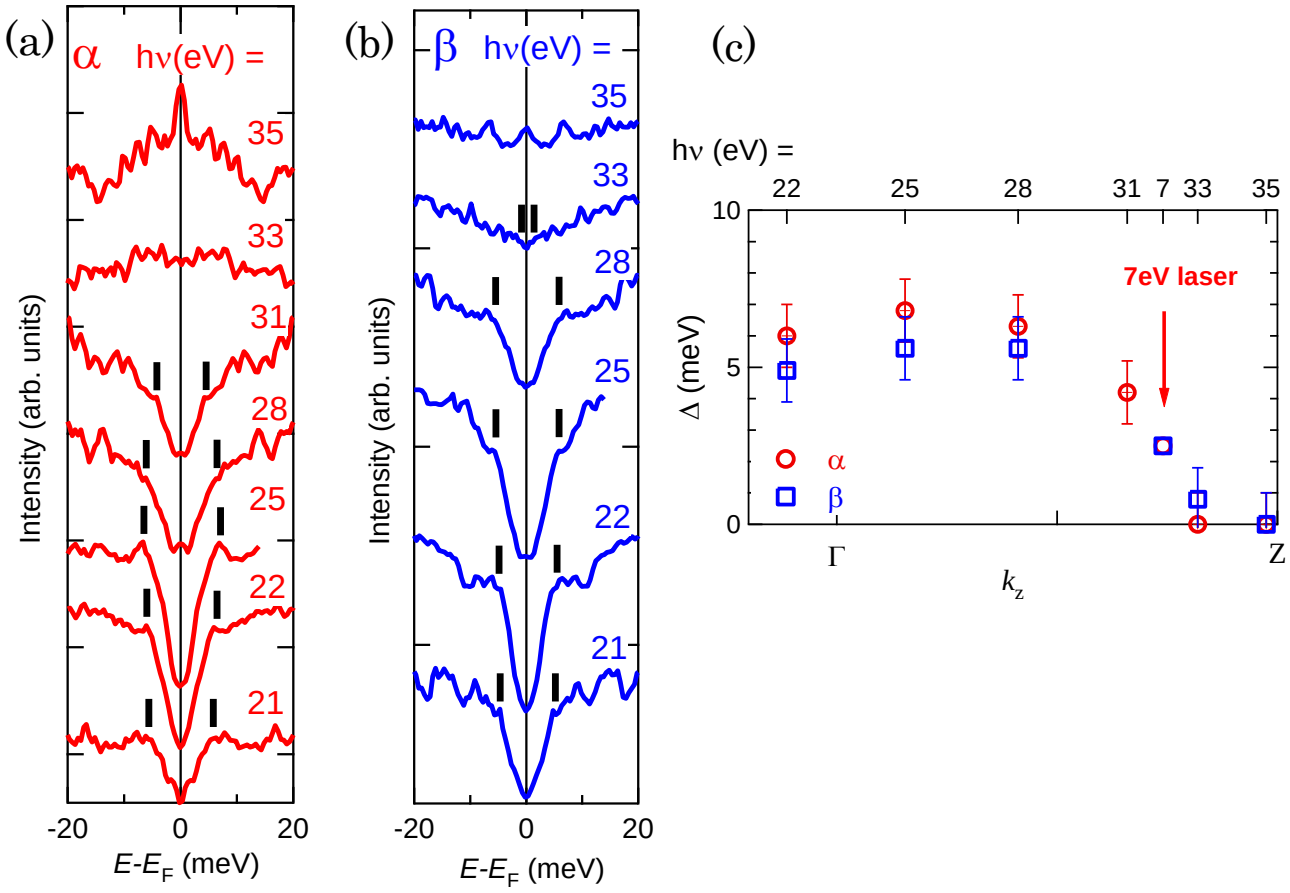

Figure 7.5 (a)-(b) Symmetrized EDCs at k_F positions of hole FS α and β along cut1 in Fig. 7.4(b) taken at various photon energies below T_c (~ 6 K). (c) SC gap on hole FSs in (a)-(b) plotted as a function of incident photon energy, showing a strong k_z dependence. By comparing k_F value between data obtained by laser-ARPES and that probed by synchrotron light, k_z probed by 7 eV photons is one period smaller than that probed by ~ 32 eV photons. The SC gap magnitude measured by laser-APRES is also correspondingly plotted in (c).

7.3.2 Results and discussions

Figure 7.4 shows the hole FSs and band dispersions of $Ba(Fe_{0.65}Ru_{0.35})_2As_2$ observed by ARPES. Here, two hole FSs, namely α and β, can be resolved both for hν = 22 eV and 35 eV. On the other hand, the band-structure calculation for $Ba(Fe_{1-x}Ru_x)_2As_2$ (x = 0.38) [76] found three hole FSs around Z. The outer-most pocket with dominant d_{z^2} character shows the strongest 3D dispersion. We could not distinguish another hole FS around Z in

the ARPES spectra, which is probably attributed to the matrix element effect. From the k_z mapping in Fig. 7.4(a), one can see the strongly warped feature of the β FS, suggesting that it has a dominant d_{z^2} orbital character around Z. Assuming that the inner potential is 14.5 eV, the corresponding k_z within the photon energy range of 22-39 eV can be well fitted under the free-electron final state model, where $k_z = 0$ at ~ 23 eV and $2\pi/c$ at ~ 35 eV. On the other hand, in the low photon energy region (< 21 eV), the free-electron final state model seems to become inaccurate. Relatively larger FSs appear around 8.5 eV, implying the location of the next Z point. Thus, one can see that 7 eV photons probe the hole FS profile near Z. By further comparing with k_F values measured with higher photon energies, k_z probed by 7 eV photons is one period smaller than that probed by ~ 32 eV photons.

Symmetrized EDCs at k_F of the hole FSs for various hν's are presented in Fig. 7.5 (a)-(b). One can see clear gap structures both on the α and β FSs around Γ, whereas no clear gap opening can be observed around Z. Figure 7.5(c) summarizes the k_z dependence of the SC gap magnitude, where the data obtained by 7 eV-laser ARPES is also plotted. The SC gap magnitude measured by laser-ARPES is consistent with the k_z dependence of SC gaps on the hole FSs measured using synchrotron light. Combining both data gives a clear SC gap anisotropy on hole FSs along the k_z direction, that is, the gap minimum appears around Z, although our measurements could not distinguish whether the SC gap magnitude becomes zero or a small non-zero value due to the limited energy resolution.

The SC gap on the electron FSs of $Ba(Fe_{0.65}Ru_{0.35})_2As_2$ was also investigated using 21 eV photons. Two electron FSs can be clearly resolved as shown in Fig. 7.6(b). If one uses the inner potential of 14.5 eV obtained from fitting the hν dependence of k_z around zone center, k_z around the zone corner probed by 21 eV photons is ~ 5.3 ($2\pi/c$), which is qualitatively consistent with the shape of the electron FS expected from the k_z value. Symmetrized EDCs at k_F measured below T_c are presented in Fig. 7.6(c)-(d), showing an almost isotropic character in the k_x-k_y plane of momentum space.

As introduced previously, thermal conductivity measurements found a large residual κ_0/T at zero field and a $\sqrt{H}$ dependence of $\kappa_0(H)/T$ in $Ba(Fe_{1-x}Ru_x)_2As_2$ (x = 0.36), strongly suggesting the existence of nodes in the SC gap structure [73]. The isotropic SC gap opening in the k_x-k_y plane both on hole FSs observed by 7 eV-laser ARPES and on the electron FSs probed by 21 eV photons rules out the existence of "vertical" line nodes, which has been found in the heavily K-doped 122 materials [77]. It has been also predicted based on the spin-fluctuation-mediated mechanism that "horizontal" line node on the highly warped hole FS with the strong d_{z^2} orbital character [72] or line-nodes of closed loops on one of the electron pockets may appear when the three-dimensionality

becomes significant. Recent ARPES measurements on $Ba(Fe_{1-x}Ru_x)_2As_2$ (x = 0.25) suggested a 3D isotropic SC gap [78], whereas thermal conductivity measurements on $Ba(Fe_{1-x}Ru_x)_2As_2$ (x = 0.23) support the presence of nodal superconductivity, but with a much smaller κ_0/T than that of $Ba(Fe_{1-x}Ru_x)_2As_2$ (x = 0.36) [73]. Our results found a strong k_z dependence of the gap magnitude on hole FSs in $Ba(Fe_{1-x}Ru_x)_2As_2$ (x = 0.35). This composition shows a more strongly warped feature on one hole FS and appearance of the SC gap minimum around Z point. The emerging SC gap anisotropy upon Ru substitution observed by ARPES might be related to the enhancing κ_0/T at zero field. As predicted for $BaFe_2(As_{1-x}P_x)_2$, a 3D nodal structure would appear on the strongly warped hole FS with a dominant d_{z^2} orbital character upon lowering the pnictogen height by P substitution [72]. In analogy with the case of P substitution, a similar case might happen in $Ba(Fe_{1-x}Ru_x)_2As_2$, that is, a 3D sign change of the SC gap takes place originating from the growing warping feature of the hole FS upon Ru substitution. This results in the emerging gap minimum around Z point observed by ARPES and the enhancing κ_0/T revealed by thermal conductivity measurement. It should be noted that both hole FSs in $Ba(Fe_{0.65}Ru_{0.35})_2As_2$ resolved by ARPES exhibit a gap minimum whereas the "horizontal" nodes predicted by the RPA calculation only appear on the highly warped hole FS. The inconsistency is unclear at the moment.

7.4 Summary

We performed an ARPES study of the superconducting gap in isovalent-substituted $Ba(Fe_{1-x}Ru_x)_2As_2$ (x = 0.35) using 7 eV laser and synchrotron light photons. Both SC gaps on the hole FSs studied by 7 eV-laser ARPES and those on the electron FSs probed by 21 eV photons are isotropic in the k_x-k_y plane, suggesting the inexistence of "vertical" line nodes. By tuning the photon energy, SC gaps measured on hole FSs showed a strong k_z dependence, namely, the gap minimum appears around the Z point, implying the possible existence of "horizontal" line nodes near Z, which could be responsible for the large residual κ_0/T and the $\sqrt{H}$ dependence of $\kappa_0(H)/T$ observed by thermal conductivity measurements.

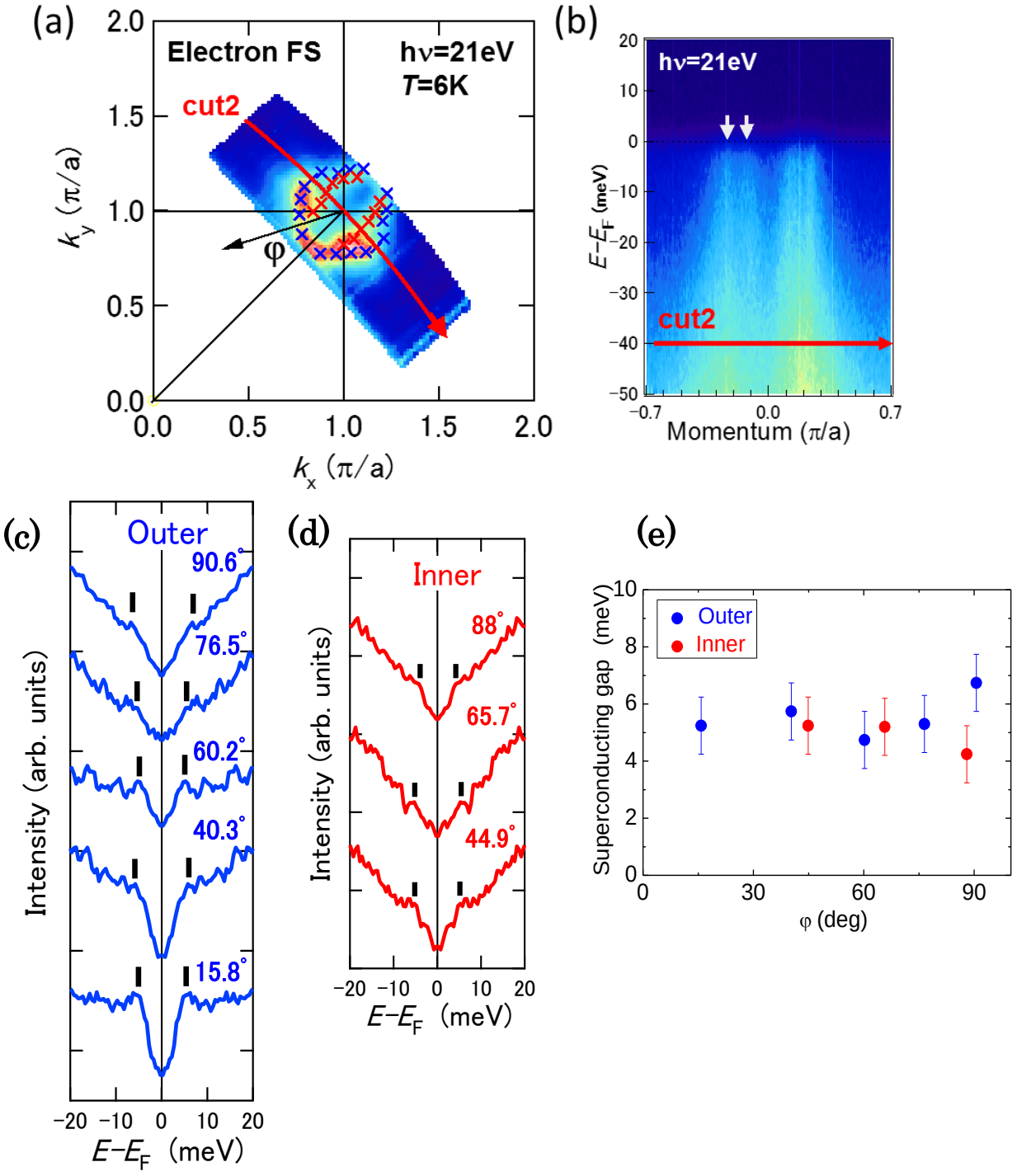

Figure 7.6 Electron FSs, band dispersions and SC gap on electron FSs of $Ba(Fe_{0.65}Ru_{0.35})_2As_2$. (a) Electron FS mapping around zone corner taken at 21eV. Definition of FS angle φ on electron FSs is indicated. (b) Energy-momentum plot corresponding to cut2 in (a). (c)-(d) Symmetrized EDCs at k_F of outer FS and inner FS, respectively, measured below T_c (~ 6 K) for various FS angles. Vertical bars indicate the SC gap energy. (e) SC gaps in (c)-(d) plotted as a function of FS angle.

Chapter 8

Summary and outlook

It is generally believed that a comprehensive understanding of the evolution of electronic states in the phase diagram will be crucial for elucidating the origin of the high temperature superconductivity of iron-based superconductors. In particular understanding the metallic AFM ground state which exists in the parent compounds is of primary importance. Mounting evidences suggest that the AFM ground state is unique with a hallmark of the electronic anisotropy. The major effort of this thesis is to characterize and understand the anisotropic electronic states of FeSCs through transport and ARPES measurements. Since the measurement of intrinsic electronic anisotropy is hampered by the twin formation below the transition temperature, we detwinned single crystals by applying uniaxial pressure.

First, a clear resistivity anisotropy in 11 compounds was revealed when the temperature was decreased below T_s. Surprisingly, in $Fe_{1+x}Te$, Cu-substituted, and Se-substituted compounds, ρ_a was always larger than ρ_b, opposite to the anisotropy observed in the 122 iron pnictides. On the other hand, it was found that the resistivity anisotropy was mostly determined by the anisotropy in the RR component. The magnitude of resistivity anisotropy in $Fe_{1+x}Te$ increased with the amount of excess Fe while the AFM order was suppressed. Although the results also show a correlation between the magnitude of the resistivity anisotropy and the amount of substituted Cu and Se atoms determined by EDAX analysis, the accuracy of EDAX analysis in determining chemical constitutions and the large effect of excess Fe on resistivity anisotropy prevent us from making a conclusive statement. However, our results potentially suggest the Cu and/or Se substitution also results in resistivity anisotropy.

Taking into account the results for the 122 iron pnictides [14], the impurity-induced anisotropy scenario may be a *generic* mechanism for the observed resistivity anisotropy in the iron-based materials. This, in other words, suggests an important common point through FeSCs. It is theoretically proposed that, for Co-doped $BaFe_2As_2$, the resistivity anisotropy can result from an impurity-induced local orbital order with broken C_4 symmetry in the presence of strong orbital fluctuations near T_s [65]. The further

clarification of the microscopic mechanism of the formation of the anomalous impurity state would help understand the interplay between the impurity and the degrees of freedom of the electronic states, which might be connected to the paring interaction in the superconducting state.

Second, annealed Ba-122 single crystals provide a system in which the crystal defects are effectively suppressed and the atom substitution can be accurately controlled. It has been revealed by previous studies of $Ba(Fe_{1-x}Co_x)_2As_2$ that exotic anisotropic impurity states are formed around the doped Co atoms. Our measurements on isovalent-substituted $Ba(Fe_{1-x}Ru_x)_2As_2$ confirmed the appearance of the resistivity anisotropy with Ru substitution. Both the magnitude of the resistivity and the resistivity anisotropy induced by isovalent Ru substitution is much smaller than that by heterovalent Co substitution. The linear correlation between RR and the resistivity anisotropy with different kinds of impurities (Co/Ru) suggests that the anomalous impurity states around Co and Ru ions have the *same* ratio between the cross sections along the *a*- and *b*-axes while having *distinct* scales in the spatial expansion. ARPES measurements showed that FSs in the AFM phase consisted of three types of pockets: isotropic hole pockets, Dirac-cone-like tiny electron pockets and another electron pocket which arises from the band folding and consequent band reconstruction. Although the direct correlation between the magnitude of resistivity anisotropy and the observed d_{xz}/d_{yz} band splitting is disapproved, our findings suggest that the observed resistivity anisotropy in the 122 compounds is likely to be related to the anisotropically scattering of the electron pockets.

In the future, the clarification of the origin of formation of the anomalous impurity state still remains an open issue. Theoretical studies suggested the importance of the orbital degrees of freedom in the AFM ground state. It would be helpful to clarify the orbital character of the reconstructed band dispersions near E_F both in 122 and 11, which exhibit opposite resistivity anisotropies. Since the neutral Fe/chalcogen block supports relatively high stability of the cleaved face for STS/STM measurements compared to that of 122, it is interesting to perform STM studies of the electronic state around impurity atoms (e.g., Cu) in iron chalcogenides.

Besides, ARPES studies of the superconducting gap structure in $Ba(Fe_{1-x}Ru_x)_2As_2$ (x = 0.35) showed a strong k_z dependence on the hole FSs, namely, the gap minimum appears around the Z point, implying the possible existence of “horizontal” line nodes near Z, where one of the hole FSs has a dominant contributions from d_{z^2} orbital. This is

qualitatively consistent with the predications based on the spin-fluctuation-mediated mechanism. However, the interplay between the spin and orbital fluctuations and the role of the structural modification/pnictogen height in tuning the SC gap structure of iron-based superconductors need to be further clarified.

Acknowledgements

I would like to express my sincere gratitude to all the people for their help and support during my doctoral study.

First, I would like to thank my supervisors, Prof. Atsushi Fujimori and Prof. Shin-ichi Uchida for their patience and kindness. Prof. Atsushi Fujimori has provided me with the opportunity to perform ARPES studies. It is his continuous encouragements and enlightening comments that help facilitating the completion of this thesis. Prof. Shin-ichi Uchida guided me in the first two years of my doctoral study until his retirement and continue to give me a lot of insightful advice after that. His valuable comments on the experimental results have benefited me a lot.

I would also like to thank Dr. Kozo Okazaki and Prof. Teppei Yoshida, who have taught me with great patience, from the principles to the experimental setups of photoemission experiments as well as the analysis methods. I would also like to express my gratitude to Dr. Teruhisa Kakeshita, who taught me many from the single crystal growth to the method of transport measurement, and also supported me in the daily life.

I would like to acknowledge Prof. Kanta Ono and Prof. Hiroshi Kumigashira for their experimental support at Photon Factory 28A, and Dr. Dong-hui Lu, Dr. Makoto Hashimoto and Prof. Zhi-Xun Shen for their collaborations and experimental support during the SSRL beamtime. I thank Prof. Shik Shin for a precious collaboration and the members of Shin group for a lot of assistances, especially Mr. Yuuichi Ota for his help for the laser-ARPES measurement. I would also like to thank the people at AIST: Dr. Kunihiro Kihou, Dr. Chul-Ho Lee, Dr. Akira Iyo, Dr. Hiroshi Eisaki for supplying me the single crystals and also for their valuable discussions. I also appreciate the assistances of Mr. Yoshinobu Nakamura, Dr. Daigorou Hirai, Prof. Hidenori Takagi on the EDAX analysis and PPMS/MPMS measurements.

I would like to express my gratitude to all the current and former members of Fujimori group: Dr. Toshiharu Kadono and Dr. Kohei Yoshimatsu for many interesting talks, Dr. Shin-ichiro Ideta for teaching me how to operate the ARPES measurement, Dr. Keisuke Ishigami, Mr. Goro Shibata, Mr. Yukio Takahashi, Mr. Shoya Sakamoto in the XMCD group for their detailed explanations for questions on magnetism and interesting talks in the lab, Mr. Leo Cristobal Ambolode II, Mr. Hakuto Suzuki, Ms. Jian Xu, Mr. Masafumi Horio in the ARPES group for their teaching me the fundamental principle of

photoemission spectroscopy, how to operate ARPES experiments, how to analyze data, a lot of valuable discussions and support during the beamtime.

I would also like to thank the former members of Uchida group: Dr. Kazuhiro Fujita for his teaching me how to grow cuprate single crystals, Mr. Tian Liang for his explanations on the iron-based superconductors, Dr. Shigeyuki Ishida and Dr. Masamichi Nakajima for their providing single crystals of iron pnictides, answering my various questions on experimental measurements and the physical problems. Mr. Ryo Suzuki, who struggled with serious diseases during his master study, has encouraged me a lot. Mr. Masayoshi Takahashi and Mr. Takahide Tanaka were ever my tutors when I just came to Japan, helping me get used to the life in Japan and teaching me almost all the basic experimental skills in Uchida group. Mr. Takuya Mikami, who spent the last year of Uchida group together with me, has helped me a lot both with the research work and in the daily life.

I would also like to thank Ms. Yuko Shimazaki, Ms. Ami Ito and Ms. Haruko Yoshimura for dealing with a lot of business stuff and giving me warm encouragements.

Finally, I would like to thank my family. My parents have all been supportive of my study. My wife shared my excitement and supported me with care.

References

[1] Y. Kamihara, T. Watanabe, M. Hirano, and H. Hosono, J. Am. Chem. Soc. **130**, 3296 (2008).

[2] J. Paglione, and R. L. Greene, Nat. Phys. **6**, 645 (2010).

[3] J. M. Tranquada, Physica B: Condensed Matter **407**, 1771 (2012).

[4] E. C. Blomberg, M. A. Tanatar, A. Kreyssig, N. Ni, A. Thaler, R. Hu, S. L. Bud'ko, P. C. Canfield, A. I. Goldman, and R. Prozorov, Phys. Rev. B **83**, 134505 (2011).

[5] J.-H. Chu, J. G. Analytis, K. De Greve, P. L. Mcmahon, Z. Islam, Y. Yamamoto, and I. R. Fisher, Science **329**, 824 (2010).

[6] S. Ishida, M. Nakajima, T. Liang, K. Kihou, C. H. Lee, A. Iyo, H. Eisaki, T. Kakeshita, Y. Tomioka, T. Ito, and S. Uchida, Phys. Rev. Lett. **110**, 207001 (2013).

[7] S. Ishida, M. Nakajima, T. Liang, K. Kihou, C.-H. Lee, A. Iyo, H. Eisaki, T. Kakeshita, Y. Tomioka, T. Ito, and S.-I. Uchida, J. Am. Chem. Soc. **135**, 3158 (2013).

[8] H.-H. Kuo, J.-H. Chu, S. C. Riggs, L. Yu, P. L. Mcmahon, K. De Greve, Y. Yamamoto, J. G. Analytis, and I. R. Fisher, Phys. Rev. B **84**, 054540 (2011).

[9] J. J. Ying, X. F. Wang, T. Wu, Z. J. Xiang, R. H. Liu, Y. J. Yan, A. F. Wang, M. Zhang, G. J. Ye, P. Cheng, J. P. Hu, and X. H. Chen, Phys. Rev. Lett. **107**, 067001 (2011).

[10] M. Nakajima, S. Ishida, Y. Tomioka, K. Kihou, C. H. Lee, A. Iyo, T. Ito, T. Kakeshita, H. Eisaki, and S. Uchida, Phys. Rev. Lett. **109**, 217003 (2013).

[11] M. Nakajima, T. Liang, S. Ishida, Y. Tomioka, K. Kihou, C. H. Lee, A. Iyo, H. Eisaki, T. Kakeshita, T. Ito, and S. Uchida, Proc. Natl. Acad. Sci. U.S.A. **108**, 12238 (2011).

[12] Y. Kim, H. Oh, C. Kim, D. Song, W. Jung, B. Kim, H. J. Choi, C. Kim, B. Lee, S. Khim, H. Kim, K. Kim, J. Hong, and Y. Kwon, Phys. Rev. B **83**, 064509 (2011).

[13] M. Yi, D. Lu, J.-H. Chu, J. G. Analytis, A. P. Sorini, A. F. Kemper, B. Moritz, S.-K. Mo, R. G. Moore, M. Hashimoto, W.-S. Lee, Z. Hussain, T. P. Devereaux, I. R. Fisher, and Z.-X. Shen, Proc. Natl. Acad. Sci. U.S.A. **108**, 6878 (2011).

[14] I. R. Fisher, L. Degiorgi, and Z. X. Shen, Rep. Prog. Phys. **74**, 124506 (2011).

[15] C. C. Chen, J. Maciejko, A. P. Sorini, B. Moritz, R. R. P. Singh, and T. P. Devereaux, Phys. Rev. B **82**, 100504 (2010).

[16] M. P. Allan, T. M. Chuang, F. Massee, Y. Xie, N. Ni, S. L. Bud'ko, G. S. Boebinger, Q. Wang, D. S. Dessau, P. C. Canfield, M. S. Golden, and J. C. Davis, Nat. Phys. **9**, 220 (2013).

[17] G. R. Stewart, Rev. Mod. Phys. **83**, 1589 (2011).
[18] E. Dagotto, Rev. Mod. Phys. **85**, 849 (2013).
[19] M. Nakajima, Docter thesis, University of Tokyo (2012).
[20] Y. Mizuguchi, and Y. Takano, J. Phys. Soc. Jpn. **79**, 102001 (2010).
[21] B. Wei, L. Guan-Nan, H. Qing-Zhen, C. Gen-Fu, H. Jun-Bao, W. Du-Ming, M. A. Green, Q. Yi-Ming, L. Jian-Lin, and W. Mei-Mei, Chinese. Phys. Lett. **30**, 027402 (2013).
[22] S. Nandi, M. G. Kim, A. Kreyssig, R. M. Fernandes, D. K. Pratt, A. Thaler, N. Ni, S. L. Bud'ko, P. C. Canfield, J. Schmalian, R. J. Mcqueeney, and A. I. Goldman, Phys. Rev. Lett. **104**, 057006 (2010).
[23] F. Rullier-Albenque, D. Colson, A. Forget, P. Thuéry, and S. Poissonnet, Phys. Rev. B **81**, 224503 (2010).
[24] S. Kasahara, T. Shibauchi, K. Hashimoto, K. Ikada, S. Tonegawa, R. Okazaki, H. Shishido, H. Ikeda, H. Takeya, K. Hirata, T. Terashima, and Y. Matsuda, Phys. Rev. B **81**, 184519 (2010).
[25] S. Ishida, Docter thesis, University of Tokyo (2012).
[26] H. Chen, Y. Ren, Y. Qiu, B. Wei, R. H. Liu, G. Wu, T. Wu, Y. L. Xie, X. F. Wang, Q. Huang, and X. H. Chen, EPL (Europhysics Letters) **85**, 17006 (2009).
[27] P. Richard, K. Nakayama, T. Sato, M. Neupane, Y. M. Xu, J. H. Bowen, G. F. Chen, J. L. Luo, N. L. Wang, X. Dai, Z. Fang, H. Ding, and T. Takahashi, Phys. Rev. Lett. **104**, 137001 (2010).
[28] J. Wen, G. Xu, G. Gu, J. M. Tranquada, and R. J. Birgeneau, Rep. Prog. Phys. **74**, 124503 (2011).
[29] S. Li, C. De La Cruz, Q. Huang, Y. Chen, J. W. Lynn, J. Hu, Y.-L. Huang, F.-C. Hsu, K.-W. Yeh, M.-K. Wu, and P. Dai, Phys. Rev. B **79**, 054503 (2009).
[30] A. M. Turner, F. Wang, and A. Vishwanath, Phys. Rev. B **80**, 224504 (2009).
[31] D. J. Singh, Phys. Rev. B **78**, 094511 (2008).
[32] D. C. Johnston, Adv. Phys. **59**, 803 (2010).
[33] T. Yoshida, I. Nishi, S. Ideta, A. Fujimori, M. Kubota, K. Ono, S. Kasahara, T. Shibauchi, T. Terashima, Y. Matsuda, H. Ikeda, and R. Arita, Phys. Rev. Lett. **106**, 117001 (2011).
[34] H. Okamoto, "Fe-Se (Iron-Selenium)", Binary Alloy Phase Diagrams, II Ed., Ed. T.B. Massalski 2, 1769 (1990).
[35] H. Okamoto, and L. E. Tanner, "Fe-Te (Iron-Tellurium)", Binary Alloy Phase Diagrams, II Ed., Ed. T.B. Massalski 2, 1781 (1990).
[36] M. Nakajima, S.-I. Uchida, K. Kihou, C.-H. Lee, A. Iyo, and H. Eisaki, J. Phys. Soc.

Jpn. **81**, 104710 (2012).

[37] S. Ishida, T. Liang, M. Nakajima, K. Kihou, C. H. Lee, A. Iyo, H. Eisaki, T. Kakeshita, T. Kida, M. Hagiwara, Y. Tomioka, T. Ito, and S. Uchida, Phys. Rev. B **84**, 184514 (2011).

[38] H. C. Montgomery, J. Appl. Phys. **42**, 2971 (1971).

[39] M. Takahashi, Master thesis, University of Tokyo (2012).

[40] T. Liang, M. Nakajima, K. Kihou, Y. Tomioka, T. Ito, C. H. Lee, H. Kito, A. Iyo, H. Eisaki, T. Kakeshita, and S. Uchida, J. Phys. Chem. Solids **72**, 418 (2011).

[41] S.-I. Ideta, Docter thesis, University of Tokyo (2012).

[42] M. Hashimoto, Docter thesis, University of Tokyo (2008).

[43] H. Suzuki, Master thesis, University of Tokyo (2013).

[44] C. R. Brundle, Journal of Vacuum Science and Technology **11**, 212 (1974).

[45] K. Okazaki, Y. Ota, Y. Kotani, W. Malaeb, Y. Ishida, T. Shimojima, T. Kiss, S. Watanabe, C. T. Chen, K. Kihou, C. H. Lee, A. Iyo, H. Eisaki, T. Saito, H. Fukazawa, Y. Kohori, K. Hashimoto, T. Shibauchi, Y. Matsuda, H. Ikeda, H. Miyahara, R. Arita, A. Chainani, and S. Shin, Science **337**, 1314 (2012).

[46] F.-C. Hsu, J.-Y. Luo, K.-W. Yeh, T.-K. Chen, T.-W. Huang, P. M. Wu, Y.-C. Lee, Y.-L. Huang, Y.-Y. Chu, D.-C. Yan, and M.-K. Wu, Proc. Natl. Acad. Sci. U.S.A. **105**, 14262 (2008).

[47] T. J. Liu, X. Ke, B. Qian, J. Hu, D. Fobes, E. K. Vehstedt, H. Pham, J. H. Yang, M. H. Fang, L. Spinu, P. Schiffer, Y. Liu, and Z. Q. Mao, Phys. Rev. B **80**, 174509 (2009).

[48] K. Momma, and F. Izumi, J. Appl. Crystallogr. **44**, 1272 (2011).

[49] E. E. Rodriguez, C. Stock, P. Zajdel, K. L. Krycka, C. F. Majkrzak, P. Zavalij, and M. A. Green, Phys. Rev. B **84**, 064403 (2011).

[50] Y. Mizuguchi, K. Hamada, K. Goto, H. Takatsu, H. Kadowaki, and O. Miura, Solid State Commun. **152**, 1047 (2012).

[51] Y. Zhang, F. Chen, C. He, L. X. Yang, B. P. Xie, Y. L. Xie, X. H. Chen, M. Fang, M. Arita, K. Shimada, H. Namatame, M. Taniguchi, J. P. Hu, and D. L. Feng, Phys. Rev. B **82**, 165113 (2010).

[52] G. F. Chen, Z. G. Chen, J. Dong, W. Z. Hu, G. Li, X. D. Zhang, P. Zheng, J. L. Luo, and N. L. Wang, Phys. Rev. B **79**, 140509 (2009).

[53] Z. K. Liu, R. H. He, D. H. Lu, M. Yi, Y. L. Chen, M. Hashimoto, R. G. Moore, S. K. Mo, E. A. Nowadnick, J. Hu, T. J. Liu, Z. Q. Mao, T. P. Devereaux, Z. Hussain, and Z. X. Shen, Phys. Rev. Lett. **110**, 037003 (2013).

[54] M. Yi, D. H. Lu, J. G. Analytis, J. H. Chu, S. K. Mo, R. H. He, M. Hashimoto, R. G. Moore, I. I. Mazin, D. J. Singh, Z. Hussain, I. R. Fisher, and Z. X. Shen, Phys. Rev.

B **80**, 174510 (2009).

[55] M. H. Fang, H. M. Pham, B. Qian, T. J. Liu, E. K. Vehstedt, Y. Liu, L. Spinu, and Z. Q. Mao, Phys. Rev. B **78**, 224503 (2008).

[56] M. Bendele, P. Babkevich, S. Katrych, S. N. Gvasaliya, E. Pomjakushina, K. Conder, B. Roessli, A. T. Boothroyd, R. Khasanov, and H. Keller, Phys. Rev. B **82**, 212504 (2010).

[57] Y. Sun, T. Taen, Y. Tsuchiya, Q. Ding, S. Pyon, Z. Shi, and T. Tamegai, Applied Physics Express **6**, 043101 (2013).

[58] T. Noji, T. Suzuki, H. Abe, T. Adachi, M. Kato, and Y. Koike, J. Phys. Soc. Jpn. **79**, 084711 (2010).

[59] Y. Han, W. Y. Li, L. X. Cao, X. Y. Wang, B. Xu, B. R. Zhao, Y. Q. Guo, and J. L. Yang, Phys. Rev. Lett. **104**, 017003 (2010).

[60] T. Sudayama, D. Ootsuki, Y. Wakisaka, T. Mizokawa, N. L. Saini, M. Arita, H. Namatame, M. Taniguchi, T. Noji, and Y. Koike, J. Phys. Soc. Jpn. **82**, 053705 (2013).

[61] J. Wen, Z. Xu, G. Xu, M. D. Lumsden, P. N. Valdivia, E. Bourret-Courchesne, G. Gu, D.-H. Lee, J. M. Tranquada, and R. J. Birgeneau, Phys. Rev. B **86**, 024401 (2012).

[62] R. M. Fernandes, L. H. Vanbebber, S. Bhattacharya, P. Chandra, V. Keppens, D. Mandrus, M. A. Mcguire, B. C. Sales, A. S. Sefat, and J. Schmalian, Phys. Rev. Lett. **105**, 157003 (2010).

[63] J. Jiang, C. He, Y. Zhang, M. Xu, Q. Q. Ge, Z. R. Ye, F. Chen, B. P. Xie, and D. L. Feng, eprint arXiv:1210.0397 (2012).

[64] T. Machida, K. Kogure, T. Kato, H. Nakamura, H. Takeya, T. Mochiku, S. Ooi, Y. Mizuguchi, Y. Takano, K. Hirata, and H. Sakata, Phys. Rev. B **87**, 214508 (2013).

[65] Y. Inoue, Y. Yamakawa, and H. Kontani, Phys. Rev. B **85**, 224506 (2012).

[66] N. Xu, T. Qian, P. Richard, Y. B. Shi, X. P. Wang, P. Zhang, Y. B. Huang, Y. M. Xu, H. Miao, G. Xu, G. F. Xuan, W. H. Jiao, Z. A. Xu, G. H. Cao, and H. Ding, Phys. Rev. B **86**, 064505 (2012).

[67] T. Mikami, Master thesis, University of Tokyo (2013).

[68] T. Terashima, N. Kurita, M. Tomita, K. Kihou, C.-H. Lee, Y. Tomioka, T. Ito, A. Iyo, H. Eisaki, T. Liang, M. Nakajima, S. Ishida, S.-I. Uchida, H. Harima, and S. Uji, Phys. Rev. Lett. **107**, 176402 (2011).

[69] E. C. Blomberg, M. A. Tanatar, R. M. Fernandes, I. I. Mazin, B. Shen, H.-H. Wen, M. D. Johannes, J. Schmalian, and R. Prozorov, Nat Commun **4**, 1914 (2013).

[70] K. Hashimoto, M. Yamashita, S. Kasahara, Y. Senshu, N. Nakata, S. Tonegawa, K. Ikada, A. Serafin, A. Carrington, T. Terashima, H. Ikeda, T. Shibauchi, and Y. Matsuda, Phys. Rev. B **81**, 220501 (2010).

[71] Y. Zhang, Z. R. Ye, Q. Q. Ge, F. Chen, J. Jiang, M. Xu, B. P. Xie, and D. L. Feng, Nat. Phys. **8**, 371 (2012).

[72] K. Suzuki, U. Hidetomo, and K. Kazuhiko, J. Phys. Soc. Jpn. **80**, 013710 (2011).

[73] X. Qiu, S. Y. Zhou, H. Zhang, B. Y. Pan, X. C. Hong, Y. F. Dai, M. J. Eom, J. S. Kim, Z. R. Ye, Y. Zhang, D. L. Feng, and S. Y. Li, Physical Review X **2**, 011010 (2012).

[74] M. J. Eom, S. W. Na, C. Hoch, R. K. Kremer, and J. S. Kim, Phys. Rev. B **85**, 024536 (2012).

[75] T. Shimojima, F. Sakaguchi, K. Ishizaka, Y. Ishida, T. Kiss, M. Okawa, T. Togashi, C. T. Chen, S. Watanabe, M. Arita, K. Shimada, H. Namatame, M. Taniguchi, K. Ohgushi, S. Kasahara, T. Terashima, T. Shibauchi, Y. Matsuda, A. Chainani, and S. Shin, Science **332**, 564 (2011).

[76] L. Wang, T. Berlijn, Y. Wang, C.-H. Lin, P. J. Hirschfeld, and W. Ku, Phys. Rev. Lett. **110**, 037001 (2013).

[77] Y. Ota, K. Okazaki, Y. Kotani, T. Shimojima, W. Malaeb, S. Watanabe, C. -T. Chen, K. Kihou, C. H. Lee, A. Iyo, H. Eisaki, T. Saito, H. Fukazawa, Y. Kohori, S. Shin, eprint arXiv:1307.7922v2 (2013).

[78] N. Xu, P. Richard, X. P. Wang, X. Shi, A. Van Roekeghem, T. Qian, E. Ieki, K. Nakayama, T. Sato, E. Rienks, S. Thirupathaiah, J. Xing, H. H. Wen, M. Shi, T. Takahashi, and H. Ding, Phys. Rev. B **87**, 094513 (2013).